
Dynamical Phenomena in Complex Plasmas

Ralf Heidemann



München 2012

Dynamical Phenomena in Complex Plasmas

Ralf Heidemann

Dissertation
an der Fakultät für Physik
der Ludwig-Maximilians-Universität
München

vorgelegt von
Ralf Heidemann
aus München

München, den 22. November 2012

Erstgutachter: Prof. Dr. G. E. Morfill

Zweitgutachter: Prof. Dr. H. Zohm

Tag der mündlichen Prüfung: 16. Januar 2013

Contents

Zusammenfassung	7
Abstract	9
1 Introduction	11
1.1 Plasma	11
1.2 Linear screening	11
1.3 Complex plasma	12
1.3.1 Charging	14
1.3.2 Forces	16
1.4 Discharges	22
2 Setup	25
2.1 PKE-Nefedov	26
2.2 PK-3 Plus	26
2.3 Gas control system	27
2.4 Electric feeding	27
2.5 Particles	30
2.6 Laser illumination and camera system	32
2.7 PK-4	32
3 Analysis methods	35
3.1 Particle kinetics	35
3.1.1 Particle detection (segmenting)	35
3.1.2 Position determination	35
3.1.3 Particle tracking	37
3.2 Density determination	38
3.2.1 2D mapping method	39
3.2.2 Uniform density distribution	40
3.2.3 Pair correlation function	41
3.3 Determination of the laser profile	44
4 Dissipative dark soliton	47
4.1 Theory	47
4.2 Experiments and results	50
4.2.1 Dissipative dark solitons in a rf complex plasma	50

4.2.2	Dissipative dark solitons in a dc complex plasma	53
4.3	Conclusion	55
5	Heartbeat	57
5.1	Experiments and results	57
5.2	Interpretation of the observations: a dynamical model of the heartbeat oscillations	58
5.2.1	Main phases of the heartbeat oscillation cycle	58
5.2.2	Dynamical model of microparticle motion	60
5.2.3	Comparison with experiment	61
5.3	Outlook	63
6	Interface Instability	65
6.1	Theory	65
6.1.1	Instabilities	68
6.2	Experiments	70
6.3	Outlook	72
7	Publications	73
7.1	Physical Review Letters (PRL): Dissipative Dark Soliton in a Complex Plasma	73
7.2	Europhysics Letters (EPL):Dissipative dark solitons in a dc com- plex plasma	78
7.3	Physics of Plasmas (PoP): Comprehensive experimental study of heartbeat oscillations observed under microgravity conditions in the PK-3 Plus laboratory on board the International Space Station	86
7.4	New Journal of Physics (NJP): Auto-oscillations in complex plas- mas	97
7.5	Europhysics Letters (EPL): Shear flow instability at the interface among two streams of a highly dissipative complex plasma	117
8	Acknowledgments	125
	List of Figures	127
	Bibliography	129

Zusammenfassung

Gegenstand der kumulativen Dissertation ist die experimentelle Untersuchung dynamischer Eigenschaften dreidimensionaler komplexer Plasmen. Komplexe Plasmen sind Niedertemperaturplasmen die zusätzlich Mikropartikel enthalten. Die Mikropartikel besitzen eine hohe elektrische Ladung durch die Absorption der Plasma Ionen und Elektronen. In dieser Dissertation werden Flüsse, Oszillationen und Wellen in komplexen Plasmen sowohl auf dem hydrodynamischen Niveau als auch auf dem kinetischen Level, der Bewegung einzelner Partikel, analysiert.

Der erste Teil der Dissertation beschäftigt sich mit dissipativen dunklen Solitonen. Das sind solitäre Verdünnungswellen die sich in stark dissipativen komplexen Plasmen ausbreiten. Die Experimente wurden sowohl in Radiofrequenz- als auch in Gleichspannungs-Entladungen durchgeführt. Die gemessenen Laufzeiten der Wellen waren dabei wesentlich länger als die Dissipationszeiten des Mediums. Der theoretische Hintergrund wird präsentiert um die Eigenschaften der Welle im Detail zu beschreiben. Die Resultate der Studie wurden in *Physical Review Letters* (PRL) [1] und in *Europhysics Letters* (EPL) [2] publiziert.

Im zweiten Teil der Dissertation werden die Grundlagen der Heartbeat Instabilität komplexer Plasmen präsentiert. Beim Auftreten der Instabilität beginnt das gesamte Partikelsystem in radialer Richtung zu pulsieren. Eine Serie von Experimenten, die an Bord der Internationalen Raumstation durchgeführt wurde, wird analysiert und die Dynamik der Instabilität wird im Detail beschrieben. Das Auftreten der Instabilität wird in einem weiten Parameterbereich untersucht und die Korrelation zwischen der Partikelbewegung, der Intensität des Plasmaleuchtens und den elektrischen Signalen wird analysiert. Ein Modell zur Beschreibung der Dynamik des Heartbeat Oszillationszyklus wird präsentiert. Die Ergebnisse der Untersuchungen wurden in *Physics of Plasmas* (PoP) [3] und in *New Journal of Physics* (NJP) [4] publiziert.

Im dritten Teil der Dissertation wird eine Rayleigh-Taylor Instabilität, die sich an der Grenzschicht zwischen einem fließenden und einem stationären komplexen Plasma entwickelt, beschrieben. Die Dynamik der einzelnen Partikel und die Hydrodynamik der Flüsse wird untersucht. Die Beobachtung einer dergleichen Instabilität ermöglicht die Untersuchung der Mikrostruktur der Flüsse beim Übergang von laminarer Strömung in einen ungeordneten und turbulenten Zustand. Die Resultate wurden in *Europhysics Letters* (EPL) [5] veröffentlicht.

Contents

Abstract

Object of this cumulative dissertation is the experimental investigation of dynamical properties of three dimensional complex plasmas. Complex plasmas are low temperature plasmas containing microparticles. These microparticles are highly charged by collecting plasma ions and electrons. Flows, oscillations and waves in complex plasmas are analyzed on the hydrodynamic level as well as the kinetic level of the motion of individual particles.

In the first part of the dissertation dissipative dark solitons are discussed. These are rarefactive solitary waves propagating in a highly dissipative complex plasma. Experimental studies were conducted in radio frequency and DC discharges. The propagation time of the waves was measured to be much longer than the dissipation times. The theoretical background is presented to describe the wave properties in detail. The results of the investigations were published in Physical Review Letters (PRL) [1] and in Europhysics Letters (EPL) [2].

In the second part of the dissertation the fundamentals of the heartbeat instability of complex plasmas are presented. When the instability occurs the particle system starts to pulsate rhythmically in radial direction. A series of experiments performed onboard the International Space Station was analyzed and the dynamics of the instability is described in detail. The occurrence of the instability is studied in a wide range of parameters and the correlations between the particle motion, the plasma glow intensity and the electrical signals are analyzed. A dynamical model explaining the heartbeat oscillation cycle is presented. The results of the experimental investigations are published in Physics of Plasmas (PoP) [3] and in New Journal of Physics (NJP) [4].

In the third part of the dissertation a Rayleigh-Taylor instability, developing at the interface of two complex plasma flows, is examined. Single particle dynamics and hydrodynamics of the flows are described. The opportunity to observe such an instability allows the exploration of the micro-structure of the flow at the transition from a laminar to disordered and turbulent state. The results are published in Europhysics Letters (EPL) [5].

Contents

1 Introduction

1.1 Plasma

Plasmas are ionized gases that contain a significant amount of electrical charged particles, enough to change its electrical properties. They possess a high electric conductivity and a strong interaction with electric and magnetic fields. A gas gets ionized when enough heat or other kinds of energy is supplied to separate some or all electrons from their atoms. The atoms that lost their electrons become positively charged ions. If enough atoms are ionized the gas becomes a plasma.

The term plasma was first applied to an ionized gas by Irving Langmuir in his publication “Oscillations in Ionized Gases” in 1928 [6]. He studied different types of mercury-vapor discharges and named the not glowing part close to the walls of the container “sheath” and the main body “plasma”, referring to the term “blood plasma”. The term was chosen because of some similar properties described by the Greek word plasma ($\pi\lambda\alpha\sigma\mu\alpha$) which means “moldable substance”. Unfortunately the double meaning of the term plasma causes misconceptions up to today.

Physical plasmas can have a very different characteristics depending on the types of atoms, the ratio of ionized to neutral atoms and the particle energies. This leads to a wide spectrum of natural occurrences and a large number of different applications. Plasmas are found in the sun and other stars [7] and in the intergalactic medium [8] in very different densities. On earth they are produced in lightnings and exist in the ionosphere, a layer of partially ionized gas in the upper atmosphere which reflects radio waves.

Plasmas are also used in a variety of industrial application for example in fluorescent lamps [9] and in plasma processing of semiconductors [10]. More recently the new field of plasma medicine developed where plasmas are used for sterilization of medical products and even the sterilization of living tissue [11, 12]. In the future plasmas may play an important role for energy production from nuclear fusion [13].

1.2 Linear screening

To describe the important properties of a plasma it is useful to introduce the model of the ideal plasma similar to the ideal gas model. Within an ideal

1 Introduction

plasma the interaction of electrons and ions is described by global fields instead of pairwise collisions. This is the case if the coupling parameter is much smaller than one, $\Gamma = \frac{E_{pot}}{E_{kin}} \ll 1$. Here the potential energy between the constituents is much smaller than their kinetic energy. This condition simplifies important calculations and is the base of the linear response formalism that describes the linear screening.

If a test charge is introduced in a plasma its potential will be exponentially screened. The screening is due to the change of the surrounding electron and ion distribution in the plasma. E.g. a negative test charge will attract ions and repel electrons. So the Coulomb potential $\Phi_c(Q, r) = \frac{1}{4\pi\epsilon_0} \frac{Q}{r}$ of the test charge in vacuum is exponentially suppressed. The resulting potential

$$\Phi(Q, r) = \Phi_c e^{-\frac{r}{\lambda_D}}$$

is called Debye-Hückel or Yukawa potential. The important parameter

$$\lambda_D = \frac{\lambda_{De}\lambda_{Di}}{\sqrt{\lambda_{De}^2 + \lambda_{Di}^2}}, \quad \text{with} \quad \lambda_{De,i} = \sqrt{\frac{k_B T_{e,i}}{4\pi n_{e,i} e^2}}$$

is the screening length which is the distance where the potential is reduced by e^{-1} . λ_D depends on the temperature $T_{e,i}$ and the density $n_{e,i}$ of the electrons and ions. In typical discharges used in this work the temperature of the electrons is much higher than the temperature of the ions ($T_i \ll T_e$). This means that ion screening length is much smaller $\lambda_{Di} \ll \lambda_{De}$ and so the ion screening is determining the screening length $\lambda_D \approx \lambda_{Di}$. In an ideal plasma the screening length is small compared to the system dimensions ($\lambda_D \ll L$) and the number of particles in a sphere with radius λ_D is much bigger than unity.

A spontaneous separation of charges in a plasma is only possible on a length-scale comparable with λ_D because a separation on a bigger scale would create very strong electric fields that would pull the electrons and ions back together. So on a large scale an ideal plasma is quasi neutral that means that the number of ions n_i is approximately equal to the number of electrons n_e or $\frac{Z_i n_i}{n_e} \approx 1$, where Z_i is the average ion charge in the case of multiple ionization.

1.3 Complex plasma

Complex plasmas are plasmas that contain additionally to ions, electrons and neutral atoms also charged macroscopic particles. Because of their typical size in laboratory experiments of $0.5 \mu\text{m} - 20 \mu\text{m}$ these particles are often called microparticles. A photograph of a typical complex plasma experiment is shown in figure 1.1. The introduction of the microparticles in the plasma offers unique experimental possibilities. Due to their high charge of several thousand elementary charges the microparticles can form a strongly coupled system. That

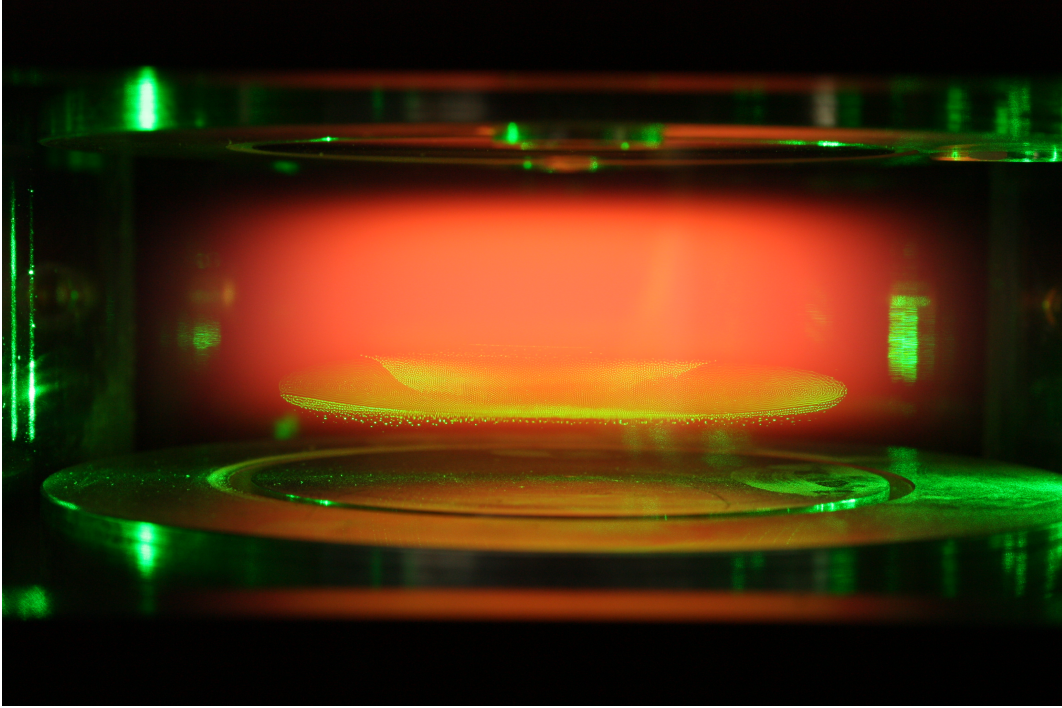


Figure 1.1: Photograph of a complex plasma in the PK-3 Plus chamber [14]. An orange glowing neon plasma is ignited between two rf-electrodes. The electrodes have a diameter of 6 cm and are surrounded by 1.5 cm wide grounded rings. A dense cloud of particles with a size of $3.42 \mu\text{m}$ is levitated in the bulk plasma and is illuminated by a green laser diode ($\lambda = 532 \text{ nm}$). Each of these microparticles attains a large electric charge of over $-4000 e$.

means that the Coulomb interaction energy between the particles can be much bigger than the kinetic energy of the particles. The coupling parameter Γ is much bigger than unity:

$$\Gamma = \frac{q_p^2}{\Delta 4\pi\epsilon_0 k_B T_p} \gg 1.$$

Here q_p is the particle charge, Δ is the interparticle distance and T_p is the temperature of the particle system. Above a critical value of Γ the particle system gets highly ordered and crystallizes [15, 16, 17]. The critical value depends thereby on the mean interparticle distance Δ that can be naturally normalized to the screening length λ_D :

$$\kappa = \frac{\Delta}{\lambda_D}.$$

By changing the control parameters it is possible to trigger a phase transition in the particle system.

1 Introduction

The big advantage of complex plasmas is that it is easy to analyze the kinetic motion of every single particle simply with the use of laser illumination and a camera. This makes it possible to study fundamental physical principles of a strongly coupled system at an atomistic level. Examples for already studied phenomena are phase transitions [18, 19], wave propagation [20, 21] and hydrodynamic instabilities [22].

Complex plasmas occur also naturally, then they are called “dusty plasmas” for example in planetary rings [23] and in the process of star formation [24]. They also occur in industrial applications like etching plasmas for semiconductors [25, 26]. Controlling and understanding complex plasmas is therefore also important to understand these phenomena.

1.3.1 Charging

The charge of a microparticle in a plasma depends on the fluxes from or to the particle. Important contributions can be ion- and electron collection currents, photo emission, thermionic emission or field emission. For typical complex plasma experiments the emission fluxes can be neglected. Additionally the electron collision frequency ν_e is much higher than the ion collision frequency ν_i for an uncharged sphere because of the higher electron temperature ($T_i \ll T_e$):

$$\nu_{e,i} \propto \sqrt{\frac{8k_B T_{e,i}}{\pi m_{e,i}}},$$

where $m_{e,i}$ is the electron/ion mass. This leads to a negative surface potential on the microparticle due to the bigger electron flux.

The magnitude of the charge can be estimated using orbit-motion-limited probe theory by Langmuir and Mott-Smith [27].

Orbital motion limited (OML) theory The assumption for the model is that the microparticle has no interaction with the plasma particles (ions and electrons) outside of a sphere with the radius of the screening length λ_D , the so called Debye-sphere. Inside the Debye-sphere electrons and ions are collisionless. This implies that the mean free path of ions and electrons is bigger than λ_D . In the model the plasma particles are deflected by the Coulomb potential of the microparticle, screening is not considered. The limit for the collection of a plasma particle is a particle trajectory that is tangential on the microparticle surface. By using the momentum and energy conservation it is possible to calculate the cross-section for the absorption of the plasma particle [28]:

$$\sigma_{e,i} = \pi r_p^2 \left(1 - \frac{2q_{e,i}\Phi_p}{m_{e,i}v_{e,i}} \right)$$

here r_p and Φ_p are the radius and the surface potential of the microparticle and $m_{e,i}$, $v_{e,i}$ and $q_{e,i}$ are the mass, speed and charge of the electron or ion. The fluxes on the particle surface can be calculated by integrating over the velocity distribution:

$$I_i = \pi r_p^2 n_i e v_{T_i} \left(1 - \frac{e\Phi_p}{k_B T_i} \right)$$

$$I_e = -\pi r_p^2 n_e e v_{T_e} \exp\left(\frac{e\Phi_p}{k_B T_e}\right),$$

where $v_T = \sqrt{\frac{8k_B T}{m\pi}}$ is the mean of the magnitude of the velocity. In steady state the ion and electron currents equilibrate ($I_i = I_e$). The resulting equation of the type $A - Bq_n = \exp(Cq_p)$ needs to be solved numerical. From this transcendental equation it is possible to calculate the particle charge. The obtained charge is approximately proportional to the particle radius and the electron temperature,

$$q_p \propto r_p T_e. \quad (1.1)$$

Collisionality parameter The applicability of the OML theory for complex plasmas is limited to low neutral gas pressures since ion neutral collisions are neglected in the model. [29] At higher gas pressures the ions in the vicinity of the microparticle can collide with neutral atoms. Charge exchange collisions and momentum loss increases the ion flux to the microparticle and decreases the absolute value of the particle charge. As demonstrated in [30] collisionality can be considered by introducing the collisionality parameter ξ :

$$I_i = \pi r_p^2 n_i e v_{T_i} \left(1 - \xi \frac{e\phi_p}{k_B T_i} \right).$$

$\xi = 1$ is the collisionless case and corresponds to the OML limit. However the factor ξ introduced in [30] is only valid for very high collisionality:

$$\xi = \sqrt{\frac{2\pi}{3}} \frac{\lambda_n}{r_p}, \quad \lambda_n < \frac{1}{3} \lambda_D,$$

where λ_n is the mean free path for ion neutral collisions. The applicability has been extended by fitting the correction parameter to simulation data in [31], known as the drift motion limited (DML) approximation:

$$\xi = \sqrt{\frac{2}{3}} \pi \frac{\lambda_n}{r_p + r^*}, \quad r^* = \sqrt{\frac{2}{3}} \pi \frac{\lambda_n^2}{3\lambda_D + \lambda_n}, \quad \lambda_n > 0.1\lambda_D.$$

The particle charge calculated with DML are up to 50% lower than the one calculated with OML [31, 32].

1 Introduction

Havnes parameter Another important influence on the microparticle charge is the microparticle density n_d in a complex plasma. The captured electrons on a particle reduce the electron flux to a second particle. This reduces the absolute magnitude of the particle charge. The captured electrons have also to be taken into account for the neutrality condition:

$$n_i = n_e + Zn_d,$$

where $Z = \frac{q_p}{e}$ is the particle charge number. The relationship is often rewritten to:

$$H = \frac{Zn_p}{n_i},$$

where H is introduced as the Havnes parameter [33].

1.3.2 Forces

The particles in a complex plasma are negatively charged and their field is screened by the plasma electrons and ions as it was described above. In turn the particles interacting with the plasma have a feedback on the plasma itself. To simplify the description the particles of a complex plasma are sometimes treated as a homogeneous and isotropic one component Yukawa liquid. The model is also used in the description of very high density matter and numerical simulations [15, 34].

Isotropy can be destroyed for example by gravity or by streaming ions. Streaming ions can lead to a wake potential behind the particles. The wake potential is a positive space charge that introduces an attractive component in the interparticle interaction. This can lead for example to chain formation [35].

Global electric force The particle system is embedded in the plasma potential which changes on a much bigger scale than the particle separation. The background plasma potential acts as a global confinement for the particles. As described in Sec. 1.4 the bulk plasma is field free and the main potential drop is situated in the plasma sheath. In the case of low plasma density ($10^6 - 10^8 \text{ cm}^{-3}$) the sheath width can be up to 1 cm and can occupy a significant part of the plasma vessel. In this case electrical fields can penetrate far into the system. The global electric potential has then a quadratic shape in first approximation. An example can be seen in Fig. 1.2. Here the electric potential calculated with a MD Simulation (Siglo-2D [36]) of neon plasma in the PK-3 Plus chamber (the setup will be described in a later chapter) is shown.

Neutral gas drag The neutral gas drag dissipates the kinetic energy of single particles. This paves the way for the creation of strongly coupled states where the potential energy of the particles is bigger than the kinetic energy and the

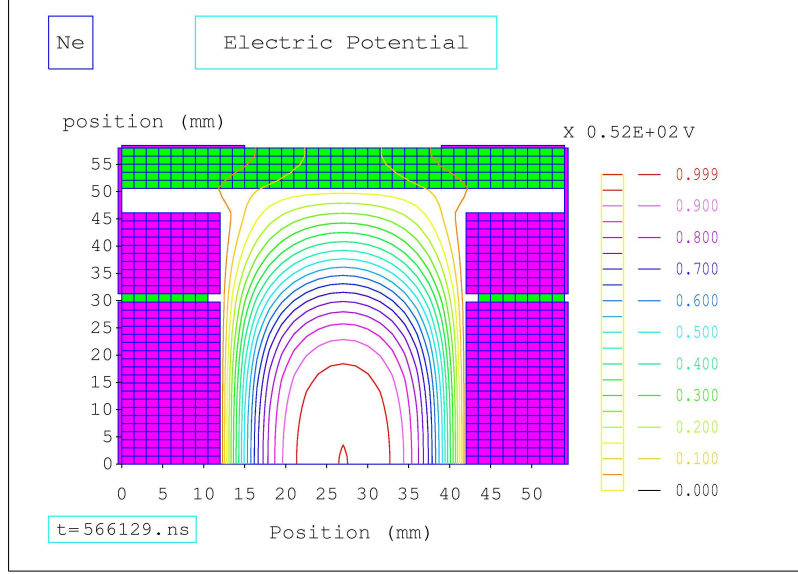


Figure 1.2: Electric potential in the plasma chamber calculated with a MD simulation (Siglo-2D [36]). This potential acts as a global confinement for the particle system. In first approximation the potential has a quadratic shape along the main axes.

particle system is able to crystallize. The neutral gas drag is also the main reason for the damping in collective particle phenomena like wave propagation and can suppress some types of instabilities like the Kelvin-Helmholtz instability. In the Epstein limit [37] of small relative velocity v_p compared to the thermal velocity of the gas atoms ($\frac{v_p}{v_a} \ll 1$) and particles with a diameter d_p much smaller than the atom mean free path ($\frac{d_p}{\lambda_a} \ll 1$) the force can be approximated by:

$$F_N = \gamma m_p v_p; \quad \gamma = \delta \frac{4}{3} \pi \frac{n_a m_a}{m_p} \sqrt{\frac{8k_B T_a}{\pi m_a}} r_p^2, \quad (1.2)$$

where m_p and r_p is mass and radius of the microparticle and m_a , n_a and T_a are the mass, the number density and the temperature of the gas atoms. The value of the coefficient $\delta = (1 + \eta \frac{\pi}{8})$ depends on the model of the interaction of the gas atoms with the particle surface. $\eta = 0$ stands for specular reflection, $\eta = 1$ for diffuse reflection [37]. Experimentally a value $\eta = 0.66$ of has been measured [38].

The drag coefficient γ is inverse proportional to the particle radius for particles with a constant mass density:

$$\gamma \propto \frac{r_p^2}{m_p} \propto \frac{1}{r_p}.$$

1 Introduction

Kinetic energy E_{kin} is dissipated in the system with $E_{kin} \propto e^{-\gamma t}$. Because of that the use of bigger particles is profitable for experiments with dynamical effects to avoid overdamping.

Equation 1.2 shows that the neutral gas drag force is proportional to the squared radius of the particle:

$$F_N \propto r_p^2$$

and proportional to the neutral gas pressure p :

$$F_N \propto n_a \propto p.$$

Thermophoresis Thermophoresis is an important tool for complex plasma experiments in a ground based laboratory since it can be used to counteract gravity. The source of the thermophoretic force is a temperature gradient in the gas surrounding a microparticle. The gradient leads to a slightly higher average kinetic energy of the gas atoms on the warmer side of the particle. So the average momentum transfer from collisions of the atoms with the particle is higher from the warmer than from the colder side. That results in a net force on the particle that points in the direction of the temperature gradient. So if the lower electrode of the plasma chamber is heated and the upper electrode is kept cool then the resulting thermophoretic force can compensate the gravitational force acting on the particle. The magnitude of the force can be calculated using the following empirically obtained formula [39]:

$$F_T = -3.33 \frac{k_B r_p^2}{\sigma} \frac{dT}{ds}, \quad (1.3)$$

here r_p is the radius of a spherical particle, σ is the cross-section for atom – atom collisions and $\frac{dT}{ds}$ is the temperature gradient. The thermophoretic force is proportional to the surface of the particle:

$$F_T \propto r_p^2.$$

Gravity can be properly compensated in the PK-3 Plus setup for particles with a radius smaller than $3 \mu\text{m}$ where a temperature gradient of less than 500 K/m has to be set between the electrodes. The use of bigger particles is eligible for many experiments since the neutral gas drag is smaller and the whole system less dissipative. The high temperature gradients that are needed for these particles are difficult to establish homogeneous enough e.g. there is always an additional gradient to the cold windows of the plasma chamber that are needed for observation. Additionally the temperature gradient can drive gas fluxes in the chamber either by normal convection or by gas creep along the chamber walls that also occurs at lower gas pressures [40]. For this reasons experiments with heavier particles are performed in microgravity on board the international space station or in parabolic flights.

Ion drag force Electric fields in a discharge cause ion currents. These ion fluxes create a force, the ion drag force, due to the momentum transfer between the ions and the microparticle.

The ion drag force has a deep impact on the structure and shape of the particle system. In particular the ion drag force might result in the appearance of the void, a particle free region in the center of an rf discharge (Sec. 1.3) and plays a central role in the heartbeat instability mechanism (Sec. 5). The exact theory of the ion drag force is still an open question with important advancements since 2002 [41, 42].

In the classical approach the momentum to a point like test-charge is transferred due to collisions between the ions and the particle [43]. With the assumption that the microparticle velocity v_p is negligible and that the ion mean free path is much larger than the screening length ($\lambda_i \gg \lambda_D$) for a collisionless plasma the resulting force is:

$$(F_I)^{classical} = n_i v_s m_i v_i 4\pi b_{\pi/2}^2 \Lambda, \quad (1.4)$$

here n_i is the ion density, m_i the ion mass, v_i the velocity of the ion current, v_s is the mean speed of the ions $v_s = \sqrt{v_T^2 + v_i^2}$, where $v_T = \sqrt{\frac{8k_B T}{m\pi}}$ is the mean of the magnitude of the velocity and Λ is the Coulomb logarithm.

The impact parameter with the asymptotic orbit angle $\pi/2$ is:

$$b_{\pi/2} = \frac{e^2 Z}{4\pi\epsilon_0 m_i v_s^2},$$

where Ze is the particle charge, normally negative in an RF complex plasma.

The Coulomb logarithm Λ can be obtained by integrating the transport scattering cross-section

$$d\sigma_t = 2\pi(1 - \cos\Theta)b db = 2\pi b(\Theta) \left| \frac{db}{d\Theta} \right| (1 - \cos\Theta) d\Theta,$$

where Θ is the scattering angle and $b(\Theta) = \frac{b_{\pi/2}}{\tan(\Theta/2)}$. It is convenient to rewrite $d\sigma_t$ as:

$$d\sigma_t = 4\pi \frac{b db}{1 + \left(\frac{b}{b_{\pi/2}}\right)^2}$$

To obtain the momentum transfer cross-section, this expression has to be integrated over a limited range from $b = 0$ to $b = b_{max}$. (At $b \rightarrow \infty$ the cross-section diverges.)

$$\sigma_t = \int_0^{b_{max}} d\sigma_t = 4\pi b_{\pi/2}^2 \ln \left[1 + \left(\frac{b_{max}}{b_{\pi/2}}\right)^2 \right]^{\frac{1}{2}}$$

1 Introduction

in the classical case the “cut-off” radius is suggested to be $b_{max} = \lambda_D$ assuming that there is no scattering at $b > \lambda_D$. The calculation is valid for $b_{\pi/2} < \lambda_D$.

$$\Lambda = \frac{1}{2} \ln \left[1 + \left(\frac{b_{max}}{b_{\lambda_D}} \right)^2 \right].$$

For a microparticle with finite radius absorption of the ions reaching the particle surface has to be taken into account [44]. With orbit-motion-limited (OML) theory the impact factor for the ion collection can be calculated as:

$$b_B = r_p \left(1 - \frac{2e(\Phi_p - \Phi_s)}{m_i v_s^2} \right)^{\frac{1}{2}},$$

here r_p is the particle radius, Φ_s is the plasma potential and Φ_p is the surface potential of the particle. Each impacting ion transfers its momentum ($m_i v_i$) to the particle. This results in the force:

$$F_B = n_i v_s m_i v_i \pi b_B^2.$$

The collection of ions changes the value of Λ in equation 1.4. It is now integrated over $[b_B, \lambda_D]$. This results in:

$$\Lambda = \frac{1}{2} \ln \left(\frac{\lambda_D^2 + b_{\pi/2}^2}{b_B^2 + b_{\pi/2}^2} \right).$$

The total ion drag force obtained by Barnes et al. [44] is the sum over both contributions:

$$(F_I)^{Barnes} = (F_I)^{classical} + F_B = n_i v_s m_i v_i \pi (b_B^2 + 4b_{\pi/2}^2 \Lambda) \quad (1.5)$$

The first component b_B^2 is proportional to particle radius and charge, $b_B^2 \propto r_p q_p$, while the second component $b_{\pi/2}^2$ is proportional to charge squared, $b_{\pi/2}^2 \propto q_p^2$. Assuming that the charge is proportional to the radius $q_p \propto r_p$ (cf. section 1.3.1) the ion drag force is proportional to radius squared:

$$(F_I)^{Barnes} \propto r_p^2. \quad (1.6)$$

The theory was further improved by Khrapak et al. [41] by considering scattering with the impact parameters $b > \lambda_D$ in a Yukawa potential. This changes the value of the Coulomb logarithm to:

$$\Lambda_K = 2 \int_0^{\infty} e^{-x} \ln \left(\frac{2\lambda_D x + b_{\pi/2}}{2r_p x + b_{\pi/2}} \right) dx.$$

Compared to Barnes formula, this correction results in a one magnitude stronger ion drag force:

$$(F_I)^{Khrapak} = \frac{2\sqrt{2\pi}}{3} n_i v_s m_i v_i b_{\pi/2}^2 \Lambda_K.$$

Even without the consideration of ion collection, the estimated force is strong enough to explain the existence of the void, the particle free region in the center of the discharge [45]. Further improvements of the theory will have to consider more than one microparticle, in particular the case when the ion mean free path is bigger than the interparticle separation ($\lambda_i \gg \Delta_p$) where the assumption of a single isolated microparticle is not valid anymore.

Gravity The gravitational force F_G plays an important role in experiments with bigger particles ($> 1 \mu\text{m}$). The gravitational force of the particle is:

$$F_G = m_p g = \rho_p r_p^3 g.$$

The force is proportional to the volume of the particle for a constant mass density ρ_p :

$$F_G \propto r_p^3.$$

The gravitational force pushes the particles in the sheath where the force is compensated by electrical forces.

$$F_G = F_E, \quad mg = ZeE.$$

The charge of the particle Ze is proportional to its radius according to the OML theory (see equation 1.1):

$$Ze \propto r_p.$$

The stronger dependence on r_p is the main reason why it is difficult to levitate heavier particles under gravity conditions also if particles with the very low density of melamine formaldehyde are used. If the electric field E for levitation is increased for example by increasing the discharge power also the outwards pointing ion drag force increases. As shown above the ion drag force is proportional to the particle surface (see equation 1.5):

$$(F_I)^{Barnes} \propto r_p^2.$$

This limits the levitation of bigger particles further.

The neutral gas drag coefficient is proportional to the surface of the particle:

$$F_N \propto r_p^2.$$

Also the thermophoretic force that is often used to compensate gravity is proportional to the particle surface:

$$F_T \propto r_p^2.$$

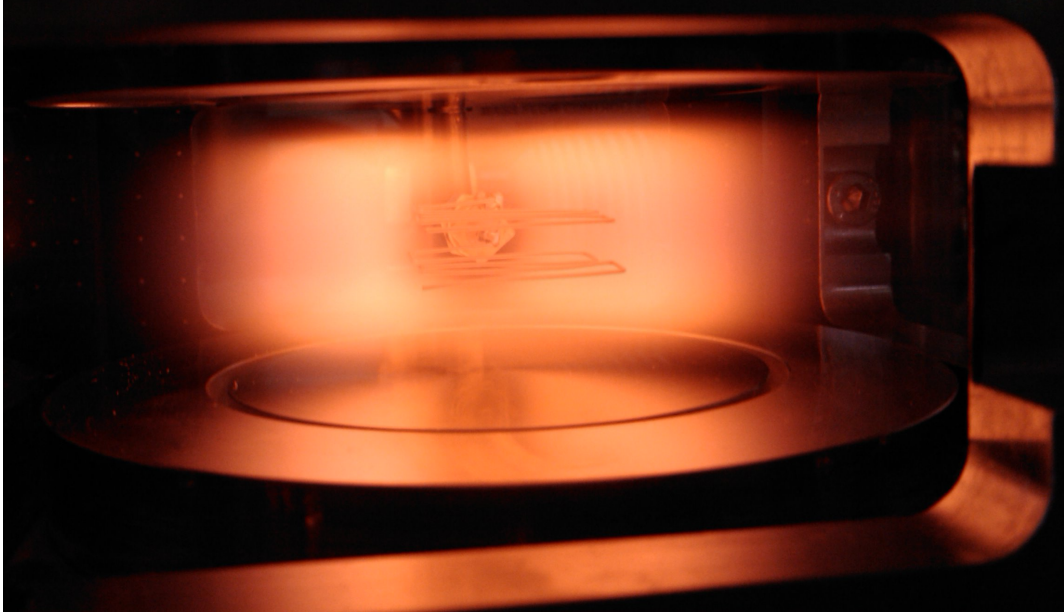


Figure 1.3: Photograph of a neon plasma in the PK-3 Plus plasma chamber with a frequency shift probe in the center. The circular metal plate is the lower electrode with the surrounding grounded ring.

In summary the gravitational force has the strongest dependence on the particle radius and dominates for large particles. This makes for some experiments microgravity conditions necessary.

1.4 Discharges

In the plasma reactors that are used in the experiments within this work a plasma is created by applying electric fields that accelerate electrons which then ionize atoms by collisions. For a DC discharge this can be achieved by applying a high DC voltage to two electrodes in a vacuum chamber filled with the working gas. Here primary electrons are accelerated and start an electron avalanche. The breakdown voltage that needs to be applied to start the discharge depends primarily on the gas pressure p , the distance between the electrodes d_e and the gas type. The breakdown voltage V_b can be calculated with Paschen's law:

$$V_b = \frac{A p d_e}{\ln(p d_e) + B}.$$

The coefficients A and B are empirically determined and depend on the gas type and the electrode material. This type of discharge is used in the PK-4 setup, that is described in section 2.7. For these experiments the operating

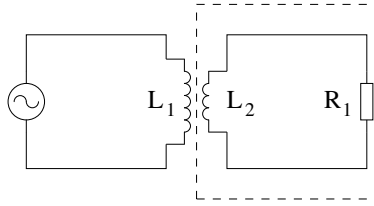


Figure 1.4: Simplified circuit of a inductively coupled discharge. The dashed box contains the equivalent circuit of the plasma. The RF-generator is connected to a coil (L_1). The plasma acts as the second coil (L_2) of a transformer.

voltage is usually around 1 kV. This is in the range of a normal glow discharge and well below the arc discharge regime that starts at much higher voltage.

Instead of a DC-voltage also alternating voltage can be used to drive the discharge. These discharges are often operated at radio frequency (rf) and then called rf-discharges. If the frequency of the voltage is high enough the massive ions cannot follow and the applied power is mainly absorbed by the free electrons. The oscillating electrons acquire enough energy to ionize other atoms by collisions.

The discharge can be driven inductively or capacitively. For an inductively coupled discharge the electrons are excited by an alternating magnetic field. The impedance of the plasma acts as a second coil of a generator. The high frequency coil [46] that drives the plasma that can be situated outside of the plasma vessel. The oscillating inductive electric field heats the electrons which then ionize the atoms. A simplified electrical circuit for a inductively coupled discharge is shown in Fig. 1.4. Electrically the plasma is equivalent to a coil with ohmic resistance in this case.

The plasma can also be capacitively coupled to electrodes with a varying electric field driving the plasma. A simplified circuit for a capacitively coupled discharge is shown in Fig. 1.5. In this circuit the RF-Generator is connected to the electrode via a blocking capacitor (C_1). This allows for the collection of charges on the electrode and so its possible to measure its self bias. The equivalent circuit of the plasma itself consists of the two capacitances for the plasma sheaths (C_1 and C_2) and the ohmic resistance (R_1) of the plasma.

In the configuration shown in figure 1.5 only one electrode is driven the other one is grounded resulting in an asymmetric discharge. The plasma chambers of PKE-Nefedov and PK-3 Plus that are described in section 2.2 have two parallel plate electrodes that are symmetrically driven in a push pull mode. That means that the same power is applied to both electrodes but there is a 180° phase shift between the voltage on the electrodes. This results in a symmetric discharge.

Independent on the ionization mechanism all plasmas share some common physical properties. One of them is the before mentioned plasma sheath. It

1 Introduction

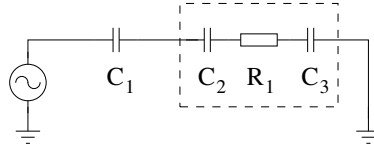


Figure 1.5: Simplified circuit of a capacitively coupled discharge. The dashed box contains the equivalent circuit of the plasma. C_2 and C_3 are the capacitances of the plasma sheath. The RF-generator is connected to the electrode by the blocking capacitor C_1 .

is the transition zone from the bulk plasma to the walls. The lighter electrons have a higher mobility than the ions and leave the plasma faster and get lost to the chamber walls. This electron loss leads to an electric potential that restrains the electrons from leaving the plasma and accelerates the ions towards the walls.

The width of the plasma sheath is of the order of the screening length and the sheath is not quasi neutral. The potential drop from bulk plasma to the walls happens mainly in the sheath. In low temperature RF plasmas with electron densities $n_e = 10^6 - 10^8 \text{ cm}^{-3}$ the sheath width is 1 – 10 mm.

2 Setup

The experiments presented in this thesis have been performed with four different complex plasma laboratories. For experiments with wave propagation large homogeneous complex plasmas are favorable. For this reason the soliton experiments, described in chapter 4 are performed in the PK-3 Plus laboratory on ground and the PK4 laboratory in parabolic flights. The experiments for interface instabilities shown in chapter 6 have been conducted in the PKE-Nefedov laboratory because its better suited for the excitation of vortex flows and stable interfaces between motionless and streaming complex plasmas. The heartbeat experiments described in chapter 5, have been performed under microgravity onboard the ISS in the PK-3 Plus laboratory, because it allows to use bigger particles and so the experiments can cover a much wider parameter space. Additionally probe measurements have been performed in the PK-3 Plus laboratory on ground to compliment the other experiments and to contribute to future experiments in this successful laboratory.

This makes in total four setups that are described in the following: PKE-Nefedov on ground, PK-3 Plus onboard the ISS, PK-3 Plus on ground and PK-4 in parabolic flights. The PK-4 differs strongly from the others and is described separately at the end of the chapter.

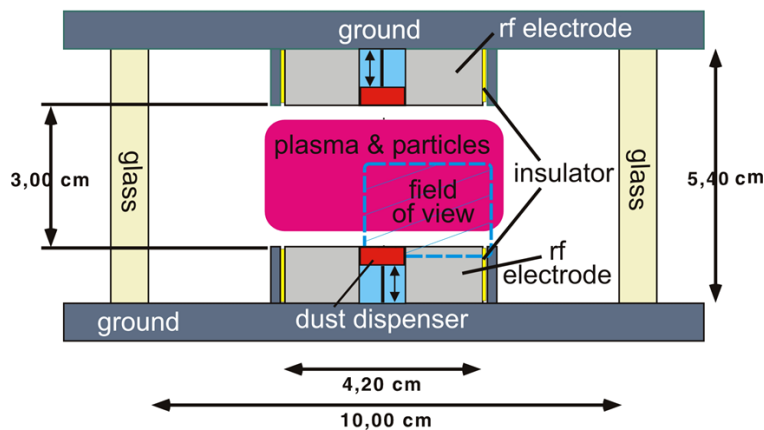


Figure 2.1: Schematic of the PKE-Nefedov plasma chamber.

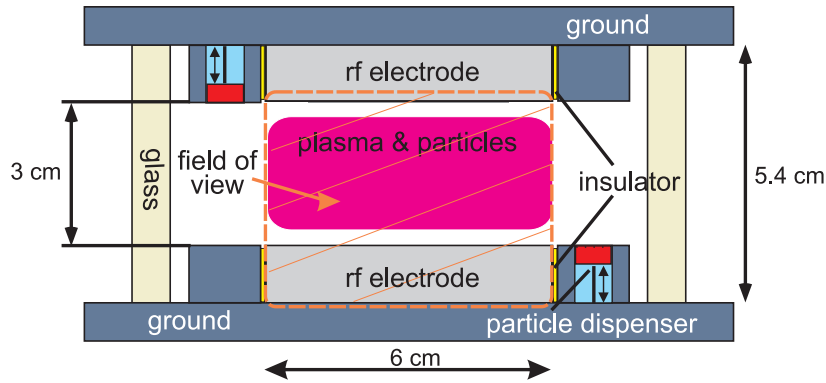


Figure 2.2: Schematic of the PK-3 Plus plasma chamber.

2.1 PKE-Nefedov

The PKE-Nefedov laboratory [47] has been designed at the Max-Planck Institute for extraterrestrial physics to be used in microgravity for longterm investigations of complex plasmas. The laboratory has been used on the International Space Station (ISS) from 2001 to 2005. Heart of the laboratory is a symmetrical driven rf-plasma chamber. The sidewalls of the vacuum chamber are made of a single quadratic glass cuvette. Top and bottom of the chamber are metallic flanges (see Fig. 2.1). Included in the flanges are the rf-electrodes which are mounted in a parallel plate configuration and are driven in a push-pull mode.

Particle dispensers are mounted in the center of the electrodes to inject particles into the plasma. The electrodes are surrounded by a grounded guard ring. The experiments presented in chapter 6 have been performed in a modified version of the PKE-Nefedov plasma chamber with a wider guard ring (10mm wide). Four Peltier devices are used to control the temperature gradient between the upper and lower electrode. They are used for the control of the thermophoretic force on the microparticles (see section 1.3.2). The vacuum system (described in section 2.3) and the electrical feeding (described in section 2.4) also differ from the one used on the space station and are the same that are used for the experiments with the PK-3 Plus plasma chamber.

2.2 PK-3 Plus

The PK-3 Plus laboratory [48] is an enhanced version of the PKE-Nefedov laboratory and its successor on the ISS. It has been developed to obtain more homogeneous complex plasmas especially useful for crystallization experiments. Additionally it provides improved hardware, software and diagnostics which makes it more versatile. The main differences are the wider electrodes and the wider grounded guard ring. Additionally a new type of particle dispensers

has been introduced and they are no longer mounted in the electrodes but in the guard rings. Another new feature of the PK-3 Plus laboratory is the low frequency function generator that is connected to the electrodes. It allows to apply voltages up to ± 55 V with different waveforms overlayed on the rf-signal. It was used for the wave excitation in the experiments described in chapter 4. Several resistors below the ground plate are used for the temperature control in the ground setup. They are connected to a furnace temperature control system and are used for experiments with thermophoresis.

2.3 Gas control system

The gas control system consists for all experiments of two main parts, the gas supply and the vent line with the vacuum pumps. The vent line consists of a membrane pump that creates a pre vacuum for the turbo molecular pump. On the space station the membrane pump is replaced by a connection to the vacuum of space. The turbo molecular pump is connected to the plasma chamber via a pressure controller that allows to set the base pressure for the experiments. In the experimental setup on the space station the gas is supplied via a dead volume of a three way valve. By rotating the valve a small gas portion enters an expansion volume and finally enters the plasma chamber through a capillary. For the ground based experiments the gas is supplied by an automatic mass flow controller. The pressure in the plasma chamber is measured by capacitance manometers.

2.4 Electric feeding

An RF-generator that operates at 13.56 MHz with 4 W maximal output is connected to the electrodes via a matching network. The matching network is used to minimize the reflected power. The impedance-matching is done once at nominal operating conditions. A servo-loop corrects small mismatches that occur if the operating conditions are changed, for example, a different rf-power or gas pressure. Forward and reflected power are measured within the generator and are part of the housekeeping data that are analyzed in the following chapters. A new matching is necessary if the plasma chamber is changed like for the experiments in chapter 6 where the PK-3 Plus chamber is replaced by the PKE-Nefedov chamber.

In both chambers top and bottom electrodes are symmetrically driven e.g. they receive the same power. They are operated in push-pull mode so their phases are shifted by 180° . The connecting circuit of the PK-3 Plus chamber is shown in Fig. 2.6.

An important component of the circuit is the bridge compensating for the

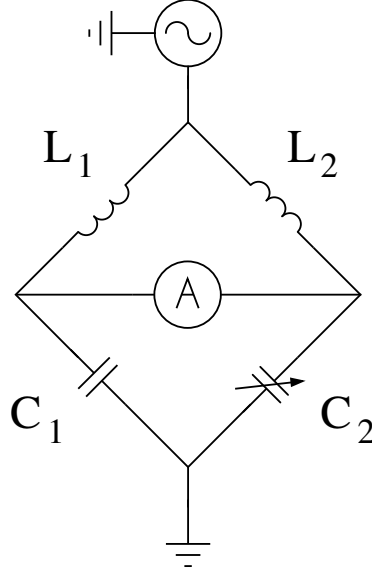


Figure 2.3: RF-current measurement in a bridge configuration. C_1 is the capacitance of the electrode towards the structure. The discharge is capacitively coupled and parallel to C_1 . C_2 is a tunable capacitor. L_1 and L_2 are coils. The current towards the electrode flows through L_1 . The voltage measured in A is reduced by an auxiliary current through branch L_2C_2 . This compensates the voltage generated in L_1 by the losses from the current flowing through C_1 . The bridge is nulled by adjustment of C_2 in the plasma-off condition. In the plasma-on condition meter A reads a voltage $U_p = \omega L_1 I_p$, where ω is the angular frequency and I_p is the current fraction due to plasma dissipation only. The measured current is part of the housekeeping data and is used to classify the discharge.

capacitance of the transmission lines and electrodes (see Fig. 2.3). These additional capacitances cause leak currents. With the help of the bridge-circuit these leak currents are subtracted at the current measurement. The measured root mean square values of current and voltage are favorable for characterizing the discharge. Since the discharge has an almost linear response at low power it is also common to use the forward RF-power for the discharge characterization. The forward RF-power gives only the matched output power of the generator but is not corrected for the leak currents.

To determine the fraction of the input power that reaches the plasma also the nonlinear response of the system has to be taken into account. Nonlinear effects further decrease the power factor η , which is introduced by:

$$P_{rms} = \eta \cdot I_{rms} U_{rms}$$

$$P(t) = I(t)U(t)$$

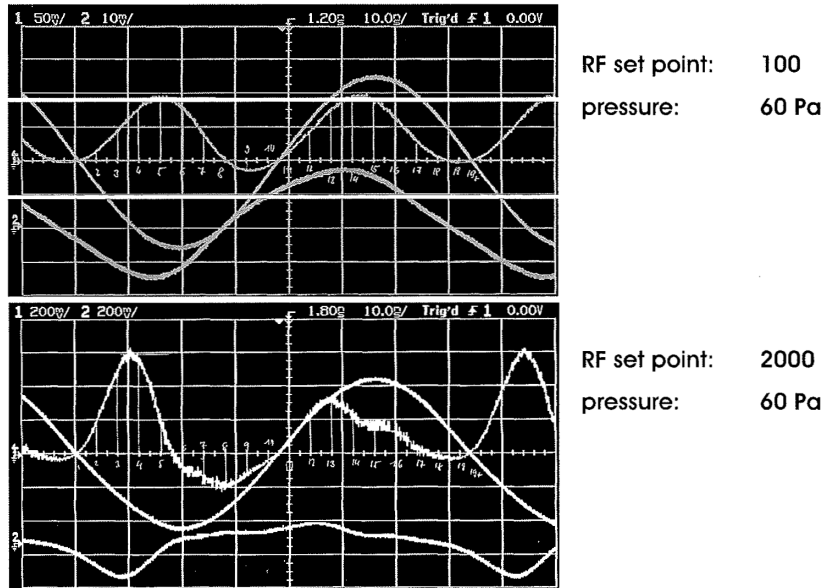


Figure 2.4: Time resolved measurement of current and voltage on the electrode and calculated power (marked with numbers and vertical lines). The power is sinusoidal at low input powers (upper panel, RF set point 100) which gives a high power factor. For high input power (lower panel) the plasma has a strong nonlinear response that results in a low power factor. The picture is taken from the technical documentation of PK-3 Plus. (Note: RF set point 4095 is equivalent to 4W output power.)

Here P is the power, I is the current, and U is the voltage. The linear reactive components of the circuitry (reactive impedance) lead to a phase shift between current and voltage that also reduces the power factor. In the PK-3 Plus setup phase shift is compensated by the matching network. However the nonlinear effects that can change the waveform of the current cannot be compensated. These distortions reduce the power transferred to the system, hence lower the power factor.

Fig. 2.4 shows the measured $U(t)$, $I(t)$ and $P(t)$ for two RF-power set points. At higher power the current deviates strongly from a sinusoidal form resulting in a lower η value (lower panel in Fig. 2.4). Most experiments have been performed at an RF set point below 500 where the estimated η is between 0.8 and 0.4 (Fig. 2.5).

The electric measurements are an important tool to analyze complex plasma experiments and to classify the discharge. The most important are the forward rf-power, the rms-current and rms-voltage. Analysis of these measurements included in all parts of this work in chapters 4 – 6, they are especially important for the heartbeat experiments (chapter 5) where the housekeeping data can be

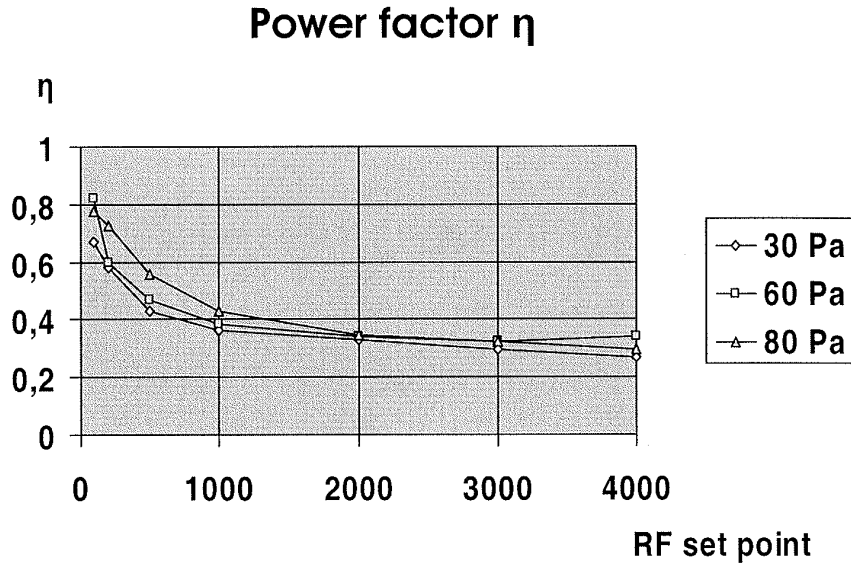


Figure 2.5: Power factor η for the PK-3 Plus setup for three gas pressures. $\eta = I_{rms}U_{rms}P_{rms}^{-1}$. Most experiments are performed at an RF set point below 500 where η is between 0.8 and 0.4. The picture is taken from the technical documentation of PK-3 Plus.

correlated to particle oscillations.

2.5 Particles

The microparticles that are injected in the plasma for the experiments are melamine-formaldehyde (MF) particles that are commercially available. The particles are monodisperse and have a mass density of 1510 kg/m^3 . The used particles have a diameter between $1 \mu\text{m}$ and $16 \mu\text{m}$.

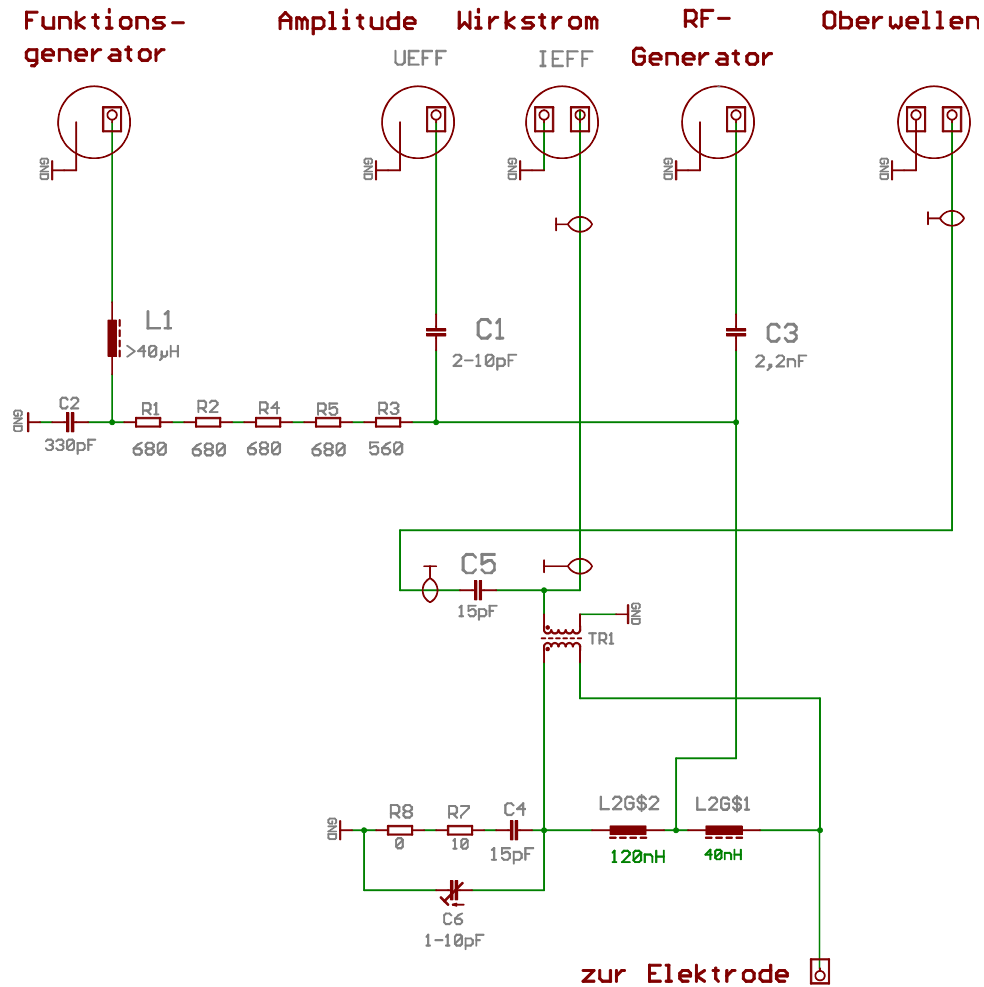


Figure 2.6: Circuit diagram of the external electric wiring for one electrode. Identical circuits are installed on both electrodes. One of the two symmetrical generator outputs is connected via capacitor C3 to a current sensor in bridge configuration (see Fig. 2.3). The measurement signal is conducted to a SMA-type connector labeled “Wirkstrom”. Also shown are measurement ports for rf-voltage (labelled “Amplitude”) and for harmonics in the current (labelled “Oberwellen”). Each of these are connected by a $50\ \Omega$ cable to a $50\ \Omega$ quadratic detector in the experiment electronics (not shown). The quadratic detectors provide the effective values: I_{eff} and U_{eff} used throughout the dissertation. The fifth port (“Funktionsgenerator”) is for the connection of a function generator that can add a DC-bias or low frequency modulations on the electrodes. The diagram is an altered version from the technical documentation of PK-3 Plus.

2 Setup

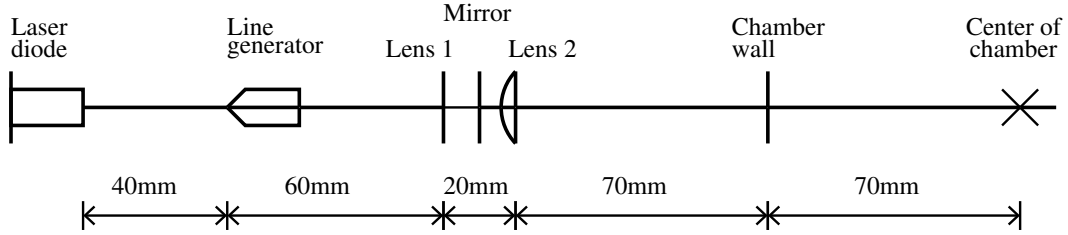


Figure 2.7: Scheme of the illumination laser optics for the ground setup of PK-3 Plus and PKE-Nefedov. The laser diode has a wavelength of 532 nm and 200 mW output power.

2.6 Laser illumination and camera system

The cloud of microparticles embedded in the plasma is optically thin so it is possible to illuminate the particles with a laser without occultation through shadowing. With the use of laser optics only a thin slice of the particle cloud is illuminated the scattered light from the particles is recorded with a camera at an angle of 90° . The recorded images are then analyzed to determine the particle kinetics (see section 3.1). An example of a recorded image from an experiment is shown in figure 2.8.

For this work a illumination system was constructed with a green laser diode with a wavelength of 532 nm and 200 mW output power for the ground setup of PK-3 Plus and PKE-Nefedov. A scheme of the laser optics is shown in Fig. 2.7. The diode has a beam diameter of $130 \mu\text{m}$ and a full angle divergence of 11 mrad.

On the space station a red laser diode with a wavelength of 686 nm and a power of 40 mW is used. The laser optics are more compact but function is a similar way. A measurement of the laser profile is presented in chapter 3.3.

The main reason for the higher laser power in the ground based experiments is that there a high speed camera is used with much shorter exposure time. The CMOS camera has a frame rate of 1000 Hz at a resolution of 1024×1024 pixels. For the ISS experiment CCD cameras with a frame rate of 50 Hz are used. Here three cameras are installed with different fields of view and a fourth camera for the observation of the plasma glow. On the cameras for the particle observations filters are used to remove the plasma radiation.

2.7 PK-4

The PK-4 setup differs substantially from the other setups, as mentioned above, since its used for DC-Discharges. The plasma chamber is a U-shaped glass tube with electrodes on both ends. The complex plasma experiments are performed in the positive column of the electric glow discharge. It is situated in the base tube which is 35 cm long and has a diameter of 3 cm. The microparticles in the

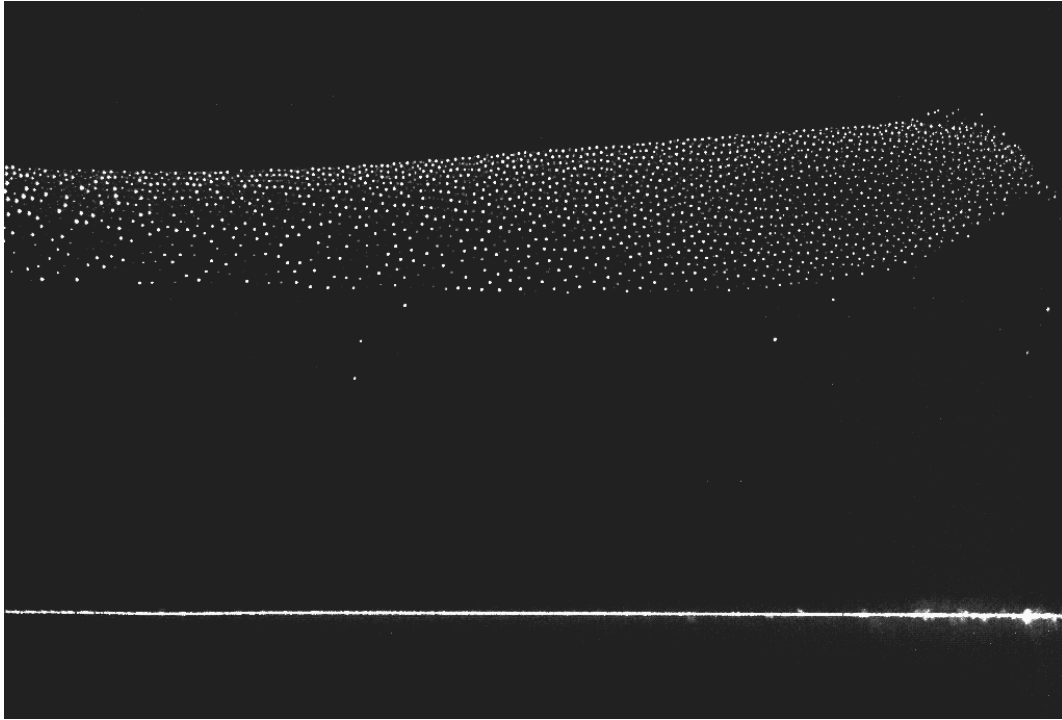


Figure 2.8: Example of a typical image recorded during an experiment in PK-3 Plus. A thin slice of the three dimensional particle cloud is illuminated by a laser diode and the scattered light from the particles is recorded with a camera at an angle of 90° . The white line below the particles stems from reflections on the lower electrode.

base tube can be illuminated with a laser through flat windows at the sides of the tube.

The gas control system of the PK-4 setup is similar to the one used in the ground setup of PK-3 Plus. Two pumps are connected to one end of the tube, a turbo molecular pump and a membrane pump for the pre-vacuum. The working gas inlet is on the other side of the tube. The gas stream in the tube can be used to manipulate the particles. The inlet is operated by a flow controller. Microparticles can be injected by gas jet dispensers in the arms of the tube. The generator regulates the discharge current to 1.0 mA the voltage depends on the gas pressure and is usually around 1000 V. The longitudinal electric field has been measured to be $\approx 2 \text{ V/cm}$ [49] independent of the gas pressure in the range between 15 Pa and 150 Pa. The electron density n_e and the electron temperature T_e were measured with Langmuir probe measurements [49, 50]. Typical conditions are $n_e = (1 - 2) \cdot 10^8 \text{ cm}^{-3}$ and $T_e = 5 - 7 \text{ eV}$.

The setup can be operated in pure DC-conditions as well as a low-frequency discharge regime. This is done by changing the polarity of one electrode while the other electrode is grounded. Typical operation frequency is 1 kHz. The

2 Setup

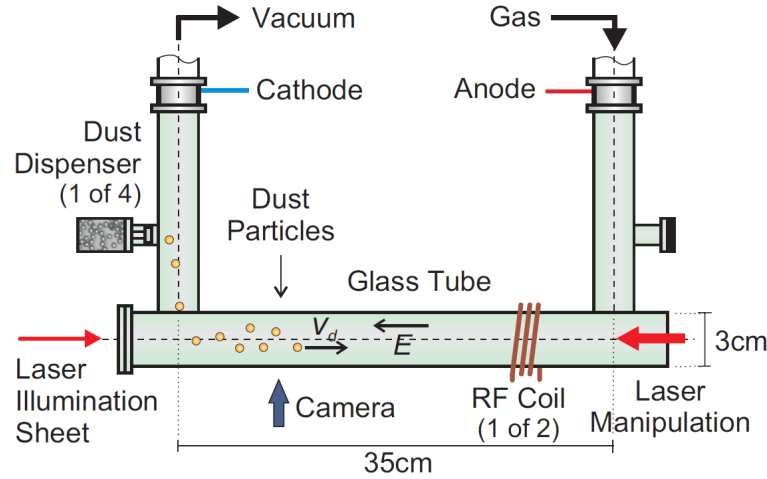


Figure 2.9: Scheme of the PK-4 setup.

duty cycle of the polarity switching can be adjusted which results in an average electric field in the discharge. The effective longitudinal force on the particles from the electric and the iondrag force can be used to manipulate the particle cloud. For a 50% duty cycle the net force is zero and the particles can be trapped in a steady state position. Additionally a coil mounted around the glass tube which can be powered by an RF-generator at 13.56 MHz and 81.36 MHz. This gives the possibility of mixed DC-RF-discharges. The coil can also be used for particle manipulation by applying DC voltage. This is used in the soliton experiments described in chapter 4.

The PK-4 setup is especially well suited for the investigation of particle flows and wave dynamics. The length of the tube allows for much longer propagation length compared to the other setups. The PK-4 setup is scheduled to succeed PK-3 Plus on the International space station. It is planned to continue the very successful complex plasma experiments under microgravity conditions.

3 Analysis methods

3.1 Particle kinetics

The determination of the microparticle position is a fundamental step in the analysis of complex plasma experiments. As described in section 2.6, the microparticles are illuminated by a laser and their scattered light is recorded by a CCD-camera. The brightness distributions provided by the camera consists of the signal from the particles, a background and noise. The process of the determination of the particle kinetics can be divided in several steps: particle detection (segmenting the image), determination of position of the center and the tracking of the particle from frame to frame. All processes are usually accomplished by applying programmed routines and algorithms. In principle there are two possible sequences for the algorithms: segmenting \rightarrow positioning \rightarrow tracking or: segmenting \rightarrow tracking \rightarrow positioning. Examples for both sequences are given below.

3.1.1 Particle detection (segmenting)

The difficulty of this task depends on the signal to background ratio, the ratio between the brightness of the particle and the brightness of the background and on the signal to noise ratio. If both ratios are larger than 50% a simple threshold method can be used to detect the particles. The method can be improved by removing the systematic background for example from plasma radiation. Such a background can be caused by measurements with no optical filters where the plasma glow is also recorded. The background can be determined by averaging over time or by applying smooth filters. The particle detection routine fixes the total amount of particles and outputs approximate positions for the position determination routine.

3.1.2 Position determination

A simple algorithm to determine the particle position is the **center of intensity method**. In this method first the pixels p_i are selected that belong to the particle and then the position vector \vec{r}_p of the center of the intensity is

3 Analysis methods

calculated:

$$\vec{r}_p = \frac{\sum_i \vec{r}_i s_i}{\sum_i s_i}, \quad s_i = I_i - b$$

where \vec{r}_i is the position vector of pixel p_i and I_i is its intensity. s_i is the signal of the particle with subtracted background b . A difficulty in this method is that the background has to be determined precisely. If its overestimated than a part of the signal is cut. This increases the error from noise.

If it is underestimated the calculated position of the particle is shifted compared to the true location because of **pixel locking** [51, 52]. The position is shifted in direction of \vec{r}_b : the center of intensity of the not subtracted background (b_n).

$$\vec{r}_b = \frac{\sum_i \vec{r}_i b_n}{\sum_i b_n}.$$

\vec{r}_b can have only values of:

$$|\vec{r}_b| \pmod{1} = 0$$

for an even amount of pixels and constant b_n or

$$|\vec{r}_b| \pmod{0.5} = 0$$

for an uneven amount of pixels. An example of the pixel locking effect can be seen in Fig. 3.1. If the true positions of the particles are evenly distributed within a pixel then pixel locking causes a concentration around \vec{r}_b . Another problem of the method is the selection of pixels that constitute the particle image. For example if a pixel is selected that belongs to a neighboring particle the calculated center of intensity is shifted because a pixel far away from the center of intensity has a big lever.

To avoid many problems of the center of mass method a new **model fit** method for the position determination has been developed for the analysis of the experiments of this work. In this method the intensity profile of a single particle in the image is assumed to be Gaussian with locally constant background.

$$h(\vec{r}) = A_0 \exp \left[\frac{1}{2} \left(\frac{|\vec{r} - \vec{A}_1|}{A_2} \right)^2 \right] + A_3$$

The fit provides the position of the particle \vec{A}_1 , the maximum intensity A_0 and the full width at half maximum $2\sqrt{2 \ln(2)} A_2$. Another advantage of the method is that the local background level is determined and can be cross checked with other background determination methods. This naturally avoids the pixel locking effect. Moreover bright pixels in the tail of the Gaussian do not shift the position as much as in the center of intensity method. The used fit routines provide also error estimates for the position. The main error source is the noise on the pixels close to the center of the Gaussian.

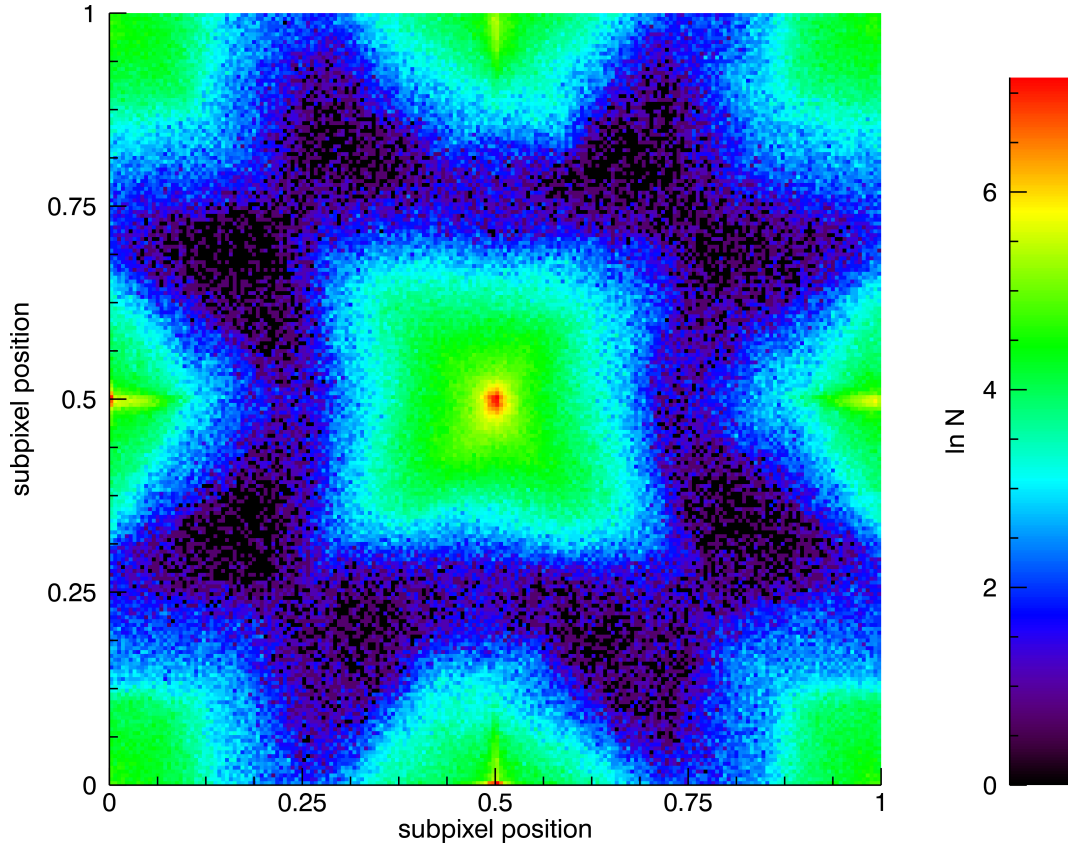


Figure 3.1: Particle positions with strong pixel locking. Shown is a 2D histogram of the particle positions r_p modulo 1 pixel of $1.4 \cdot 10^6$ particles. Color coded is the natural logarithm of the number of particles per bin. Without pixel locking the positions are equally distributed.

3.1.3 Particle tracking

After the position of every particle in all relevant frames is determined the particles have to be identified in consecutive frames. Only then it is possible to analyze the particle kinetics. The choice of the algorithm to track the particles depends on the specific experiment. For slow moving particles (for example particles in a crystalline state) the next position can be searched in the **proximity** of the previous position. This is possible if the particle velocity v_p per frame rate (fr) is smaller than half of the mean interparticle separation: $\frac{v_p}{\text{fr}} < \frac{1}{2}\Delta$. If the particle velocity is higher but predictable, for example in a laminar particle stream, then the next position can be searched in the proximity of the **extrapolated** position in the next frame. Still the algorithm can lead to lost particles or wrong identification.

For this reason a new algorithm has been developed that is based on the **connection of the lightpath** of the particle. In this method first the pixels

are identified that belong to a particle. This is done by an image filter that is adapted to the image conditions. Every pixel in the filtered “image” has the value zero or one. The pixels with the value one belong to a particle, pixels with the value zero do not belong to a particle. Then connected regions are labeled. Next connected or overlapping regions in the consecutive frame are identified and the labels are transferred. Finally the original regions are passed on to the position determination algorithm that used the model fit. From this information the tracks are constructed. The sequence for the light path algorithm is: segmenting \rightarrow tracking (by lightpath) \rightarrow positioning.

The lightpath algorithm only works if the dead time between the exposer times of consecutive frames is small enough. This is almost always the case for the cameras used in complex plasma experiments. The lightpath algorithm is specially suited for experiments where the particle velocity is so high that they produce strongly elongated images. That is if the particle moves more than the diameter of its image d_i while the exposer time $\frac{1}{f}$: $v_p > d_i f$. The proximity algorithm often fails in this case.

3.2 Density determination

An important parameter to describe a complex plasma is the particle density $n = \left(\frac{4\pi}{3}a_{ws}^3\right)^{-1}$, where a_{ws} is the Wigner-Seiz radius [53] and the mass density $\rho_m = mn$ of the particle system, here m is the mass of one particle: $m = V_p\rho_p$, where V_p is the particle volume and ρ_p density of the used material. So the mass density assuming spherical particles can be calculated to:

$$\rho_m = \rho_p \left(\frac{d_p}{a}\right)^3$$

where d_p is the particle diameter (usually between 1 and 10 μm) and $a = 2a_{ws}$ is the mean particle separation (usually between 100 and 1000 μm). Most experiments are performed with melamin formaldehyde particles which has a density of 1510 kg/m^3 . Typically ρ_m/ρ_p is between 10^{-6} and 10^{-3} .

The main problem is to determine the three dimensional (3D) particle density n . Since, as described in section 2.6, only a small slice of the entire particle cloud is illuminated by the laser and only a two dimensional (2D) projection recorded by the camera is available for analysis, this is a difficult task.

To demonstrate the different methods and to derive the proper geometric factors simulation data are used. Below an example of such a simulation is presented. In the simulation the particle cloud is in a liquid (disordered) state as it was in the most experiments discussed in sections 4, 5 and 6.

The MD simulation with periodic boundary conditions and Yukawa type interparticle interaction was performed for $N_{3D} = 36000$ particles in a cubic region. The simulation data set are the 3D positions of the particle cloud at

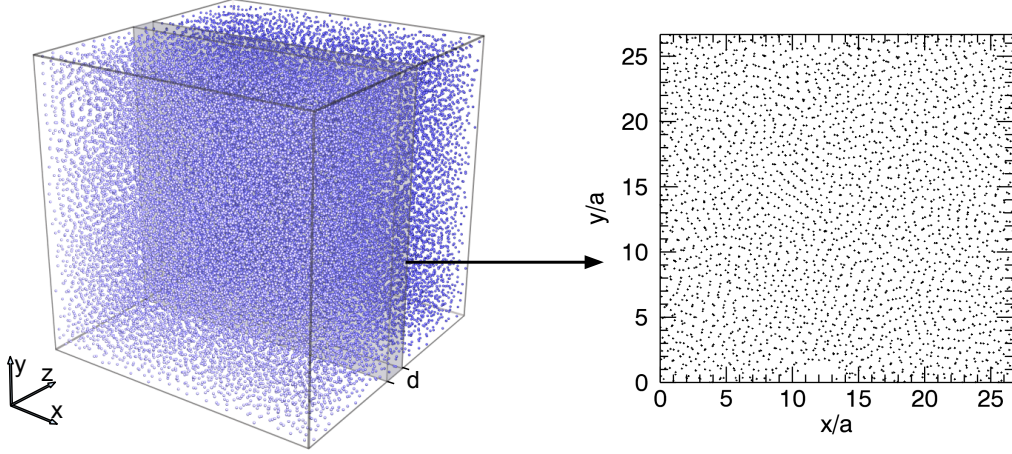


Figure 3.2: (left) 3D positions of the particles obtained from the MD-simulation [54] and (right) the projection of a slice onto the x-y plane. All distances are normalized to the interparticle separation a .

a fixed time moment (cf. Fig. 3.2). The simulations have been performed by Dr. Jiang. The simulation method has been published in [54].

Slices of different width d were taken at the center of the data set and projected in the normal direction of the slice to simulate certain aspects of the density calculation. This represents taking a picture of the slice of particles and then determine the (2D) position of the particles within the picture. That means only x and y coordinates of the particles in the slice were used for the 2D calculations. The width of the slice is equivalent to the thickness of the laser sheet in the experiment.

To obtain a reference value, the 3D density n_0 was calculated with $n_0 = \frac{N_{3D}}{V}$, where V is the volume of the particle cloud. The interparticle separation $a = 2a_{ws}$ was calculated by $a = \left(\frac{6}{\pi} \frac{V}{N_{3D}}\right)^{\frac{1}{3}}$.

The particle coordinates are normalized to a . This is a natural choice because only the ratio a/d between the interparticle separation and the laser sheet width is the most important parameter. To determine whether it is possible or not to restore a 3D distribution having at hand only 2D projections is the main goal of this chapter. There are a few known methods that will be discussed in the following.

3.2.1 2D mapping method

The simplest approach to calculate the 3D density is to assume that the interparticle separations a_{2D} in the 2D projection is the same as a_{3D} in 3D. a_{2D} can be calculated by $a_{2D} = \left(\frac{4}{\pi} \frac{S}{N_{2D}}\right)^{\frac{1}{2}}$, where S is the area of the studied projection and N_{2D} is the number of particles in S . The area per particle is the area of

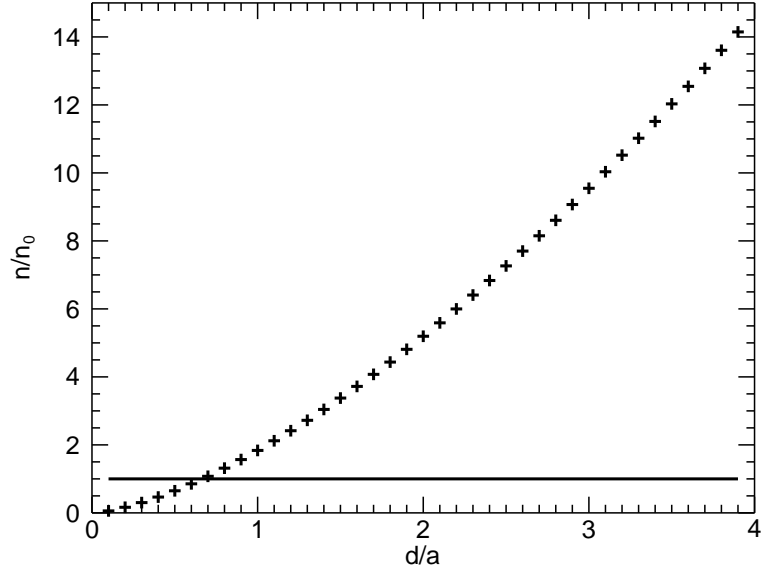


Figure 3.3: Particle density of the simulated particle cloud calculated from 2D projections with different slice width d (marked with crosses). d represents the thickness of the laser sheet and is normalized to the interparticle separation a . The estimated density is normalized to the actual density n_0 (black line corresponds to $n = n_0$).

a circle with radius $\frac{1}{2}a_{2D}$, the 2D Wigner-Seitz radius. The 3D density can be calculated as:

$$n = ka_{2D}^{-3}, \quad k = \frac{6}{\pi},$$

or directly from the 2D area density n_{2D} :

$$n = \xi n_{2D}^{\frac{3}{2}}, \quad \xi = \frac{3\sqrt{\pi}}{4}, \quad n_{2D} = \frac{N_{2D}}{S},$$

k and ξ are the geometric factors that depend on the actual structure of the particle cloud. A few examples are given in Sec. 3.2.3. The main disadvantage of this method is that the density is strongly overestimated if $d > a$ (that is if the laser is broader than the interparticle separation) and underestimated for $d < a$. This is illustrated in Fig. 3.3. Method 1 gives only the correct value if $d/a \approx 0.7$.

3.2.2 Uniform density distribution

The density estimate can be improved if d , the laser sheets thickness is known. Then one can assume that all particles that are visible in the 2D projection (N_{2D}) are located in the particle cloud with the volume $S \times d$ where S is the

area of the picture taken for analysis. The density can be calculated by:

$$n = \frac{N_{2D}}{Sd}$$

under the assumption that all “projected” particles are recognizable in the 2D image. Since d is known in the simulation and also no particles are lost due to overlapping, this method gives the true value within statistical variations. This variations can be seen in Fig. 3.4 where the calculated density is plotted for different slices of the simulated data. The standard deviation

$\delta = \left(\frac{1}{N-1} \sum_{j=0}^{N-1} (x_j - \bar{x})^2 \right)^{\frac{1}{2}}$ depends on d and is smaller than 1% for $d > a$ (cf. Fig. 3.5).

The problem of this method is that d is not always known in the experiment. The effective illuminated slice width depends on many different factors. Among them are the complicated shape of the laser beam profile and the laser profile, the “cutting level” used in the particle detection technique and on the amount of light scattered by every particle. The scattered light intensity depends on particle size. Therefore the true shape of the projected volume has to be determined for every combination of laser, particle size and detection software. Additional errors are introduced by the “shadowing” effect: the observed particle images are finite in size and can overlap in the 2D image. It will reduce the calculated density.

3.2.3 Pair correlation function

It would be preferable to use a method to estimate the density in a way that is insensitive to the geometry of the laser illumination. This can be done assuming that the particles in a complex plasma are not randomly distributed but are structured. To analyze this structure in the simplest way the pair correlation function $g(r)$ can be applied. For a random point distribution $g(r) = 1$ for all r . If the distribution has a lattice structure or is hexatic or liquid like then $g(r)$ has a first maximum at the most probable distance a_g of the next neighbor. By knowing the structure the density can be calculated from the packing density.

$$n = k a_g^{-3}$$

here k is the structure factor that depends on the volume attributed to a single particle in the structure. Different values of k are shown in table 3.1. The values of k are 1.27 for the random distribution described in method 1 and $k = 1$ for a simple cubic lattice. The more realistic structures have values from 1.3 to 1.4. So that even without knowing the exact structure the density can be calculated from a_g . The important question is whether it is possible to determine a_g having only a 2D projection of the actual 3D structure. Figure 3.6 shows the

3 Analysis methods

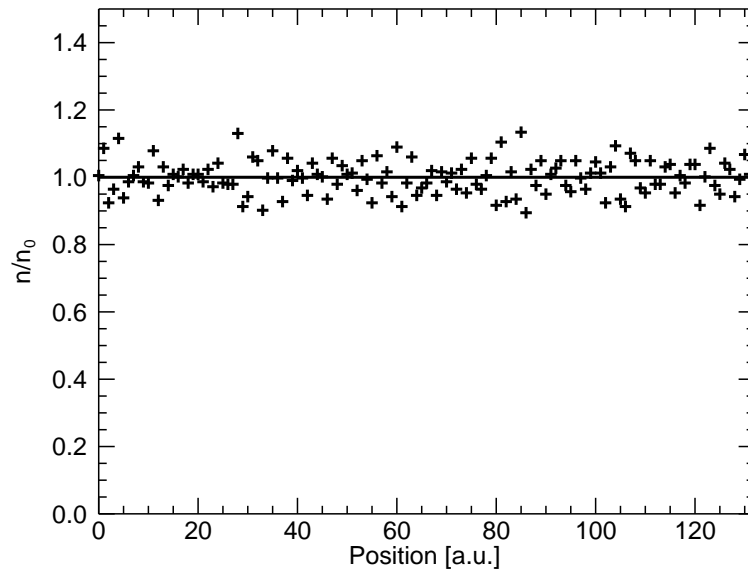


Figure 3.4: Particle density of the of a simulated particle cloud calculated from 2D projections with fixed width ($a/d = 0.25$) at different positions (marked with crosses) normalized to the density n_0 (black line). The method is described in section 3.2.2.

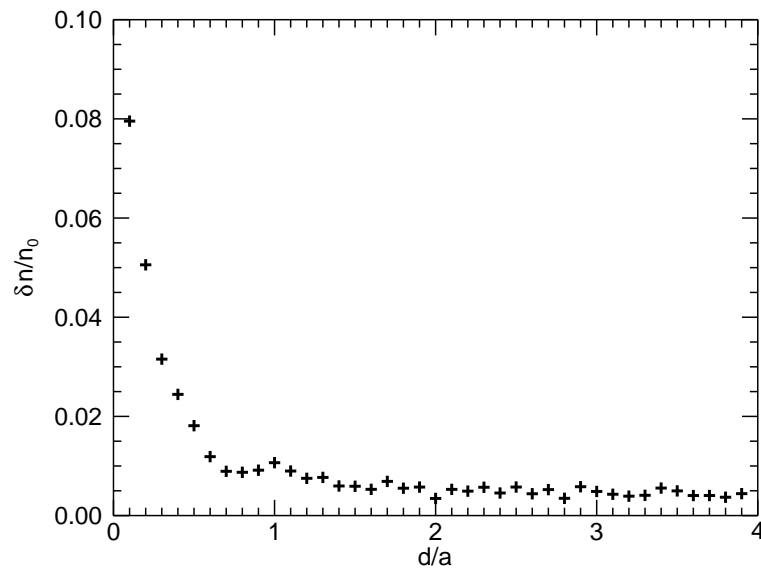


Figure 3.5: Deviation of the calculated density relative to the density n_0 for different projection width d normalized to the interparticle separation a . The position of the slice is fixed at the center of the volume.

Structure	n	a_g	k
simple cubic	s^{-3}	s	1
body centered cubic	$2s^{-3}$	$\frac{\sqrt{3}}{2}s$	1.3
face centered cubic	$4s^{-3}$	$\frac{s}{\sqrt{2}}$	1.41
simulation			1.27

Table 3.1: Structure factors for cubic structures. n is the number density, s is the lattice spacing.

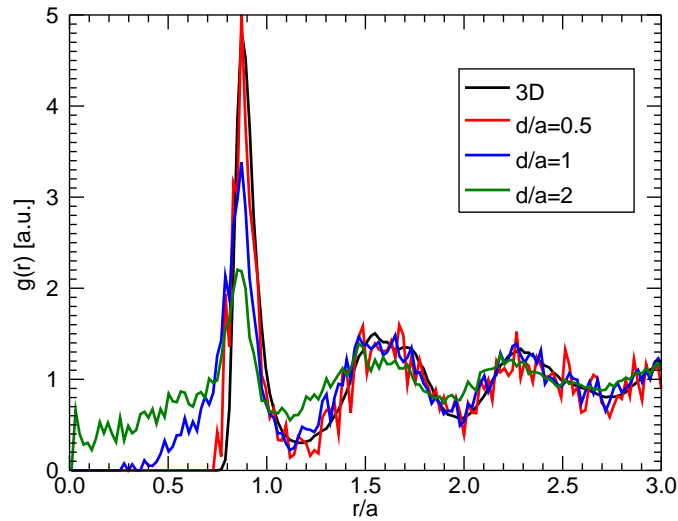


Figure 3.6: Pair correlation functions obtained from the simulated data in 3D (black line) and in 2D projections with different slice width d . The distances r and d are normalized to the average interparticle separation a . The position of the first peak is $a_g = 0.85$ and has almost no dependence on d .

$g^{3D}(r)$ in comparison with the $g^{2D}(r)$ obtained for different slice width. Due to the projection the probability for small distances ($< a_g$) increases noticeable through the appearance of a wing on the left side of the first peak, that increases with d/a . Additionally the height of the first peak decreases for increasing d/a indicating a stronger disordering. However the position of the first peak is actually the same for 3D or 2D and does not depend on d/a .

This makes pair correlation function analysis a very powerful tool to determine the density of a complex plasma cloud from a recorded 2D image.

3.3 Determination of the laser profile

The PK-3 Plus setup allows a tomographic scan of the the particle system by moving the laser and camera relative to the plasma chamber. This is usually used to analyze three dimensional crystal structures. But the scans can also be used to analyze the profile of the illumination laser. This is accomplished by gridding the field of view of the camera and determining the average track length of the particles in the grid cell during the scan.

The results of such a analysis can be even more useful than a direct measurement of the laser with a photo diode since it contains not only information about the laser but also about the sensitivity of the camera and it also depends on the particle detection algorithm. Hence the obtained profiles could also be called “profile of the particle detection depth”. Since the biggest influence on the shape of the profile is the laser power distribution it is valid to call it “laser profile”. Another contribution to the profile is the particle size because smaller particles have a smaller detection threshold than bigger particles.

In the PK-3 Plus setup onboard the ISS two illumination laser are available and the intensity of the laser can be tuned by changing its duty cycle. So for precise measurements the profile has to be obtained for all combinations of particles and laser intensity. Due to limited experimental time on the ISS this was not possible up to now. It has also to be mentioned that the whole field of view of the camera has to be filled with particles to be able to make this measurement. This limits the possibility to conduct the measurement under gravity conditions.

The profile shown in Fig. 3.7 are obtained from an experiment with particles with $6.81 \mu\text{m}$ diameter. The maximal track length of $170 \mu\text{m}$ has been measured on the left side of the field of view, the side where the laser source is mounted. The shortest tracks are on the right side ($80 \mu\text{m}$) close to the focal line of the laser.

3.3 Determination of the laser profile

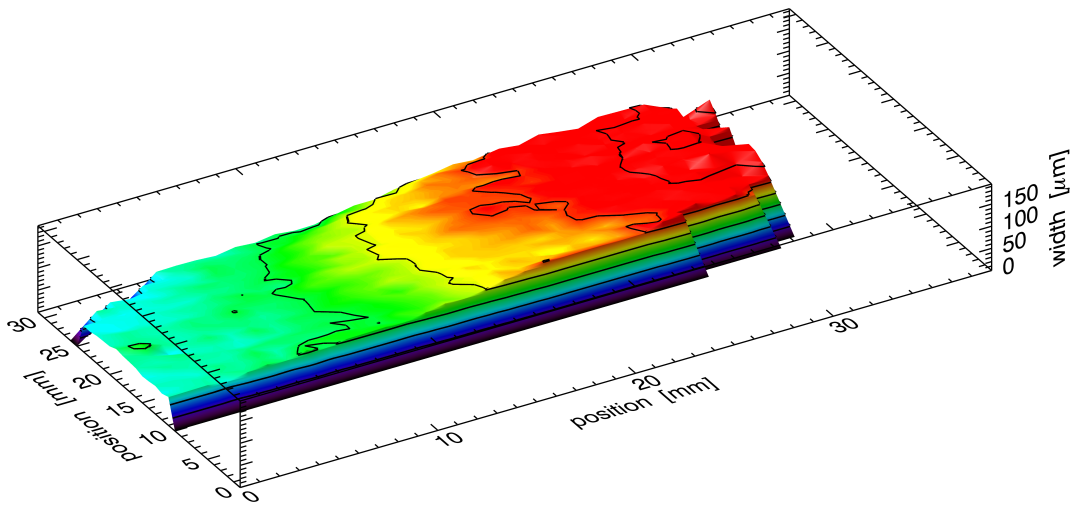


Figure 3.7: Profile of the illumination laser obtained from three dimensional scans. The measurements were made for the field of view of the “quadrant view” camera of the PK-3 Plus setup in microgravity on-board the ISS. The color indicates the width of the laser-illuminated volume. In particle free regions the width cannot be measured.

3 Analysis methods

4 Dissipative dark soliton

4.1 Theory

The history of solitons started 1834 when John S. Russell observed a “wave of translation” on the Union Canal in Scotland. He wrote about his observation:

“I was observing the motion of a boat which was rapidly drawn along a narrow channel by a pair of horses, when the boat suddenly stopped – not so the mass of water in the channel which it had put in motion; it accumulated round the prow of the vessel in a state of violent agitation, then suddenly leaving it behind, rolled forward with great velocity, assuming the form of a large solitary elevation, a rounded, smooth and well-defined heap of water, which continued its course along the channel apparently without change of form or diminution of speed. I followed it on horseback, and overtook it still rolling on at a rate of some eight or nine miles an hour, preserving its original figure some thirty feet long and a foot to a foot and a half in height. Its height gradually diminished, and after a chase of one or two miles I lost it in the windings of the channel. Such, in the month of August 1834, was my first chance interview with that singular and beautiful phenomenon which I have called the Wave of Translation” [55]

Important features of the observed wave were that it was stable over a very long distance without changing the shape. After his observation Russel conducted the first experiments in a water channel. For his experiments he inserted a plate vertically into the water channel and pressed it slowly forward. The displaced water in front of the plate formed a heap that traveled to the other side of the channel. [55]

With this experiments he was able to determine some more properties of the wave that is that the speed of the wave depends on the amplitude of the wave and on the water depth. He also found that two waves do not merge so that a bigger wave overtakes a smaller one.

The importance of solitons in modern physics is based on the finding that it is possible to explain the phenomenon by a balance of dispersion and nonlinear effects that can maintain a localized solitary wave and that integrable model systems exist that have soliton solutions. Most prominent systems are described by the Korteweg – de Vries (KdV) equation and the nonlinear Schrödinger (NLS) equation.

In general a soliton can be described as a traveling wave packet that consists of a superposition of waves with different frequencies. Their composition can

4 Dissipative dark soliton

be analyzed by Fourier transformation. In a dispersive medium waves with different frequencies travel with different speed so the wave packet dissolves with time. Nonlinear effects in the medium can at the same time transform waves of different frequency into each other. For a particularly shaped wave packet these two effects can cancel each other out and the wave can travel unperturbed through the medium.

Different media can have different nonlinear effects so the soliton solutions can have different shapes.

The first analytical soliton solution was found for the Korteweg – de Vries equation:

$$\partial_t \Phi + \partial_x^2 \Phi + 6\Phi \partial_x \Phi = 0. \quad (4.1)$$

It is a mathematical model for waves on shallow water surfaces.

A solution of this equation that describes a wave with fixed shape is:

$$\Phi(x, t) = \pm \frac{1}{2} c \cosh^{-2} \left[\frac{\sqrt{c}}{2} (x - ct - b) \right] \quad (4.2)$$

The wave travels with the phase speed c through the medium and speed of the wave depends on the amplitude, b is an arbitrary constant.

The solution can be obtained by the inverse scattering transform which is not only a method for solving the KdV equation but also many other non-linear partial differential equations. The inverse scattering transform is a non-linear generalization of the Fourier transform which is used to solve linear partial differential equations. With the inverse scattering transform the term soliton can be more restricted as a class of reflection less solutions of equations that are integrable via that method.

One important representative of this kind of equations is the nonlinear Schrödinger equation which is a classical field equation with numerous applications for example in optics and in water waves. The nonlinear Schrödinger equation is:

$$i\partial_t \Psi + \frac{1}{2} \partial_x^2 \Psi + (V(x) + k |\Psi|^2) \Psi = 0. \quad (4.3)$$

As in the kdV equation $\frac{1}{2} \partial_x^2 \Psi$ is the dispersion term, $V(x)$ is the potential energy and k relates to the strength of the nonlinearity. The sign of k depends on the type of interaction between the particles that is described with the model. For $k > 0$ the inter-particle forces are repulsive for $k < 0$ the forces are attractive.

Depending of the sign of k the NLS has two families of soliton solutions. For repulsive particles ($k > 0$) the solution is given by a **bright soliton**. Here the traveling wave consists of a local maximum in the density distribution $|\Psi|^2$. A bright soliton has the following form:

$$\Psi(x, t)_{bright} = A \sinh[A(x - vt)] \exp \left[-i(vx + \frac{1}{2}(a^2 - v^2)t) \right] \quad (4.4)$$

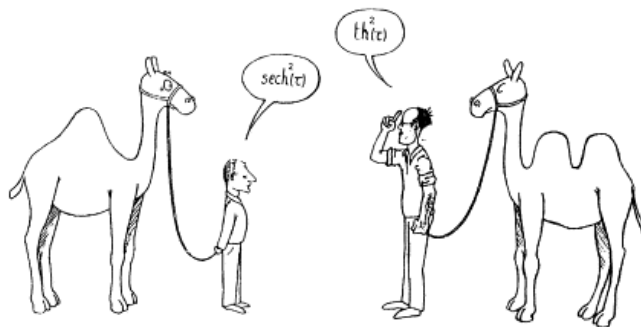


Figure 4.1: Dark and bright solitons by Marc Haelterman in 1989 [56].

Here A is the amplitude and v is the speed of the wave. A and v are here independent which is a main difference to KdV solitons.

For attractive particles ($k < 0$) a new type of stable solution appears: the **dark soliton**. It has the form:

$$\Psi(x, t)_{dark} = A \tanh[A(x - vt)] \exp[-i(vx + \frac{1}{2}(a^2 - v^2)t)] \quad (4.5)$$

A dark soliton is a traveling local minimum in the density distribution $|\Psi|^2$.

The soliton described in this work is also of the refractive type which means it is also a dark soliton but it can not be described by equation 4.5.

The main reason for this is that three dimensional complex plasmas are dissipative systems because of the neutral gas drag (see. Sec. 1.3.2). The NLS does not contain a damping term.

There are two principal effects of dissipation in a physical system. The first is that dissipation affects the behavior of phenomena that also occur in conservative systems. Here damping is responsible for energy loss and can be treated as a perturbation. This implicates that in dissipative systems the classical concept of solitons can still be used at least at short time scales where the loss of energy can be neglected.

Second, dissipation can also play a more fundamental role and can be the cause of new structures that do not exist in conservative systems. These structures disappear if dissipation is switched off [57]. This gives rise to a new class of solitons where dissipation is essential for the formation and the stabilization of the soliton. This new type of solitons - **dissipative solitons** - can exist for unlimited time even with strong damping. This is only possible in open systems where energy or matter can flow into the system. If this flow is stopped the soliton disappears. These important properties are certainly fulfilled in the case of 3D complex plasmas. The high damping rates make them strongly dissipative and the constant energy input from the generator to sustain the plasma makes them open systems with the potential to support these types of structures.

The general idea behind dissipative solitons is much wider than the strict definition of classical soliton solutions obtained only by the inverse scattering

transform. Dissipative solitons are also allowed to change in time or to be stationary like spots or pulses. This more general definition makes the concept much more applicable in real physical systems but makes them much harder to describe mathematically. Many systems that are capable of producing dissipative solitons cannot be described by a mathematical model employing a single equation. But in some cases this is possible, one example is the Burgers equation.

$$\partial_t \Phi = \partial_{xx} \Phi - \Phi \partial_x \Phi = \frac{d}{dx} \left(\partial_x \Phi - \frac{1}{2} \Phi^2 \right), \quad (4.6)$$

which has a special type of diffusion on the right hand side and still has a soliton solution:

$$\Phi = b \exp \left(\frac{1}{2} b (bt - x) \right) \cosh^{-1} \left(\frac{1}{2} b (bt - x) \right) \quad (4.7)$$

The search for similar simple mathematical description of complex plasmas is one of the key stones in complex plasma research. This makes the experimental discovery and description of solitons a very important task. In the publication “Dissipative Dark Soliton in a Complex Plasma” [1] the discovery of a new type of solitons in complex plasmas is described and a detailed description of the phenomenon is presented. Relations with previous findings of similar experiments in our field and in other fields is also shown.

The finding was strongly supported by the discovery of a very similar wave in completely different discharge type. The first observation occurred in an RF discharge of PK-3 Plus described in Sec. 2.2 and the second in a DC-discharge in PK-4 (see Sec. 2.7).

The observed wave in PK-4 is described in “Dissipative dark solitons in a dc complex plasma” [2]. All details of the analysis methods and the experimental setups are described in the previous sections.

4.2 Experiments and results

4.2.1 Dissipative dark solitons in a rf complex plasma

In the following publication which is attached to this thesis the dynamics of nonlinear solitary waves in a complex plasma is described and analyzed.

- R. Heidemann, S. Zhdanov, R. Sütterlin, H. M. Thomas, and G. E. Morfill. Dissipative dark soliton in a complex plasma. *Phys. Rev. Lett.*, 102(13):135002, Mar 2009.

The wave propagation was observed in a high density, three dimensional microparticle cloud. The microparticles were embedded in a neon rf gas discharge.

The most significant property of the wave was that it was dominantly rarefactive. That means that the particle density within the wave is decreased not increased. Based on the comparison of the wave with theoretical predictions and due to the rarefaction it was possible to identify the wave as a dark soliton. Furthermore the medium in the experiment was highly dissipative, the damping time is much shorter than the wave propagation. This leads to a more precise classification of the wave as a dissipative dark soliton (DDS). Previous publications about solitons in complex plasmas cover experiments with bright solitons in 2D complex plasmas consisting of a single mono layer of microparticles [58]. In these experiments the solitons were excited by a voltage pulse to a wire that was placed inside the plasma chamber slightly below the plane of microparticles. Experiments with solitary waves in 3D complex plasmas are reported in [59, 60, 61]. The described wave phenomena are large amplitude dust acoustic waves and compressive shock-waves that were excited by gas-dynamic impacts and electromagnetic impulses. The waves were analyzed using image intensity profiles. The analysis of individual particle kinetics could not be presented. To our knowledge there are no previous publications about dark soliton experiments in complex plasmas. The majority of dark solitons experiment in other fields concern optical solitons that are associated with wave envelopes [56, 62]. Acoustic type dark solitons are reported in Bose-Einstein condensates [63].

Experimental setup and conditions For the experiments a modified version of the PK-3 Plus setup described in section 2.2 was used. The experiments were performed in the laboratory on ground. Thermophoresis was used to partially compensate the gravitational force on the particles. The temperature difference between top and bottom electrode was set to 15 K. Since dissipation plays an important role in the wave formation and wave propagation the choice of the working gas and pressure is important. Because of that we compared argon and neon and finally analyzed a series of eight experiments with neon at different pressures in a range from 20 Pa to 35 Pa . Below 20 Pa the particle system gets perturbed by self excited waves [64]. Above 35 Pa the neutral gas damping is so strong that the wave propagation is prohibited. For the reported experiments the effective rf-voltage on the electrodes was set to 13 V. For the microparticles we chose $3.42 \mu\text{m}$ melamine-formaldehyde particles. The particle motion was recorded with a high speed camera with 1000 frames per second. The camera had a resolution of 1024×1024 pixels. The used optics allowed for a spatial resolution of $26.8 \mu\text{m}$ per pixel.

Wave excitation A dc bias of 8.6 V has been applied to both electrodes with the use of a function generator. The bias compressed the particle cloud vertically. The wave propagation was triggered by switching the bias off.

Description of the wave The wave propagates from top of the particle cloud to the bottom. Particles within the wave in the depletion zone are accelerated upwards and then decelerated in a sedimentation front. The particle motion is opposite to the direction of propagation. The wave is visualized in the publication by snapshots and diagrams of the tracked particle position. The waves dynamics is illustrated by a time-plot that shows the vertical particle density distribution against time.

The temporal sequence of the wave formation after switching of the voltage bias starts with the acceleration of the first particle layer into the empty region above the particle cloud followed by the second and further layers. The fast moving particles with average velocities up to 45 mm/s form the rarefaction zone. The particles are stopped suddenly in a sedimentation front. At higher gas pressure (> 24 Pa) the particles settle layer by layer. At lower pressures the accelerated particles penetrate the sedimentation front up to five layers deep resulting in a bidirectional flow and a change in the particle number distribution $N_y(t)$. The propagation speed of the wave was ≈ 20 mm/s

Wave properties The tracking of individual particles allowed us to resolve the wave at the kinetic level. With this it was possible to derive physical quantities that are hard or impossible to observe in other physical systems. For example it was not only possible to derive the propagation speed of the wave but also the complete velocity distribution of the constituting particles. In the publication we presented the measurements of the particle number distributions that have been calculated for all time-steps (frames) and all experiments and compare them with the undisturbed distributions. We also presented the particle velocity distributions and compare them with theoretical predictions. All notable features of the distributions are described in the publication.

We identified three parameters that characterize the soliton at any moment: the amplitude of the velocity distributions, the width of the velocity distributions and the instantaneous propagation velocity. The initial amplitude of the DDS depended strongly on the neutral gas damping. The highest value was measured at the lowest gas pressure 20.4 Pa with 45.0 mm/s. At higher pressures (> 30 Pa) the initial amplitude was smaller than 5 mm/s. The amplitude of the wave changes during propagation with a constant rate. For pressures below 20 Pa the amplitude increases with time. This indicates a weak instability of the wave which may be connected to nonlinear global modes [64, 65]. At pressures around 22 Pa the wave propagates without changing the amplitude. At higher pressures the amplitude decreases with time but its damping rate is still much lower than the Epstein damping rate for the given pressure.

The width of the wave was independent of pressure and has an average value of approximately 0.7 mm. The propagation speed of the wave was also independent of the gas pressure and had an average value of 20 mm/s. Additionally we

determined the “grayness” of the dark soliton that is the decompression ratio defined by the ratio of the number density within the rarefaction zone to the density of the undisturbed particle cloud. The highest value measured was a factor of 7.8.

All mentioned parameters and distributions were calculated for every time-step of 10^{-3} s in all eight experiments. This yields about 500 measurements per parameter per experiment. Most of the values presented in the publication are averaged values over the 500 single measurement.

Many more experiments with dark solitons were conducted since the publication on ground and also in parabolic flight experiments and on the International Space Station which confirms a very good repeatability. One of these experiments of particular interest was the observation of a dissipative dark soliton in PK-4. This is significant because it means that these type of waves can not only be created in rf-discharges but also in a dc complex plasma. The experiment is described in the next section.

4.2.2 Dissipative dark solitons in a dc complex plasma

In the following publication which is also attached to this thesis a dissipative dark soliton is described that has been observed in a DC-discharge in the PK-4 setup.

- S. Zhdanov, R. Heidemann, M. H. Thoma, R. Sütterlin, H. M. Thomas, H. Höfner, K. Tarantik, G. E. Morfill, A. D. Usachev, O. F. Petrov, and V. E. Fortov. Dissipative dark solitons in a dc complex plasma. *EPL (Europhysics Letters)*, 89(2):25001, 2010.

The experiment series has been performed during a DLR Parabolic flight Campaign onboard the A-300 ZERO-G plane. The wave was excited in a dense three dimensional complex plasma in a neon gas discharge. The reduced gravity provided a huge homogeneous particle cloud that was not compressed on the chamber walls as it would be in a ground bases experiment.

Experimental setup and conditions The experiments were performed in the PK-4 setup described in section 2.7. For the experiment the gas pressure was set to 18 Pa. Previous to the experiment the gas was continuously renewed with a flow rate of 0.3 sccm while the experiment the flow was switched off. The used melamine formaldehyde particles had a diameter of $3.43 \mu\text{m}$, the same size as in the RF-DDS experiment (see section 4.2.1). The neutral gas damping rate for this pressure and particle size was calculated to $\gamma = 41 \text{ s}^{-1}$. The injected particle cloud was hold in place by polarity switching at a frequency of 1 kHz with a 50% duty cycle. In this experiment a diode laser with an output power of 20 mW and a wavelength of 686 nm was used to illuminate an approximately

4 Dissipative dark soliton

100 μm thin sheet of the particle cloud. The scattered light was recorded with a CCD-camera with a framerate of 60 Hz and a resolution of 640 x 480 pixels. The used optics allowed for a resolution of 33 μm per pixel.

The setup made it possible to determine the position of the particles and to track the particles from frame to frame. On average 2650 ± 120 particles were registered per frame. The mean particle density was $\langle n_d \rangle = (7 \pm 1) \cdot 10^4 \text{ cm}^{-3}$. With the plasma parameters shown in description of the PK-4 setup in section 2.7 the particle charge Z was estimated to be in the range between 5000 and 7000 elementary charges using the DML approximation (cf. section 1.3.1).

Soliton excitation The soliton was excited by a short voltage pulse on the electrical manipulative (EM) electrode that is mounted around the glass cylinder. After the excitation the wave propagated in horizontal direction parallel to the glass tube.

Description of the soliton The observed wave has similar properties to the soliton observed in the RF-complex plasma (section 4.2.1). The particles entering the wave are accelerated and constitute the rarefaction zone. Then they are decelerated forming a sedimentation front and relax in their new equilibrium position. The soliton propagation is visualized in the publication with the help of snapshots from the recorded movies and space-time plots. These plots illustrate the soliton width and the propagation speed.

The map of the longitudinal velocity distribution of the particles versus time illustrates the single particle kinetics. The velocity distribution inside the soliton at a fixed time moment has the shape of an inverse squared hyperbolic cosine:

$$V = A \cosh^{-2} \left(\frac{x - x_0}{\delta L} \right),$$

where A is the amplitude, $2\delta L$ is the width and x_0 is the position of the soliton. The shape is similar to classical soliton solutions.

The damping rate of the soliton amplitude in the analyzed experiment has a decay rate of $\gamma_{damp} = 3.1 \pm 0.6 \text{ s}^{-1}$. The damping of the amplitude of the soliton is 14 times smaller than the damping from the neutral gas. In fact the frictional kinetic energy dissipation rate is approximately 10 times bigger than the change rate of the kinetic energy in the soliton. In this overdamped case it is possible to derive the effective force on the particles:

$$ma = \sum_i F_i,$$

where m and a is the mass and the acceleration of the particles. The known component of the forces F_i is the friction force. All other forces can be approx-

imated with an effective electric field E_{eff}

$$ma = -m\gamma v + eZE_{eff},$$

where v is the velocity and eZ the charge of the particle. If the acceleration is small compared to γv it can be neglected:

$$m\gamma v = eZE_{eff}$$

This means that the velocity distribution of the particles $v(x)$ is proportional to the effective electric field:

$$v(x) \propto E_{eff}(x)$$

In the given experiment this means that the electric field inside the soliton can be derived from the measured particle velocity profile.

In the publication the main author applies the same reasoning to the whole cloud and derives as first approximation a parabolic confinement for the whole particle cloud. The confinement field is characterized by the confinement frequency Ω . The calculated Ω from the particle kinetics changes between 7 s^{-1} to 13 s^{-1} indicating a slightly asymmetric confinement.

The anomalously low damping of the solitons amplitude compared to the neutral gas damping is already known from the soliton in rf-complex plasma. Also the propagation speed of the soliton was comparable in this experiment it was measured to $C_{DDS} = 15 \pm 1\text{ mm/s}$

The similarities of the dissipative dark soliton in dc- and rf-complex plasma are surprisingly detailed, in spite of the very different discharge condition resulting in a totally different global particle confinement. The experiment in rf-conditions was performed with thermophoresis the dc-experiment was performed in micro gravity conditions.

4.3 Conclusion

A new type of wave in three dimensional complex plasmas has been observed and described. The observation of the dissipative dark soliton has sparked interest in the field of complex plasmas and also in other fields.

It has been connected to the theoretical investigation of nonlinear dust acoustic waves [66, 67, 68] and the theoretical and numerical investigation of soliton solutions of the nonlinear Schrödinger equation with a dissipative term that arises due to dust charge variations [69]. It has also been used as an example in the experimental investigation of other dissipative phenomena like lane formation and phase separation [70] and for the investigation of nonlinear synchronization of self-excited dust density waves [71].

4 Dissipative dark soliton

Our observation of the dissipative dark soliton in complex plasmas was also recognized in other fields for example the investigation of dark solitons in Bose-Einstein condensates [72] and also in the field of quantum fluids where dark solitons have been observed in dissipative polariton gas [73].

Future investigations on the subject are already enroute, experiments for the excitation of DDS were performed in micro gravity conditions in parabolic flights and on the International space station with the PK-3 Plus setup. The results of the investigations will give a broader view on the new topic.

5 Heartbeat

In many experiments that were performed with the PK-3 Plus setup on board of the International Space Station the so called heartbeat instability could be observed. Under microgravity conditions the microparticles in a complex plasma arrange themselves in a vast cloud that spreads nearly all over the available inter-electrode space. In the middle of the plasma chamber a void is often formed. The void is completely free of particles. Under certain conditions the complex plasma becomes unstable and rhythmically pulsates in the radial direction. In given experiments the instability has been observed in a wide parameter range. Detailed knowledge of the heartbeat instability is vital for the planning and conducting of experiments in microgravity and in the laboratory. The appearance of heartbeat prevents other experiments for example it hinders the formation of crystalline structures.

5.1 Experiments and results

Eighteen experiments are discussed and analyzed in the following publication which is attached to this thesis.

- R.J. Heidemann, L. Couédel, S.K. Zhdanov, K.R. Sütterlin, M. Schwabe, H.M. Thomas, A.V. Ivlev, T. Hagl, G.E. Morfill, V.E. Fortov, V.I. Molotkov, O.F. Petrov, A.I. Lipaev, V. Tokarev, T. Reiter, and P. Vinogradov. Comprehensive experimental study of heartbeat oscillations observed under microgravity conditions in the PK-3 Plus laboratory on board the international space station. *Physics of Plasmas*, 18(5):053701, 2011.

The measurements were performed with MF particles of different diameters from $6.81\ \mu\text{m}$ to $15\ \mu\text{m}$ in Argon as well as in Neon plasma at different discharge powers. The gas pressure varies between 8Pa and 100Pa. The frequency of the observed oscillation ranges from 0.8Hz to 7Hz. The oscillation frequency increases linearly with plasma power and with the neutral gas pressure. The correlation of the particle motion and the recorded plasma parameters is discussed.

In the second publication on this subject which is also attached to this thesis one of the experiments from the first publication is discussed in greater detail.

- S.K. Zhdanov, M. Schwabe, R. Heidemann, R. Sütterlin, H.M. Thomas, M. Rubin-Zuzic, H. Rothermel, T. Hagl, A.V. Ivlev, G.E. Morfill, V.I.

Molotkov, A.M. Lipaev, O.F. Petrov, V.E Fortov, and T. Reiter. Autooscillations in complex plasmas. *New Journal of Physics*, 12(4):043006, 2010.

In this second paper the emphasis is on “oscillons” a wave like phenomenon in the complex plasma cloud that is connected to the heartbeat oscillation.

5.2 Interpretation of the observations: a dynamical model of the heartbeat oscillations

The observation results obtained over a wide range of experimental conditions with the PK-3 Plus setup discussed in both publications allows to draw important conclusions on complex plasma dynamical features. In particular, they enable to formulate a model with the intention to describe the dynamics of the heartbeat oscillations. In the following chapter the phases of the heartbeat are discussed and connections with physical parameters are made. Followed by a comparison with the experimental results. Predictions from this model are shown to agree well with experimental findings.

5.2.1 Main phases of the heartbeat oscillation cycle

In short, the “heartbeat” sequence can be described as follows. Each cycle of the stable heartbeat oscillation begins with an enhanced plasma glow in the central area (corresponding plasma glow measurements are shown in the publication). Then the microparticles start to accelerate towards the center, entering the void; the plasma glow diminishes. Inside the void region the microparticles decelerate, until, after some advance, they turn around and start leaving the void area again. While the microparticles approach their starting positions, the glow intensity increases again, and the cycle restarts [48, 74]. It is convenient to divide this cycle into four phases (A to D).

A – enhanced ionization At the beginning of phase A the cloud is in the “maximal open void” configuration. At the void boundary the confining force $Z|e|E$ exerted on each microparticle from the global electric field $E = E_c$ is compensated by the ion drag force F_i . An enhanced glow appears in the central region while the glow intensity at the cloud edges decreases (see section III. C. “Plasma glow measurements” in 7.3). It is known, that an increase of the glow intensity is associated with an enhanced ionization [75]. Thus the change in glow intensity directly relates to a global alteration of the ion and electron densities, enhanced in the center. The increase of the density gradient is responsible for an enhanced ambipolar electric field $E = E_c + E_h(t)$. The rise-time of $E_h(t)$ is of the order of

5.2 Interpretation of the observations: a dynamical model of the heartbeat oscillations

the electron diffusion time $\tau_{De} \approx 10 \mu s$. This results in a force imbalance $Z|e|E > F_i$ at the void boundary, effecting the microparticle acceleration and their advance into the void.

We designate as τ_{E_0} the duration of this active stage of the enhanced ionization. This time is shorter than the video frame exposure time of the glow camera, giving an upper limit of $\tau_{E_0} < 1/50$ s.

B – decay of $E_h(t)$ During this phase the microparticles accelerate into the void. There, by capturing electrons, the microparticles lower the electron density and thereby decrease the ionization rate. The timescale for the charging of the microparticle is in the order of a few μs [76].

The electric field $E_h(t)$ decays due to the ion (ambipolar) diffusion in

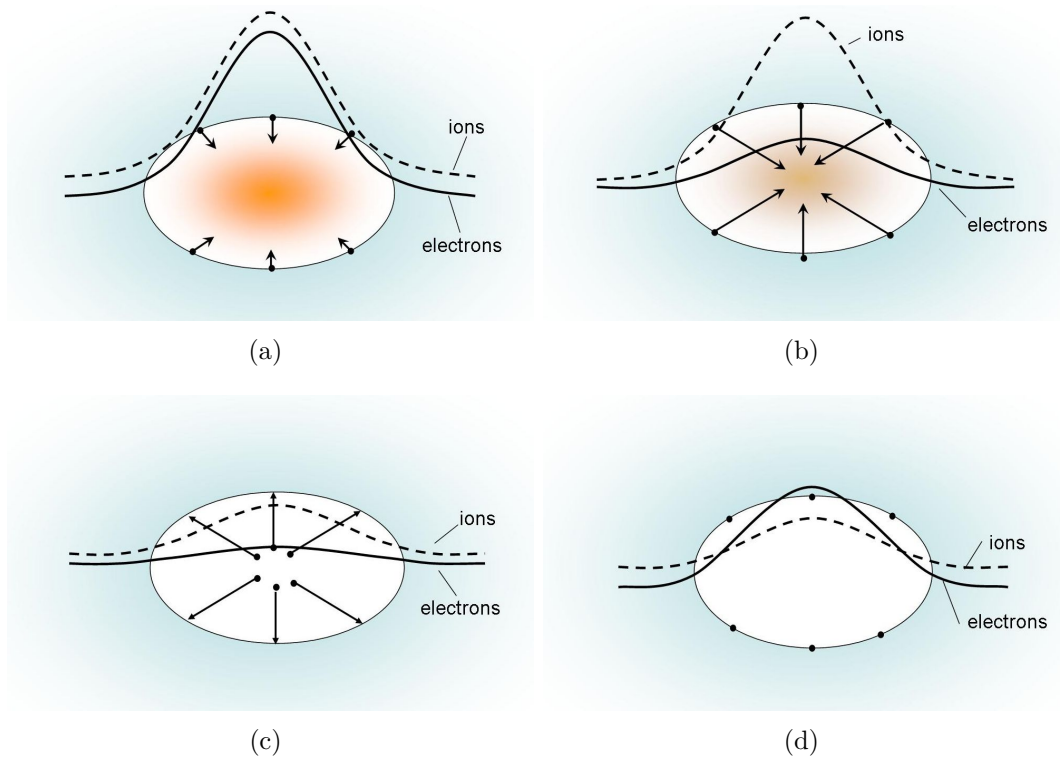


Figure 5.1: The different phases of a heartbeat oscillation. a) The Cycle starts with enhanced glow in the void center that leads to a higher ion and electron density. b) The microparticles are accelerated towards the center in the ambipolar electric field. By doing so they decrease the ionization rate. c) Ion drag is pushing the microparticles outwards. d) The absence of microparticles leads to a higher electron density which triggers a higher ionization rate and so phase A starts again.

the time $\tau_{Di} \approx 1 - 20$ ms. Still the microparticles continue to accelerate towards the center. Although τ_{Di} is short, the affected microparticle velocities and displacements are not negligible. At the end of this phase the ambipolar field enhancement E_h vanishes.

- C – enhanced ion drag** The ion drag force is now stronger than the confining force, becoming the main force component acting on the microparticles. By inertia, the microparticles continue their advance into the void region, steadily decelerated by the ion drag force and neutral gas friction. The microparticles eventually reverse the direction of motion and drift outwards. The smaller the total force, the lower the microparticle drift velocity in this phase. Therefore the reopening time is imposed by the difference between the strength of the confining field and the ion drag force.
- D – restoration of initial conditions** As the microparticles approach the starting positions which they occupied at the beginning of phase A a significant amount of microparticles has left the void. Electron losses to the microparticle surface decreases, the electron density increases, and finally the conditions triggering an explosion of the ionization rate in an avalanche process reappear, restarting the cycle again with phase A.

5.2.2 Dynamical model of microparticle motion

As described in the introduction (section 1.3) the microparticle dynamics is determined by the electric forces, the ion drag force and the neutral gas drag force (the Epstein drag force [37]) acting on the microparticles. Therefore it is straightforward to describe the motion of a particle, vibrating at the void boundary, by the following model equation:

$$\frac{d\mathbf{v}_d}{dt} = \frac{-Z|e|}{m_d}(\mathbf{E}_h(\mathbf{r}, t) + \mathbf{E}_c(\mathbf{r})) - \gamma\mathbf{v}_d + \frac{\mathbf{F}_i(\mathbf{r}, t)}{m_d}, \quad (5.1)$$

where \mathbf{v}_d is the microparticle velocity, Ze the microparticle charge, e the elementary charge, m_d the microparticle mass. γ is the damping rate of the Epstein drag force, and $\mathbf{F}_i(\mathbf{r}, t)$ is the ion drag force. The electric field can be divided into two parts: a time independent global confinement field $\mathbf{E}_c(\mathbf{r})$ and the pulsating electric field enhancement $\mathbf{E}_h(\mathbf{r}, t)$ that arises due to the instability

In the following the one dimensional motion of one single test microparticle is discussed. The particle is initially located in the vicinity of the void boundary

The x-axis is pointing away from the void center and its origin is given by the initial microparticle position before the instability. To further simplify the problem a parabolic confinement of the microparticles in the plasma is assumed, so that $E_c(x) = (x + x_0)E'$, where $E' = \text{const}$ characterizes the strength of the confining field and where x_0 is the position of the test microparticle before the

Table 5.1: Modeling parameters for the calculated trajectories shown in Fig. 5.2 and 5.3.

Nr.	E' V/cm ²	γ s ⁻¹	Z	E_0 V/cm	τ_{Di} ms	τ_{E_0} ms
I	15.2	57	9800	2.33	1	20
II	8.3	57	9800	3.33	1	20
VI	5.1	11	9000	2.5	1	20

instability starts. As a model assumption, we assume that the ion drag force F_i varies only very little in space and time. Therefore this force component is considered to be constant. Its value can be estimated from the force balance on the onset of the instability: $F_i = Z |e| E_c(0)$. The electric field enhancement at the void boundary is approximated by

$$E_h(x, t) = E_h(t) = \begin{cases} E_0 & 0 \leq t < \tau_{E_0} \\ E_0 e^{-\frac{t-\tau_{E_0}}{\tau_{Di}}} & \tau_{E_0} \leq t < \tau_{E_0} + \tau_{Di} \\ 0 & \tau_{E_0} + \tau_{Di} \leq t \end{cases}$$

representing the phases A – C.

This model has two free parameters: E' the scale of the confining electrical field, and E_0 the amplitude of the enhancement E_h . Both can be determined from the comparison of the model predictions to the observed microparticle trajectories. Note that E' is determined primarily by the frequency of the oscillation, whereas E_0 is directly related to the amplitude of the microparticle vibrations. These are two independent measurements. Hence E' and E_0 are well-defined, as a few examples discussed in the following section demonstrate.

5.2.3 Comparison with experiment

In the following section the dynamical model is compared with the microparticle motion during one cycle of the heartbeat oscillation. Numerical simulations were carried out for the parameters of experiments **I**, **II** and **IV** from the publication.

The modeling parameters E' , γ , E_h , Z , τ_{Di} and τ_{E_0} can be found in Table 5.1.

Fig. 5.2 and 5.3 show a comparison of the motion of a single microparticle with the predicted motion derived from the model (equation 5.1).

As can be seen in Fig. 5.2 and 5.3, the model is able to reproduce the main features of the microparticle motion: a fast motion towards the center of the void and a slower motion back to the equilibrium position.

It is worth noting that the value of E' can also be deduced from the frequency of the breathing mode (cf. according section in the publication). For

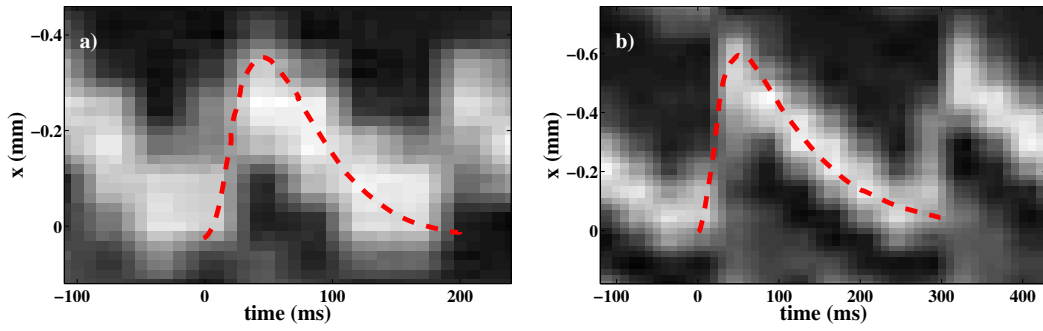


Figure 5.2: Comparison of the observed and simulated microparticle trajectories for (a) experiment **I** and (b) experiment **II**. The panels show cuts from the time-space plots, representing a complete oscillation of one microparticle. The dashed lines represent trajectories calculated with equation 5.1 for the parameters given in table 5.1.

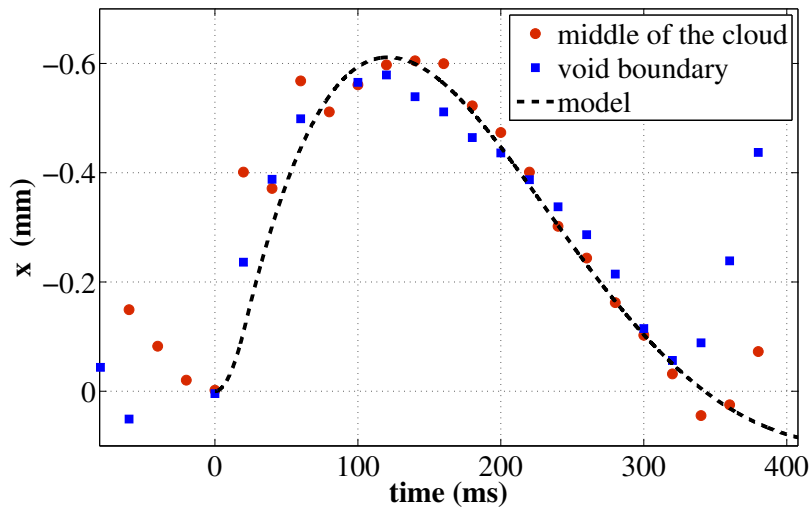


Figure 5.3: Comparison of the simulated microparticle trajectories (dashed line) with the tracked microparticle positions for experiment **VI**. Experimental parameters are listed in Table 1 in the publication. The microparticle trajectory taken in the middle of the cloud agrees better with the simulation than the trajectory at the void boundary.

experiments **I**, **II** and **IV**, $E'/E'_{bm} = 1 \pm 0.3$. This confirms the importance of confinement for the frequency of the heartbeat oscillation.

There are however some discrepancies which can be explained as followed: no precise measurements of plasma parameters exist and our calculations were based on estimates; the time τ_{E_0} of enhanced ionization in the void could not be measured accurately due to a too low frame rate during the experiments; a harmonic confinement was assumed; and variations of the ion drag force were completely neglected. The change in ion drag might be the reason behind the slightly different dynamics for microparticles on the void boundary and microparticles in the middle of the microparticle cloud (cf. Fig. 5.3).

Nevertheless it is worth noting that our simple model explains the microparticle dynamics fairly well in the case of weak heartbeat oscillations (as in experiment **I** and **II**, Fig. 5.2)) as well as in experiments with a strong (nonlinear) heartbeat oscillation with auto-oscillations (cf. **VI**, Fig. 5.3).

5.3 Outlook

More research needs to be done to fully understand the heartbeat instability. The presented model can already describe the oscillation itself. The next step is the explanation of the onset of the instability.

On the experimental side more investigations in ground based laboratories are needed with a higher framerate for the analysis of the particle motion. To resolve the fast contraction in the heartbeat cycle a framerate of 2000 to 3000 fps is required. Additionally a detailed mapping of the instability threshold is necessary. Specially the dependence of the threshold on the microparticle density. Promising experiments are already conducted although the excitation of the instability under gravity is complicated since the particles have to fill up a great part of the chamber volume for the instability to occur.

Several groups work at the moment on the theoretical description of the onset of the instability. An article with a possible explanation will be published from our group shortly. Such publications will open the next round for experimental research to confirm the theoretical predictions.

6 Interface Instability

The goal of the experiment discussed in this chapter is to use complex plasma as a model system for two interacting fluid flows and to analyze the microstructure of the flows on the atomistic level. This is accomplished by studying the kinetics of the constituent particles of a liquid complex plasma under shear. Of particular interest is to study the transition from laminar flow to disordered and turbulent flow. Additionally the properties of the interface between two flows, for example between resting and streaming fluids can be analyzed. In the phase of laminar flow the particles stream in parallel layers which do not intermix. In the turbulent flow the streams are disordered and the flow is chaotic. Vortices formed, interpenetration of the streamlines and lane formation occurred. By following single particle tracks in the transition zone between the two flow phases it is possible to determine the forces acting on the particles and to obtain dynamical quantities like the divergence of the velocity field of the fluid, the kinetic energy distribution and the enstrophy distribution within the transition zone. With these quantities it is possible to learn more about the cause of the breakup of the laminar flow. The experiments are reported in the following publication which is attached to this thesis.

- R. Heidemann, S. Zhdanov, K. R. Sütterlin, H. M. Thomas, and G. E. Morfill. Shear flow instability at the interface among two streams of a highly dissipative complex plasma. EPL (Europhysics Letters), 96(1):15001, 2011.

6.1 Theory

To characterize the liquid and the instability it is important to compare the forces acting inside the liquid. Of special interest is the relationship of the inertia forces to the viscous forces, that is the Reynolds number $Re = \frac{vL}{\nu}$, where \vec{v} is the velocity, L is the important scale length and ν is the kinematic viscosity. To calculate the Reynolds number the viscosity has to be measured. In the experiment in question this was possible to obtain from the spatial dependents of the vorticity ($\Omega = \Delta \times \vec{v}$) at the interface in the complex plasma. The spatial dependence of Ω can be derived from the momentum transport equation:

$$\frac{\partial \vec{v}}{\partial t} + (\vec{v} \cdot \nabla) \vec{v} = \nu \nabla^2 \vec{v} - \frac{\nabla p}{\rho} - \gamma \vec{v}, \quad \nabla \cdot \vec{v} = 0 \quad (6.1)$$

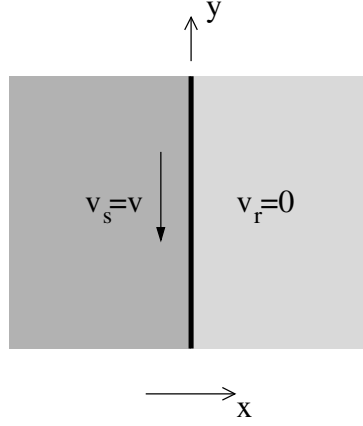


Figure 6.1: Sketch of the flow pattern for equation 6.3. The vertical interface is indicated by a thicker line. It separates the streaming particles on the left from the resting particles on the right. The flow is only inhomogeneous in x -direction.

where ν is the kinematic viscosity, $\rho = \text{const.}$ is the density and p the pressure of the liquid. For constant ρ and $(\vec{v}\vec{\nabla})\vec{v} = \vec{\nabla}\frac{v^2}{2} - \vec{v} \times \vec{\Omega}$ one gets by taking the curl of both sides of relationship (6.1):

$$\frac{d\vec{\Omega}}{dt} - \vec{\nabla} \times (\vec{v} \times \vec{\Omega}) = -\nu \vec{\nabla} \times \vec{\nabla} \times \vec{\Omega} - \gamma \vec{\Omega}. \quad (6.2)$$

The equation can be simplified for the flow pattern illustrated in figure 6.1. There is no flow perpendicular to the (x, y) -plane which reduces the problem to two dimensions. In two dimensions equation 6.2 is equivalent to:

$$\frac{d\Omega}{dt} = \frac{\partial\Omega}{\partial t} + (\vec{v}\vec{\nabla})\Omega = \nu \Delta\Omega - \gamma\Omega, \quad \Omega = \text{curl}_z \vec{v} = \frac{\partial v_y}{\partial x} - \frac{\partial v_x}{\partial y} \quad (6.3)$$

In the given experiment the vorticity distribution does not change along the interface, that is in y direction. So we assume $v_y \frac{\partial}{\partial x} \Omega = 0$. Additionally the flux at the interface is directed in the y -direction. So we assume $v_x = 0 \rightarrow v_x \frac{\partial}{\partial x} \Omega = 0$. Also the vorticity distribution is steady state yielding $\frac{d\Omega}{dt} = 0$. With that, the equation can be simplified to $\frac{\partial^2}{\partial x^2} \Omega = \frac{\gamma}{\nu} \Omega$. This can be solved yielding:

$$\Omega = A \exp\left(-\sqrt{\frac{\gamma}{\nu}} x\right).$$

This relationship implies that the kinematic viscosity can be determined by measuring the vorticity profile in the particle cloud. For the kinematic viscosity in the particle component of the complex plasma we obtained from the experimental data:

$$\nu \approx 10 \frac{\text{mm}^2}{\text{s}}$$

Note that in two dimensional complex plasmas the kinematic viscosity has been measured to be $1 \frac{\text{mm}^2}{\text{s}}$ by Nosenko et al. [77] and $130 \frac{\text{mm}^2}{\text{s}}$ by Gavrikov et al. [78, 79]. To derive the vorticity and divergence of the particle velocity field in the particle system one has in principle two options. The first one is to generate a regular gridded velocity field from the discrete velocities of the particles and then to calculate the spatial derivatives $\frac{dv_y}{dx}$ and $\frac{dv_x}{dy}$. A problem arises in the method by performing the gridding by either binning or by interpolation from the choice of the proper grid size. Especially if one is interested in obtaining the values on the scale of the interparticle separation. The second option is to define and calculate a discrete vorticity and divergence of the particle velocity field. This is the route followed in this work. Starting from the definition of divergence at a point P:

$$\text{div } \vec{v}(P) = \lim_{V \rightarrow 0} \int_{\partial(V)} \vec{v} \vec{n} \frac{dS}{V},$$

where V is a volume around P and $\partial(V)$ its surface and \vec{n} is the unit normal to the surface. For the case of two dimensional particle distributions we define a discrete definition of divergence by the relative radial motion of the nearest neighbors of one particle relative to its separation. We introduce:

$$(\text{div } \vec{v})_i = \frac{1}{n_i} \sum_{j=1}^{n_i} \frac{\vec{r}_{i,j} \cdot \vec{v}_{i,j}}{r_{i,j}^2}. \quad (6.4)$$

$\vec{r}_i = x_i \vec{e}_x + y_i \vec{e}_y$ are the particle positions in every frame, $\vec{r}_{i,j} = \vec{r}_j - \vec{r}_i$ are the vectors to the nearest neighbors derived by Delauney triangulation. $i=1 \dots N$, where N is the number of particles in a frame and $j=1 \dots n_i$, where n_i is the number of the nearest neighbors. The relative velocity $\vec{v}_{i,j}$ to the nearest neighbors is projected in radial direction $\frac{\vec{r}_{i,j}}{|\vec{r}_{i,j}|}$ and divided by their separation $|\vec{r}_{i,j}|$.

The vorticity is calculated similarly. The relative velocity is projected at the tangential direction $\vec{r}_{i,j}^\perp = \vec{e}_z \times \vec{r}_{i,j}$ which is orthogonal to $\vec{r}_{i,j}$, where $\vec{e}_z = \vec{e}_x \times \vec{e}_y$. Finally we define the discrete vorticity:

$$\Omega_i = \vec{e}_z \cdot (\mathbf{curl } \vec{v})_i = \frac{1}{nn_i} \sum_{j=1}^{nn_i} \frac{\vec{r}_{i,j}^\perp \cdot \vec{v}_{i,j}}{r_{i,j}^2}. \quad (6.5)$$

In this definition the vorticity is positive for counterclockwise rotation. With the help of (6.4) and (6.5) we can attribute a value for the local expansion, contraction and the local rotation to every particle in every frame on the natural scale of the interparticle separation. An integration of these values yields a description of the fluid at any larger scale. For example it can be used for the calculation of the kinematic viscosity or the calculation of the rotational part of the kinetic energy of the particles. To be able to measure the vorticity in a complex plasma it is necessary to determine the particle positions with high enough precision to be able to calculate the second derivative.

6.1.1 Instabilities

In the experiment the interface between a flow and a stagnation zone in a complex plasma is analyzed and an instability capturing the interface has been found. Possible reasons behind the breakup of the interface is the Kelvin-Helmholtz instability or the Rayleigh-Taylor instability. The dispersion relation describing the growth rate of the linear Kelvin-Helmholtz modes is:

$$\omega^2 - \left(2kv_r \frac{\rho_r}{\rho_r + \rho_s}\right) \omega + \frac{\rho_r}{\rho_r + \rho_s} k^2 v_r^2 = 0, \quad (6.6)$$

where ω is the oscillation frequency, k is the wavenumber, ρ_r and ρ_s is the densities of the resting and the streaming microparticle cloud and v_r is their relative velocity. The "classical" instability is driven by the pressure decrease that develops if streaming liquid has to flow around a "hump" growing at the interface: the flow velocity locally increases and the pressure decreases. This pulls the perturbation further into the stream.

In the conditions of the experiment in question the background damping is not negligible. Additionally interfacial surface tension stabilizes the short wavelength perturbations. Damping can be taken into account by replacing ω :

$$(\omega - kv_r)^2 \rightarrow (\omega - kv_r)((\omega - kv_r) + i\gamma),$$

where γ is the damping rate coefficient and i is the imaginary unit. The generalized dispersion relation is:

$$\omega^2 + \left(i\gamma - 2kv_r \frac{\rho_r}{\rho_r + \rho_s}\right) \omega + \frac{\rho_r}{\rho_r + \rho_s} (k^2 v_r^2 - i\gamma kv_r) - \frac{\alpha_r + \alpha_s}{\rho_r + \rho_s} |k^3| = 0, \quad (6.7)$$

where $\alpha_{r,s}$ are the surface tension coefficients. To test whether this type of instability is the main agent leading to the interface breakup, it is necessary to compare the observed increment of the instability with the maximal possible increment defined by (6.7). The increment is maximal at the wavenumber:

$$k_{max} = \frac{2}{3} v_r^2 \frac{\rho_r \rho_s}{(\rho_r + \rho_s)(\alpha_r + \alpha_s)}.$$

With this the maximal increment can be calculated yielding:

$$\Im\omega_{max} = \frac{1}{3} \frac{k^2 v^2}{\gamma} \frac{\rho_s / \rho_r}{(\rho_s / \rho_r + 1)^2}.$$

Substituting the experimental measured parameters, $v_s, \gamma, \rho_{r,s}$ and $k = 3 \text{ mm}^{-1}$ corresponding to the maximal growth rate it is found that $\Im\omega_{max}$ is 1–2 orders of magnitude less than expected [5]. Therefore the interface breakup can not be explained with this type of instability in our conditions. Experimentally it

was also found that increasing v_r does not make the interface more unstable which supports this result qualitatively.

Another possible explanation for the interface instability is the Rayleigh-Taylor type instability. Let us assume that the interface between the two liquids is destabilized by an effective acceleration acting perpendicular to the interface and that it is stabilized by surface tension. The dispersion relation of the Rayleigh-Taylor instability including damping is:

$$\begin{aligned}\Re\omega &\approx v_r k, \\ \Im\omega &\approx ka \frac{(\rho_r - \rho_s)}{(\rho_r + \rho_s)\gamma} - k^3 \frac{(\alpha_s + \alpha_r)}{(\rho_s + \rho_r)\gamma},\end{aligned}\quad (6.8)$$

where $\Re\omega$ and $\Im\omega$ are the real and imaginary part of the oscillation frequency, and a is the effective acceleration. The necessary strength of the acceleration can be calculated by substituting all measured parameters from the experiment. It was found that for the observed instability increment only an acceleration of $a = 0.3 \text{ m/s}^2$ is needed.

The effective acceleration can stem from the density difference in the two liquids and also a charge difference (see section 1.3.1). Then a small electric field in the discharge can cause the acceleration. Centrifugal forces of the flowing particles in the vortex can also be a destabilizing factor. The experimental determination of the acceleration source is challenging and an issue for future investigations. Nevertheless the calculation shows that a Rayleigh-Taylor type instability is a plausible cause of the observed interface breakup. Additionally it is worth noting that the Kelvin-Helmholtz instability, while not powerful enough for the long wavelengths, can result in growth of shorter wavelengths. Neglecting surface tension, the dispersion relation for this instability resolved for the wavenumber k is:

$$k = \sqrt{\frac{\Im\omega\gamma (\rho_r + \rho_s)^2}{v_r^2 (\rho_r \rho_s)}}. \quad (6.9)$$

It gives under our experimental conditions:

$$\lambda = \frac{2\pi}{k} \approx 0.4 \text{ mm} \approx 3\Delta.$$

as a typical length-scale, assuming $\Im\omega^{-1} \approx 1 \text{ s}$ as a typical time-scale. This is approximately three interparticle separations Δ . At this scale kinetic effects are important and assumptions made based on hydrodynamics leading to 6.9 become questionable.

This example shows once more that complex plasma experiments can play an important role in revealing physical phenomena that are at the boundary between hydrodynamics and kinetics where the discreteness of the medium plays an important role.

6.2 Experiments

An extensive amount of experiments has been conducted to study different kinds of complex plasma flows. The main difficulty while conducting the experiments is the topology, the orientation and structure of the particle fluxes, that have no simple dependence on the control parameters.

Even if the cloud is homogeneous enough the flow of the particles can be broken apart in smaller vortexes with small interfaces.

The best topology that is most suited for the analysis of the basic features of the interface and flow transitions is one with huge vortices and therefor extended interfaces. A very beneficial way to achieve this in the PKE-Nefedov laboratory is with a huge toroidal particle flow where the poloidal diameter of the flow is almost as big as the gap between the electrodes. This flow patterns are shown in Fig. 6.2.

An important advantage of this type of flow patterns is that they are steady state. That means that the flows can be observed for hours or in principle indefinitely long.

For a given flow topology the interfaces between streaming and resting particles can be very different. For example the interface can be completely laminar with almost no interaction between the two complex plasmas. Or on the contrary the mixing area can be very broad with almost no clear interface. An important result of the comparison of the different experiments is that the mixing strength between the flowing and resting complex plasmas does not strongly depend on the speed of the flowing particles at the interface.

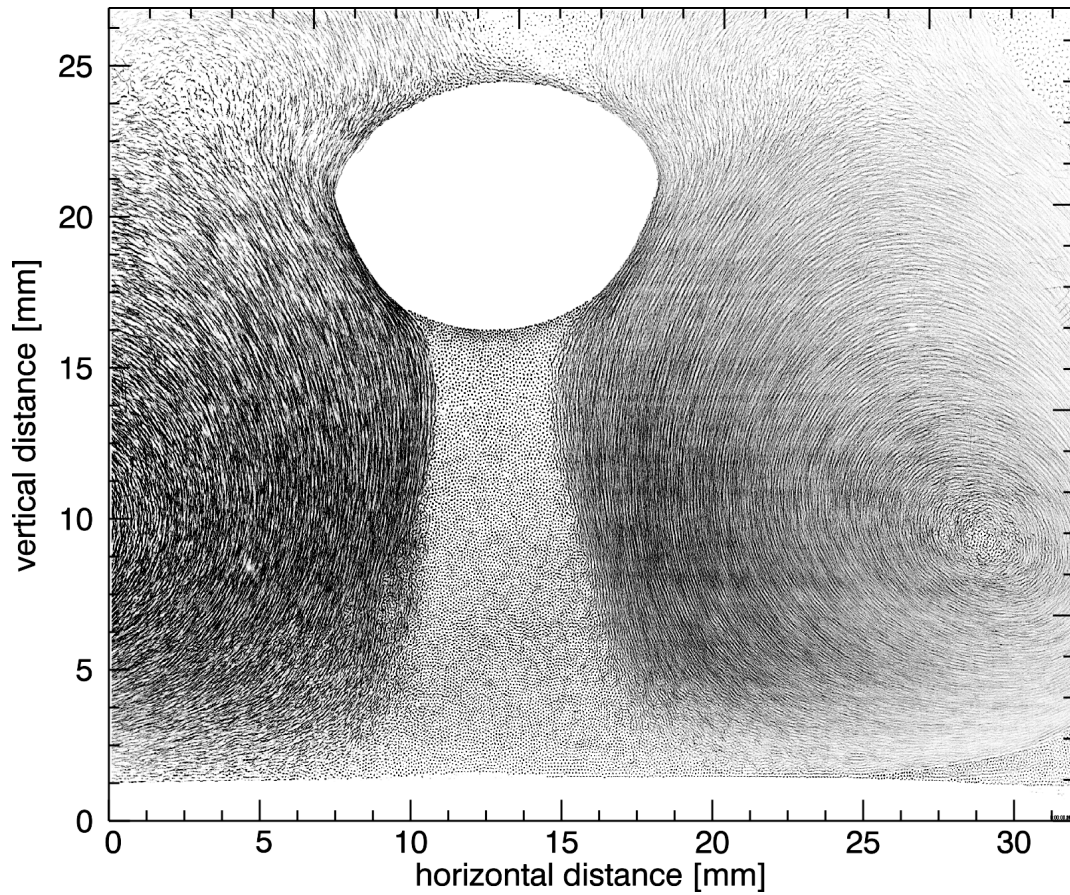


Figure 6.2: Overlay of 30 images recorded at 90 frames per second. The experiment was performed with particles with a diameter of $1.28\ \mu\text{m}$ in argon plasma at 55 Pa with an RF power of 1 W. The image shows the central cross-section of a toroidal vortex stream. The stream is visible due to the elongated particle tracks forming the concentric structures in the left and the right part of the image. The particle free void in the top center of the toroidal stream is an obstacle to the flow and a stagnation zone of resting particles is formed below the void. The interface between the streaming and the resting particles is laminar at the beginning close to the void and breaks up further downstream where turbulent mixing occurs.

6.3 Outlook

With the results of the analysis of the experiment it is possible to almost certainly rule out a Kelvin-Helmholtz type instability as a cause for the breakup. In fact the results can be fairly well explained by a Rayleigh-Taylor instability.

The observation of a Rayleigh-Taylor instability in a dusty plasma as described in our publication [5] has inspired other experimental work. For instance the group of Bob Merlino from the University of Iowa [80] has reported an experiment with this instability at the interface between large scale vortex flows in the microparticle cloud. Unfortunately the image quality in their experiment did not allow for single particle tracking so the analysis is based on the analysis of the brightness distribution from the whole particle cloud. This forestalls the description of the instability on the kinetic level.

The second difference to our experiment is the completely different plasma chamber. The experiment was conducted in a dc-discharge with an axial magnetic field. The discharge was formed by applying a 300 V bias to a 3.6 cm diameter anode disk with respect to the grounded walls of the cylindrical discharge chamber. The vacuum chamber had a diameter of 60 cm and a length of 100 cm. The axial magnetic field of 3 mT confined the electrons and produced an elongated anode glow in which the microparticle cloud was confined. The appearance of the same phenomenon in such different conditions emphasizes the universality of the observed instability.

Experimental investigations of shear flows and shear viscosity are also important as a test for simulations. For example the million-particle equilibrium molecular dynamics simulations performed by Budea et al. [81]. They determined the shear- viscosity in the 3-dimensional Yukawa liquid.

7 Publications

7.1 Physical Review Letters (PRL): Dissipative Dark Soliton in a Complex Plasma

Dissipative Dark Soliton in a Complex Plasma

R. Heidemann, S. Zhdanov, R. Sütterlin, H. M. Thomas, and G. E. Morfill

Max-Planck-Institut für extraterrestrische Physik, 85740 Garching, Germany

(Received 29 August 2008; published 31 March 2009)

The observation of a dark soliton in a three-dimensional complex plasma containing monodisperse microparticles is presented. We perform our experiments using neon gas in the bulk plasma of an rf discharge. A gas temperature gradient of 500K/m is applied to balance gravity and to levitate the particles in the bulk plasma. The wave is excited by a short voltage pulse on the electrodes of the radio frequency discharge chamber. It is found that the wave propagates with constant speed. The propagation time of the dark soliton is approximately 20 times longer than the damping time.

DOI: [10.1103/PhysRevLett.102.135002](https://doi.org/10.1103/PhysRevLett.102.135002)

PACS numbers: 52.27.Lw, 52.35.Mw, 52.35.Sb

We address the dynamics of nonlinear solitary waves which are impact excited in a dense complex plasma using a neon rf gas discharge at pressures 20–35 Pa. Complex plasmas are low pressure, low temperature plasmas containing microparticles. These microparticles are highly charged up by collecting plasma ions and electrons. They can be visualized individually with scattered light from a laser beam, which is recorded with a CCD camera.

The solitary wave structures we observe propagating in the complex plasma cloud are dominantly of a rarefactive type, hence resemble so called *dark solitons* (or *holes*, or *gray solitons* if mobile) important in a number of applications such as optical fibers, waveguides, laser beams, mechanics of discrete systems, etc. [1–4]. The physical mechanism determining the behavior of rarefactive solitary waves is still under debate [5]. Therefore, the search for physically realistic systems that can support stable solitary holes or dark solitons is of considerable interest [6]. Complex plasmas provide an excellent experimental system for such nonlinear structures.

There are two important points to be considered. First, nonlinear wave patterns observed in given experiments are highly dissipative. Therefore we will call them dissipative dark solitons (DDSs). Dissipativeness is ubiquitous, e.g., in granular media [7] which also can support solitary waves [8]. Second, DDSs are known to be weakly structurally unstable with a tendency to self-organize a shelf around the pulse wings [1]. In our case these are two asymmetric compressions that form the contour of the solitary wave. The backward one is a sedimentation front (similar to evaporation-condensation [9] or moisture wave fronts [10,11]). Here particle motion quickly damps and the cloud tends to restore its former quasiuniform structure. Note that the dissipative fronts are known as stabilizing factors for DDSs [6].

Travelling rarefactive structures are associated mostly with wave envelopes (as in examples with optic and waveguide applications cited above). Sound-like rarefactive waves are believed to be unstable. Nevertheless, a stable existence and propagation of compact rarefactive pulses is possible in multicomponent and nonisothermal plasmas,

i.e., in conditions quite similar to those of our experiments. For example, rarefactive ion acoustic solitary waves have been observed in auroral plasmas [12], and in multicomponent plasmas with negative ions [13]. Soliton formation both of potential hill and potential dip type have been predicted to exist in multicomponent self-gravitating molecular clouds consisting of, for example, a hydrogen gas and a dust component or a mixture of normal matter and dark matter [14,15]. Especially for dust acoustic waves the opportunity to observe the rarefactive pulses has been discussed in [16,17]. Parameters of these waves were predicted to be strongly dependent on anisotropy, nonisothermality and gas pressure. Recently it has been shown that rarefactive longitudinal solitons in complex plasmas can be described by the extended Korteweg–de Vries equation [18,19]. Dissipative solitons, existing in open systems, are considered a natural extension of the soliton concept in conservative systems. Compared to classical solitons, they may evolve (i.e., change their shape [20]) during propagation.

Compressive solitons in 2D complex plasmas were observed and studied in [21]. These waves were excited by an electric pulse to a wire located approximately in the plane of the particle monolayer. Large amplitude dust acoustic waves and compressive shock like excitations in a 3D complex plasma were studied in [22–24]. Excitation was achieved using gas-dynamic impacts, or an electromagnetic impulse [24]. The complex plasma was confined by the strong electric field of dc discharge striations, and the observations used image intensity profiles.

We use a modified version [25] of the PK-3 Plus design [26] currently installed on board the International Space Station. Discharge pressures (20–35 Pa) were chosen in the under critical domain to avoid autowave excitations [25]—at a pressure below 20 Pa. This allowed us to achieve a stable single-wave regime (Fig. 1) involving no complications caused by the interaction of solitary and self-excited waves. Above 35 Pa the wave was too strongly damped to be observable. The rf effective voltage was set to 13 V, a very low value, just high enough to sustain the discharge.

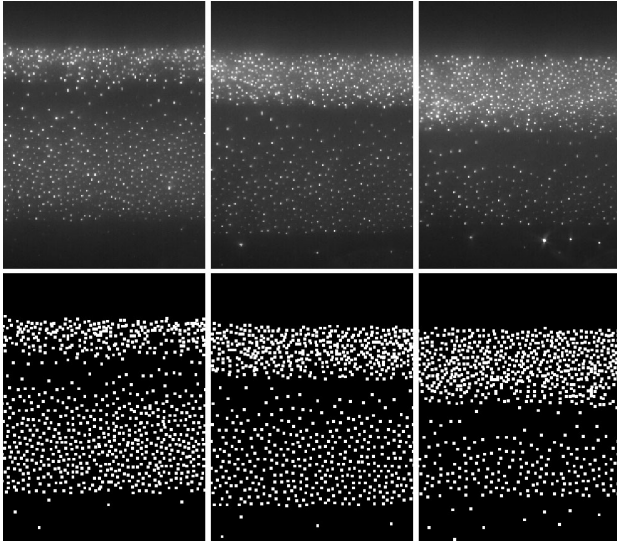


FIG. 1. Single-wave dynamics of the particle cloud. Upper row shows snapshots of the particle cloud. The cloud is illuminated by a laser beam extended to a sheet with the average thickness of $100 \mu\text{m}$. The field of view is $13.7 \times 7.2 \text{ mm}^2$. The brighter, growing stripe on the top of each image is the sedimented (nearly relaxed) part of the cloud. The bottom boundary of this stripe, expanding downwards, is the sedimentation front followed by the rarefaction zone (darker, almost particle free region below). From left to right: $t = 0.12 \text{ s}$, 0.20 s , 0.28 s after the instant of shock excitation ($t = 0 \text{ s}$). Neon gas pressure is 20.4 Pa . Tracked particle positions for the same time instants are shown in the lower row. Largely in-plane motion allows us to trace up to 95% of the particles in the field of view. Note that the rarefaction zone (*the dark soliton*) shifts rapidly downstream with respect to particle motion directed dominantly upwards [the maximal particle velocities (from left to right) are $1.8\text{--}2.0 \text{ cm/s}$].

Spherical monodisperse melamine-formaldehyde particles with a diameter of $3.42 \pm 0.06 \mu\text{m}$ were injected into a neon plasma. To situate the particle cloud in the bulk plasma, slightly below the center, we used thermophoresis to almost balance gravity. The lower chamber flange was heated to establish a temperature difference of $\Delta T = 15 \text{ K}$ across the whole chamber. This elevates the particles above the plasma sheath. It also forestalls the formation of a void that would appear if gravity is balanced completely [27].

An approximately $100 \mu\text{m}$ thick vertical slice through the center of the complex plasma was illuminated by a diode laser. The scattered light was recorded under 90° by a high-speed camera with a frame rate of 1000 Hz . The resolution is 1024×1024 pixels. The used optics allowed us to observe an area of $27.4 \times 27.4 \text{ mm}^2$ which resulted in a spatial resolution of $26.8 \mu\text{m}/\text{px}$.

This camera and optics in combination with newly developed software allowed us to track the full motion of 95% of all particles during the experiment. This was impossible in earlier experiments [21–25]. To generate the dark soliton, the complex plasma was first compressed by a dc offset of 8.6 V externally applied to electrodes.

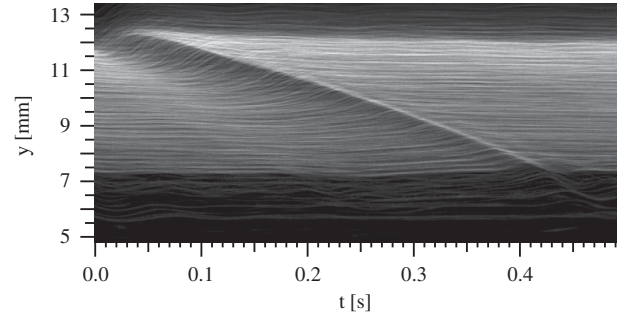


FIG. 2. Periodogram of the dark soliton in the complex plasma at 24.1 Pa . The wave is triggered by turning on or off a dc offset applied to both electrodes. The dark area corresponds to the rarefaction zone. The bright boundary on the right edge of the rarefaction zone is the narrow sedimentation front behind the wave. The periodogram is constructed from 490 still images (0.49 s). The vertical axis shows the distance from the lower electrode. The center of the plasma chamber is at 15 mm .

Switching off the dc offset triggers a solitary rarefaction wave. Particles are accelerated inside the wave, then decelerate forming a sedimentation front where the particles relax into a new equilibrium configuration (Fig. 1).

Figure 2 illustrates the propagation of the dark soliton through the particle system. In our recorded images the dark soliton propagates vertically (y direction), and the particle distribution in horizontal x direction is almost homogeneous (Fig. 1). The local particle density is proportional to the local visible brightness in the images. For each image the brightness is averaged in x direction resulting in a line showing the vertical brightness distribution. The periodogram is constructed by stacking these lines together, representing the temporal evolution of the vertical brightness distribution in the recorded images, and thus the density of the particle cloud. The dynamical scenario of the wave pattern formation is as follows: first, immediately after switching off the negative voltage offset, the particles are at rest; next, the top layer accelerates into the empty region above the particle cloud, quickly followed by the second and further layers. These fast moving particles constitute the rarefaction zone. They are stopped suddenly, forming a sedimentation front. At low pressures ($< 24 \text{ Pa}$) the fast particles can penetrate through the sedimentation front for up to five particle layers, resulting in a bidirectional flow. From tracked particle trajectories we calculate the particle number distribution $N_y(t)$ using a sliding window technique. The particles are counted in a window $1024 \times 8.5 \text{ pixel}^2$ centered around a given point y . This window is shifted in y direction in 2 pixel steps. As a reference for these particle number distributions we determined the distribution of particle numbers in the undisturbed cloud $\langle N_y \rangle_t$ at the same discharge conditions. The reference distribution is obtained by averaging over a time interval of 1 s (i.e., over 1000 frames). $N_y(t)$ and $\langle N_y \rangle_t$ are shown in Fig. 3(a).

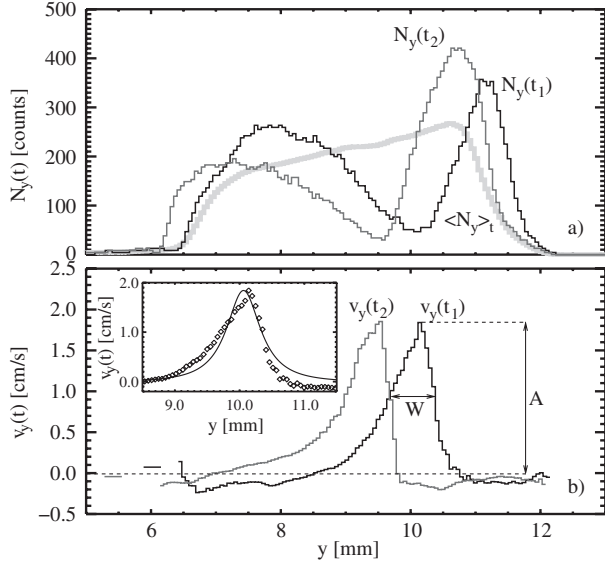


FIG. 3. (a) Particle number distributions $N_y(t)$ and (b) vertical particle velocity profiles $v_y(t)$ vs vertical position y , measured at 20.4 Pa and at $t_1 = 0.12$ s, $t_2 = 0.20$ s after the instant of excitation. The distribution of the undisturbed cloud $\langle N_y \rangle_t$ is drawn in grey. The mean interparticle separation is $\Delta \approx 90 \mu\text{m}$. The arrows indicate the amplitude (A) and the width at a half amplitude (W). Note that the minima of $N_y(t)$ correspond to the maxima of $v_y(t)$. (insert) The DDS velocity profile [5,34] matches well to the observed one (the fit accuracy is $\sigma = 1.9$ mm/s). The fit parameters were taken from the experiment at $t = t_1$.

The particle number distributions have three distinct large scale features: two maxima and one minimum. Close to the maxima the cloud is evidently denser compared to the reference distribution $\langle N_y \rangle_t$. These maxima are easy to identify: The first one (at lower y values) is the initial compression, which forms before the wave starts to propagate. The second one (at higher y values) corresponds to the sedimented part of the cloud, slowly relaxing into the new quasiequilibrium position. We identify the rarefaction zone between the maxima as the dark soliton. The rear edge of the dark soliton is steeper than the front edge.

To characterize the strength of the wave using these particle distribution functions, we determine the average maximum decompression ratio D . First we calculate the ratio $d(y, t) = \frac{\langle N_y \rangle_t}{N_y(t)}$, from which we select the maximum for each frame, and then average the result over the whole image sequence. With increasing pressure the decompression ratio decreases (Fig. 4). So the wave gets weaker with higher pressure, which is expected because of the higher neutral gas drag.

Averaged vertical particle velocity profiles $v_y(t)$ are shown in Fig. 3(b). Note that inside the wave the particles accelerate upwards, that is in the opposite direction compared to the soliton propagation direction. Using these

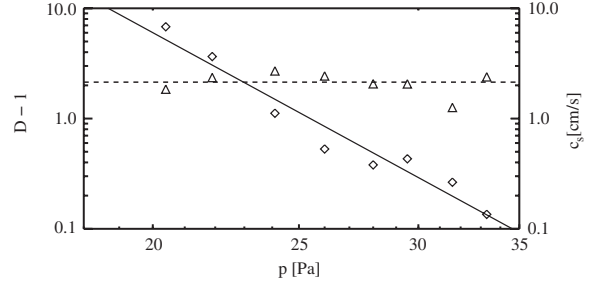


FIG. 4. (diamonds) Average maximum decompression ratio D and (triangles) the speed of sound c_s vs neon gas pressure. The solid line shows the power law least square fit: $D = \alpha(p[\text{Pa}]/20)^n + 1$, $\alpha = 6 \pm 1$, $n = -7.5 \pm 0.7$. The speed of sound was obtained by using the well-known relationship [5,34] $c_s = A \frac{\sqrt{D}}{D-1}$. The speed of sound depends weakly on pressure as the theory [17] predicts. On average, there is $\langle c_s \rangle = 2.14 \pm 0.16$ cm/s (the dashed line).

profiles we define three parameters of the wave (see Fig. 5): amplitude, speed, and width.

The shape of the dark soliton depends on the neutral gas pressure. The highest observed initial amplitude is $A_{\text{init}}(20.4 \text{ Pa}) = 4.50 \pm 0.03$ cm/s. In the range of 20–30 Pa the initial width of the wave is independent of pressure and has an average value of $\langle W_{\text{init}} \rangle = 0.69 \pm 0.05$ mm. The shape of the wave changes while it propagates through the cloud. For different neutral gas pressures the deformation dynamics varies. During the short

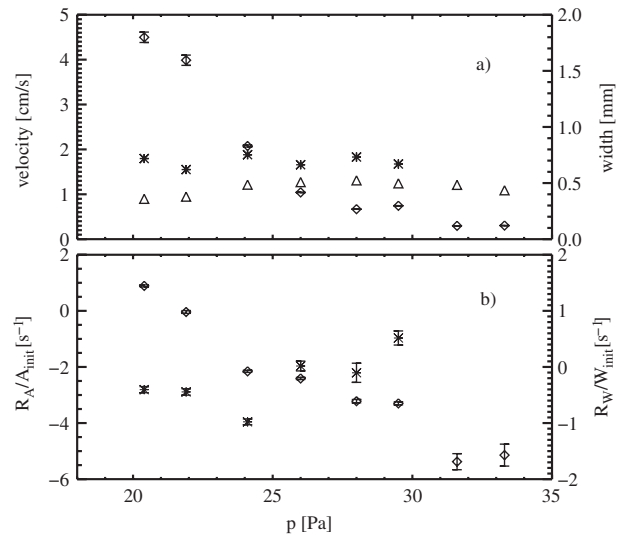


FIG. 5. (a) The dark soliton's amplitude A_{init} (diamonds), the width W_{init} (stars), and the wave speed v_{DS} vs pressure determined shortly after the instant of excitation. At pressures above 30 Pa the wave is too weak to determine its width properly. (b) The initial rate of the relative amplitude variation R_A/A_{init} (diamonds) and the relative width variation R_W/W_{init} (stars). Note that at $p < 22$ Pa the amplitude rate is positive, indicating a weak instability of the wave.

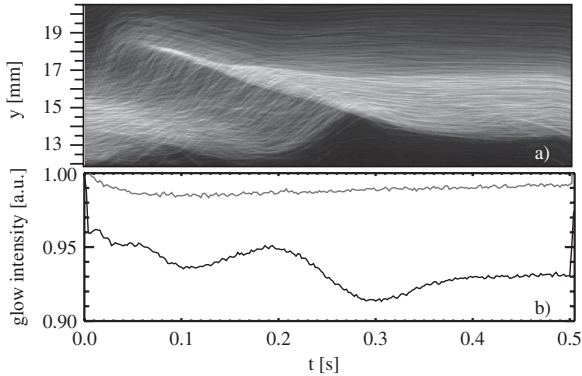


FIG. 6. (a) The particle number density profile and [(b), the black curve] the complex plasma glow intensity vs time. Apparently, the variation in the plasma glow follows the particle density variation. [(b), the gray curve] A control measurement in the particle-free plasma shows no such activity. The wave is triggered by turning on or off a dc offset applied to the bottom electrode.

time (~ 0.3 s) that we observe the propagating waves their amplitude and width vary approximately at a constant rate $R_A = \frac{dA}{dt} = \text{const}$, $R_W = \frac{dW}{dt} = \text{const}$, these constants are dependent on pressure. The relative variations R_A/A_{init} and R_W/W_{init} normalized by the initial values of the amplitude and the width, determined shortly after the instant of wave excitation, are shown in Fig. 5(b).

Surprisingly for $p < 22$ Pa the amplitude rate is positive, and the amplitude of the wave increases with time. The relative width variation is negative in this interval. Hence, the soliton's shape gets steeper. Since the complex plasma cloud is globally stable, this weak instability could be due to the nonlinear global modes [25,28]. Note also a well pronounced correlation of variations in the cloud density associated with DDS and in the plasma glow (Fig. 6). Note also that the enhanced discharge glow in the regions of the reduced particle number density favors the ionization instability [29,30].

At pressures above 22 Pa the soliton amplitude decreases rapidly during the propagation time, exactly as one would expect for waves propagating in any dissipative medium. However, the soliton amplitude decay rate is at least 10–25 times lower than the Epstein damping rate [31]. Such an anomalously low wave damping rate has also been found in plasma crystals previously [32,33]. It is thought to be due to a collective effect but an explanation is still outstanding.

To conclude, a rarefactive strongly nonlinear solitary wave has been excited in a dense complex plasma cloud compensated for gravity by thermophoresis. The rarefaction zone was observed traveling at a speed ~ 2 cm/s. We identify this wave as a *dissipative dark soliton* (with decompression factor as large as 7.8). We observed that the

DDS could self-support its propagation for as long as tens of dissipation times at least. The excitation and free propagation of this nonlinear dissipative structure can be observed because the complex plasma is in an active undercritical state for the pressure range used in the experiments.

This research was funded by DLR/BMWi Grant No. 50WP0203. Special thanks to Dr. Konopka and Peter Huber for continuous support in data analysis and programming, and Dr. Rothermel and Dr. Konopka for valuable help with planning and building the experiment.

- [1] S. Burtsev *et al.*, J. Opt. Soc. Am. B **14**, 1782 (1997).
- [2] Y. S. Kivshar, Phys. Rev. A **43**, 1677 (1991).
- [3] B. C. Collings *et al.*, Opt. Lett. **22**, 1098 (1997).
- [4] N. K. Efremidis *et al.*, Phys. Rev. E **66**, 046602 (2002).
- [5] A. Hasegawa *et al.*, *Optical Solitons in Fibers* (Springer-Verlag, Berlin, 2002).
- [6] N. Efremidis *et al.*, Phys. Rev. E **62**, 7410 (2000).
- [7] P. B. Umbanhowar *et al.*, Nature (London) **382**, 793 (1996).
- [8] A. Snezhko *et al.*, Phys. Rev. Lett. **94**, 108002 (2005).
- [9] O. Inomoto *et al.*, Phys. Rev. Lett. **85**, 310 (2000).
- [10] V. S. Shklyar *et al.*, J. Eng. Phys. Thermophys. **11**, 261 (1966).
- [11] J. Carmeliet *et al.*, J. Therm. Envelope Build. Sci. **27**, 277 (2004).
- [12] S. S. Ghosh *et al.*, Nonlinear Proc. Geophys **11**, 219 (2004).
- [13] Y. Nakamura *et al.*, Phys. Rev. Lett. **52**, 2356 (1984).
- [14] T. Cattaert *et al.*, Astron. Astrophys. **438**, 23 (2005).
- [15] R. E. Kates *et al.*, Astron. Astrophys. **206**, 9 (1988).
- [16] A. A. Mamun, Phys. Rev. E **55**, 1852 (1997).
- [17] P. K. Shukla *et al.*, *Introduction to Dusty Plasma Physics* (IOP, Bristol, 2002).
- [18] I. Kourakis, in *Multifacets of Dusty Plasmas: ICPDP5*, AIP Conf. Proc. No. 1041 (AIP, New York, 2008).
- [19] I. Kourakis *et al.*, Eur. Phys. J. D **29**, 247 (2004).
- [20] N. Akhmediev *et al.*, *Dissipative Solitons. Lect. Notes Phys.* (Springer, New York, 2005), Vol. 661.
- [21] D. Samsonov *et al.*, Phys. Rev. Lett. **88**, 095004 (2002).
- [22] V. E. Fortov *et al.*, Phys. Plasmas **10**, 1199 (2003).
- [23] V. E. Fortov *et al.*, Phys. Rev. E **69**, 016402 (2004).
- [24] V. E. Fortov *et al.*, Phys. Rev. E **71**, 036413 (2005).
- [25] M. Schwabe *et al.*, Phys. Rev. Lett. **99**, 095002 (2007).
- [26] H. M. Thomas *et al.*, New J. Phys. **10**, 033036 (2008).
- [27] H. Rothermel *et al.*, Phys. Rev. Lett. **89**, 175001 (2002).
- [28] A. Couairon *et al.*, Physica (Amsterdam) **108D**, 236 (1997).
- [29] N. D'Angelo, Phys. Plasmas **5**, 3155 (1998).
- [30] X. Wang *et al.*, Phys. Plasmas **8**, 5018 (2001).
- [31] P. S. Epstein, Phys. Rev. **23**, 710 (1924).
- [32] M. Rubin-Zuzic *et al.*, New J. Phys. **9**, 39 (2007).
- [33] M. Rubin-Zuzic *et al.*, Nature Phys. **2**, 181 (2006).
- [34] P. O. Fedichev *et al.*, Phys. Rev. A **60**, 3220 (1999).

**7.2 Europhysics Letters (EPL):Dissipative
dark solitons in a dc complex plasma**

Dissipative dark solitons in a dc complex plasma

This article has been downloaded from IOPscience. Please scroll down to see the full text article.

2010 EPL 89 25001

(<http://iopscience.iop.org/0295-5075/89/2/25001>)

View [the table of contents for this issue](#), or go to the [journal homepage](#) for more

Download details:

IP Address: 130.183.136.86

The article was downloaded on 17/09/2010 at 15:14

Please note that [terms and conditions apply](#).

Dissipative dark solitons in a dc complex plasma

S. ZHDANOV¹, R. HEIDEMANN¹, M. H. THOMA^{1(a)}, R. SÜTTERLIN¹, H. M. THOMAS¹, H. HÖFNER¹, K. TARANTIK¹, G. E. MORFILL¹, A. D. USACHEV², O. F. PETROV² and V. E. FORTOV²

¹ *Max-Planck-Institut für extraterrestrische Physik - 85741 Garching, Germany, EU*

² *Joint Institute for High Temperatures, Russian Academy of Sciences - 125412 Moscow, Russia*

received 10 September 2009; accepted in final form 23 December 2009

published online 2 February 2010

PACS 52.27.Lw – Dusty or complex plasmas; plasma crystals

PACS 52.35.Mw – Nonlinear phenomena: waves, wave propagation, and other interactions
(including parametric effects, mode coupling, ponderomotive effects, etc.)

PACS 52.35.Sb – Solitons; BGK modes

Abstract – The observation of dark solitons in a three-dimensional dc complex plasma is presented. The experiments are performed using neon gas at a pressure of 18 Pa and melamine-formaldehyde particles with a diameter of 3.43 μm . The waves are excited by a short pulse produced by the circular electrical-manipulative electrode built in inside the discharge glass tube. The wave speed is measured to be of the order of 15 mm/s. The propagation time of the observed dark soliton is approximately 10–15 times longer than the damping time.

Copyright © EPLA, 2010

Introduction. – Stable dark solitons (or *holes*) have a number of well-known applications in optics [1–3], laser beam dynamics [4], in mechanics of discrete systems [5] and many others [6]. These waves are also interesting from another point of view —as an indicator of the peculiar properties of dispersion and nonlinearity of the medium in which they propagate [1,6]. Recently rarefactive-type solitary waves, the dissipative dark solitons (DDS), have been observed and studied in a 3D complex plasma in an rf discharge [7]. (Complex plasmas are low-pressure, low-temperature plasmas containing microparticles. Due to their special properties, complex plasmas provide an excellent system to study fluid flow dynamics including solitons, multi-soliton excitations, self-excited wave ridges, on the most detailed scale, namely on the scale of individual particles. The microparticles are highly charged up by collecting plasma ions and electrons. They can be visualized individually with scattered light from a laser beam.) In plasma physics the term hole —*electron hole*, *ion hole*, *plasma hole*— is generally associated with particularities (a depression) in the particle distribution functions (see, e.g., [8–11]).

Traditionally an envelope of waves is called a dark soliton [1]. Nonetheless solitary rarefactive nonlinear waves are also interesting in many applications [12–15]. Recently, the opportunity to observe these waves in complex plasmas has been discussed theoretically [16–18].

Although the complex plasma used in these experiments was shown to be highly dissipative, the nonlinear wave patterns were not overdamped and clearly detectable. This, of course, is not very surprising —dissipation is ubiquitous, and in many cases even an inherent attribute of the self-supporting nonlinear structures [6,19].

At higher pressures it is normally a decay caused by friction. Still, the amplitude decay rate does not necessarily follow the decay law valid for individual particles [7].

In the present study we address the dynamics of nonlinear solitary waves which are impact-excited in a dense complex plasma using a neon dc gas discharge at a pressure of 18 Pa. The experiments were conducted using a parabolic-flight version of the PK-4 design [20–23] which is planned as a long-term research facility on the International Space Station. The experiments were performed during the 11th DLR Parabolic-Flight Campaign within 25 parabolas on Day 3 (November 2007) on board the A-300 ZERO-G plane. Experiments under microgravity have the advantage that the microparticle distribution becomes homogeneous enough for precision measurements.

The elongated form of the PK-4 discharge tube provides a unique experimental design for studying the propagation of different kinds of dust waves. Such waves can be either self-excited or initiated by an external source. In this work solitary waves were investigated using an excitation by an “electrical plunger” (electrical manipulative (EM) electrode) in a pulse mode. This way of excitation actually

^(a)E-mail: thoma@mpe.mpg.de

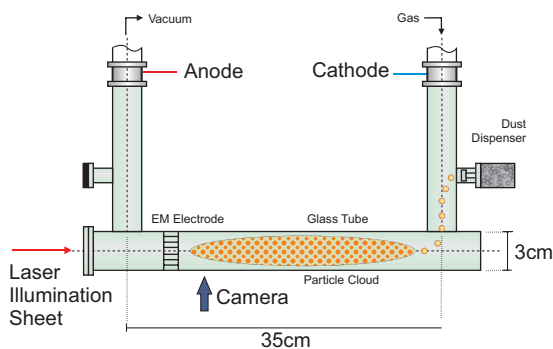


Fig. 1: (Color online) The heart of the PK-4 experimental setup. The main elements are: The “II”-shaped discharge chamber which is filled with neon. The cathode and the anode of the discharge are situated at the end of the “legs” of the tube. The particles are injected into the discharge plasma by dispensers localized at the cathode side (one of them is schematically shown). The recording system consists of an extended laser illumination sheet and a CCD camera. The particles injected from the dispenser stream towards the electrical plunger (EM electrode). They are then stopped by an effective confinement barrier caused by polarity switching at a frequency of 1 kHz, forming a dense particle cloud. The particle cloud can be stimulated by a series of short-time pulses provided by the plunger fed by the dc generator.

is similar to gas-dynamic impacts, or electromagnetic impulses used in [24,25] but in sharpness and localization of the impacts it has certain advantages compared to the latter.

Experimental procedure. – The experiments were conducted in the “Plasmakristall 4” (PK-4) experimental device that uses the positive column of a high-voltage dc discharge to produce complex (dusty) plasmas. A simplified sketch of the experiment geometry is drawn in fig. 1. The glass tube provides very good access for observation, diagnostics, and manipulation of the particles. The main part of the tube has a length of 35 cm and an inner diameter of 3 cm. Two optical ports offer access for laser illumination and manipulation, four particle dispensers allow the use of different microparticles (for the sake of simplicity in fig. 1 only one of them is shown). A gas supply system with adjustable gas flow ensures the purity of the gas (neon) and offers an additional way of introducing controllable flow to the complex plasma. Two CCD cameras record the microparticles.

Two dc cylindrical electrodes are installed at the ends of the tube. The dc discharge is operated with a regulated current of $I_{dc} = 1.0$ mA, corresponding to a voltage of about $U_{dc} = 1000$ V or less depending on the gas pressure. The plasma parameters, *i.e.*, electron temperature and density and the longitudinal electric field in the positive column of the dc discharge, have been determined by Langmuir probe measurements in ground-based laboratory experiments in the absence of particles. It was

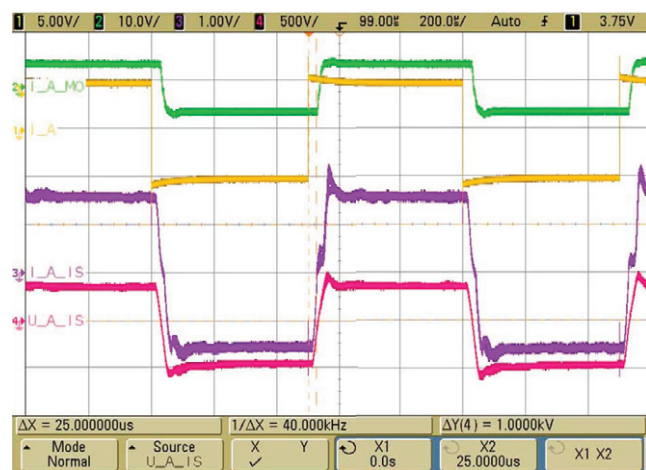
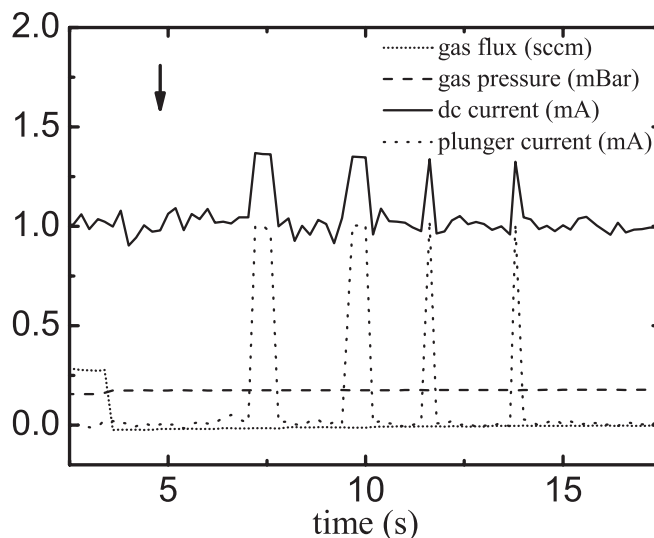


Fig. 2: (Color online) Top: a set of housekeeping data of the discharge in neon. After setting up the gas flux and the pressure, the dc discharge was ignited and the particles were injected into the tube. In order to “capture” the particle cloud, the discharge regime was changed to polarity switching at a frequency of 1 kHz. (In the plot this time instant is marked by the vertical arrow.) The short-time stimulation pulses are clearly identified as sharp peaks in the current of the electrical plunger (otherwise the current is set to zero). The pulse time durations were varied to choose the optimal regime. From left to right: $\frac{1}{2}$ s, $\frac{1}{3}$ s, $\frac{1}{6}$ s, $\frac{1}{12}$ s. Shorter pulses gave more reproducible results (see fig. 3). Bottom: a typical oscillogram of a polarity switching regime (neon, pressure 100 Pa, 0.2 sccm gas flow) with a 1.6 mA discharge current. Four signals are measured (in volts) and displayed on the oscilloscope screen shots: yellow: the high-voltage (HV) current control signal and green: the housekeeping current parameter, measured internally and returned by the HV-source (the conversion coefficients are 0.32 mA/V in both cases); magenta: the voltage drop at the 1 kOhm series resistor, a measure for the real plasma discharge current (the conversion coefficient is 1.0 mA/V); red: the discharge voltage across the plasma discharge tube. The discharge voltage changes with fairly steep transitions (≈ 40 μ s) between +450 V and -450 V. The discharge current alternates between plus and minus 1.6 mA more or less ideally.

found that the longitudinal electrical field is given by $E \simeq 2 \text{ V/cm}$ independent of the pressure (between 15 and 150 Pa) at a dc current of 1.0 mA [22].

The experimental facility can be operated in a pure dc as well as in a low-frequency discharge regime by applying polarity switching at a frequency of 0.1–5 kHz and at a variable duty cycle (see fig. 2). The polarity switching is a well-suited method for controlling the net averaged longitudinal electrical field in the positive column of a plasma discharge. At typical polarity switching frequencies of 1 kHz, microparticles act on this averaged field only and can therefore easily be manipulated. This leads to an effective “potential well” sufficiently deep to trap the particles and to create a stable and extended particle cloud with a fixed position within the plasma chamber in case of a vanishing net field.

Experimental conditions. – In the present work DDS were investigated under microgravity applying an excitation by the electrical plunger operated in a pulse regime. A controlled gas pressure was chosen at a level of 18 Pa and a flow rate of 0.3 sccm (see fig. 2). Monodisperse melamine formaldehyde particles with a diameter of $3.43 \pm 2\% \mu\text{m}$ and a mass $m = 3.2 \cdot 10^{-11} \text{ g}$ were injected into the dc discharge plasma in the vicinity of the cathode. After injection the particles first rapidly drifted in the direction of the anode (driven by the dc electric field of the discharge and by the gas flow). The speed of the particles 80–90 mm/s observed at this stage is limited by the gas friction. The gas damping rate is estimated to be $\gamma_{Eps} = 41 \text{ s}^{-1}$ [26]. Shortly before the streaming particles reached the plunger, the gas flow was stopped and the discharge was changed to the polarity switching regime at a frequency of 1 kHz (50% duty cycle). This frequency is more than an order of magnitude higher than the dust-plasma (response) frequency, so that the effective longitudinal force on the microparticles (electric plus ion drag) averages to zero leading to a trapping of the particles (fig. 3).

A short-duration pulse is applied to the electrical plunger and disturbs the particle cloud. This is a rather convenient method to trigger and study propagating density waves: By changing the polarity of the applied pulse it is possible to obtain a rarefactive wave (which we study here) or a compression (shock) wave, either. Details on the shock excitations will be published elsewhere.

The particle cloud was illuminated by a laser sheet (wavelength: 686 nm, output power: 20 mW) of 100 μm FWHM and recorded by a CCD camera (JAI Progressive Scan) at a frame rate of 60 fps with an image resolution of $640 \times 480 \text{ px}^2$ and an image exposure time 8 ms per frame. The camera field of view (FoV) was $21 \times 16 \text{ mm}^2$ at the tube axis. The spatial resolution of the video recording system was about 33 $\mu\text{m}/\text{px}$. On average over 2650 particles (± 120) were tracked in each frame and traced from one frame to another to calculate the particle velocity.

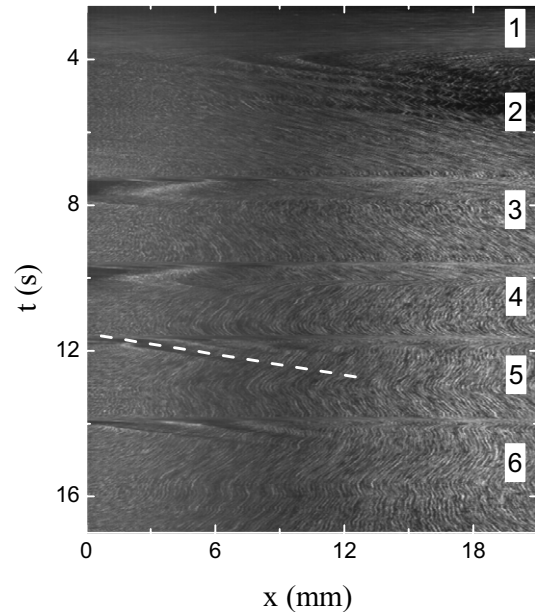


Fig. 3: Periodogram (a (x, t) map) of the complex-plasma dynamics taken over about 14 s of the experiment. The numbers mark the main observed stages: (1) a freely streaming particle flow, (2) a first relaxation stage, (3–6) stages of the propagating waves alternated by intermediate relaxation stages. The waves are triggered by turning on/off a dc current feeding the “electrical plunger” (see text); the push-pull sequences are seen as the elongated brighter horizontal stripes passing across the map. The inclined darker and shorter stripes correspond to the rarefaction zones (the dark solitons). The dashed reference line indicates the propagation velocity of 12 mm/s. The soliton propagation velocities exhibit a slight scatter from one initiation to another, and even inside the same single multi-wave mode. On average the slope of the darker regions yields $V_{DDS} = 12 \pm 0.5 \text{ mm/s}$ for all stages with excitations (2–6). The maximum observed velocity of the particles, accelerating inside the DDS, is of the same order. At the stage (1) the velocity of the streaming particles is much higher (80–90 mm/s). The darkest regions to the left are particle free. The DDS are formed later on inside the relaxing cloud.

During the experiments the injected particles formed an elongated quasi-uniform cloud with a diameter of $\sim 0.9 \text{ cm}$ and a mean particle density of $\langle n_d \rangle = (6\text{--}8) \cdot 10^4 \text{ cm}^{-3}$. The electron density n_e and the electron temperature T_e were diagnosed by a Langmuir probe in laboratory investigations [22,23]: $n_e = (1\text{--}2) \cdot 10^8 \text{ cm}^{-3}$ and $T_e = 5\text{--}7 \text{ eV}$ for the dc mode. There are some indications that the low-frequency polarity switching does not significantly change the plasma conditions [27,28].

Assuming no complications due to a possible interaction of solitary and self-excited waves, the discharge pressure was chosen to lie in-between the unstable and the overdamped regime. This forestalls the formation of self-excited waves [29] and ensures that solitary waves are not overdamped and therefore barely detectable. Examples with a few stable wave ridges obtained at 18 Pa are shown in figs. 3 and 4.

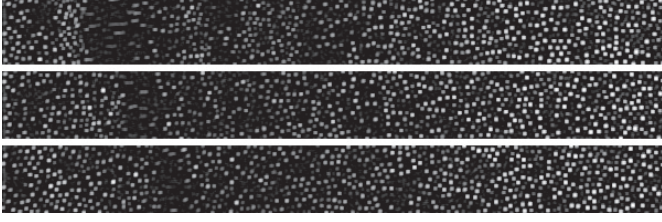


Fig. 4: Three consecutive snapshots of the particle cloud, demonstrating the wave dynamics. The neon gas pressure is 18 Pa. The cloud is illuminated by a laser beam extended to a sheet with average thickness of $100\ \mu\text{m}$. The field of view is $2 \times 21\ \text{mm}^2$. The brighter, growing stripe on the left of each image is the initial relaxed part of the cloud. It is followed by the rarefaction zone, nearly free of particles. The maximal particle speed observed there was 11–12 mm/s. Also two more much weaker rarefactive zones can be seen to the right of the first one. The particles then relax back to the original state (right). From top to bottom: $\Delta t = 0.27\ \text{s}, 0.37\ \text{s}, 0.47\ \text{s}$ after the instant of excitation. The images were noise-filtered and gamma-corrected to enhance the contrast.

Following [30] and using the parameters listed above, we estimate the particle charge to be in the range of $Z \simeq 5000\text{--}7000\ e$.

Results and discussion. – Figure 3 shows the periodogram that illustrates the propagation of the dark solitons through the particle system. The periodogram is assembled in the following way: first, a narrow horizontal band of $2 \times 21\ \text{mm}^2$ is isolated from the center of each frame, next, all pixel intensities are added vertically resulting in a single line showing the central horizontal pixel intensity distribution. These lines are finally stacked in sequence, representing the temporal evolution of the horizontal brightness distribution in the recorded images, and thus (to some extent) the density of the particle cloud.

The dynamical scenario of the individual wave pattern formation is clearly seen in fig. 4: the particles are accelerated inside the wave, constituting the rarefaction zone, then decelerated forming a compression front where they relax into a new equilibrium configuration. This behavior is similar to that observed in rf complex plasmas [7].

Figure 5 shows the detailed dynamical pattern as indicated by the pixel intensities and the particle velocity distributions. The shape of the wave changes significantly as it propagates through the cloud. Actually there is a one-soliton regime at the time $\Delta t = 0.72\ \text{s}$ after the ignition. The shape of the wave becomes modified mainly because of neutral gas damping. At this particular moment the soliton amplitude is approximately $|V_1| = 1.1\ \text{mm/s}$ compared to $|V_2| \sim 9\text{--}12\ \text{mm/s}$ immediately after the trigger. The soliton amplitude damping rate can be estimated then roughly as

$$\gamma_{damp} = (\Delta t)^{-1} \ln(|V_2/V_1|) \approx 3\ \text{s}^{-1}. \quad (1)$$

The rough estimate (1) of the soliton damping rate agrees well with that obtained from the asymptotics of the DDS (see the insert in fig. 5).

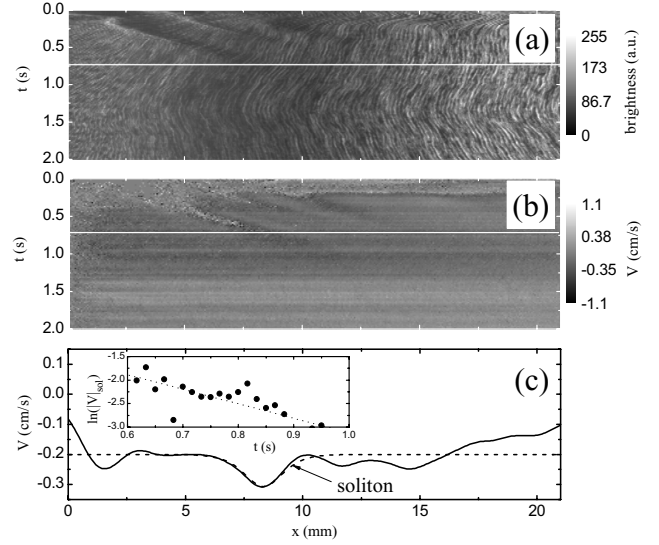


Fig. 5: (a) The image intensity distribution (stage 5 in fig. 3), (b) the map of the binned horizontal particle velocities and (c) the velocity profile of the solitary wave and the accompanying residual particle drift taken at the moment indicated in (a) and (b) with the white horizontal line ($\Delta t = 0.72\ \text{s}$ after the pulse). The velocity profile is smoothed with a Gaussian kernel of bandwidth $0.65\ \text{mm}$. The mean interparticle separation is $\langle \Delta \rangle \approx 300 \pm 10\ \mu\text{m}$. The actual wave shape of DDS fits well with a “classical” inverse-squared-hyperbolic cosine form (the dashed line in (c), see the text for details). The insert: with time the soliton gets weaker with the decay rate $3.1 \pm 0.6\ \text{s}^{-1}$ as indicated by the dotted line. The soliton amplitude $|V|_{sol}$ is measured in cm/s.

It is approximately

$$\frac{\gamma_{Eps}}{\gamma_{damp}} \approx 14 \quad (2)$$

times less than that predicted by the Epstein formula [26]. Hence, as in [7], soliton damping is *anomalously* low. This is thought to be due to a collective effect [7,31,32] but a full explanation is still outstanding.

Note that the observed damping rate is stronger than that reported in [7], in spite of the same particle size.

The wave structure (the particle velocity profile) fits well with the “classical” soliton shape

$$V = V_{drift} - |V|_{sol} \cosh^{-2} \left(\frac{x - x_0}{\delta L} \right). \quad (3)$$

Taking the parameters $V_{drift} = -2\ \text{mm/s}$, $|V|_{sol} = 1.1\ \text{mm/s}$, $x_0 = 8.32\ \text{mm}$, and $\delta L = 1.1\ \text{mm}$, we obtained the wave shape shown in fig. 5. Good agreement is evident. The soliton width is estimated to be a few ion screening lengths, $\delta L/\lambda_{di} \sim 5\text{--}7$. The weak asymmetry of the wave is due to the spatial inhomogeneity of the cloud.

The main results of the present study agree fairly well in many respects with those obtained in [7]. Indeed this is a very surprising fact. These two series of experiments (a rf-discharge plasma compared to a low-frequency

discharge plasma) were different not only with respect to the discharge conditions, and hence the global particle confinement, but also the particle dynamics conditions were different. The particle cloud was lifted by thermophoresis in ground-based experiments [7] whereas in the recent study the cloud showed a freely relaxing after-shock in microgravity conditions. Moreover, in the given experiments it was possible to study the DDS at lower pressures (18 Pa) for which the waves are unstable in rf-plasmas [7].

Another interesting peculiarity of the present experiments is the particle drift affected by the relaxation process. For instance, $|V_{drift}| = |\langle V \rangle| \approx 2\text{--}2.5$ mm/s at the particular moment specified in fig. 5. On average the DDS speed is as large as $V_{DDS} = 12\text{--}12.5$ mm/s. Hence, the absolute wave speed can be estimated as

$$C_{DDS} = V_{DDS} + |V_{drift}| \approx 15 \pm 1 \text{ mm/s}. \quad (4)$$

in fairly good agreement with that measured in [7]. As in [7], the wave speed is less than the speed of the dust acoustic waves. For our set of parameters the theory [17] predicts $C_{DAW}^{(theory)} \simeq 20\text{--}25$ mm/s.

Note that the individual particle dynamics is indeed overdamped. To verify that this is true let us compare the frictional kinetic energy dissipation rate

$$\dot{W}_{fr} = m\gamma_{Eps} \langle V^2 \rangle \approx \frac{1}{2} m\gamma_{Eps} V_{max}^2, \quad (5)$$

where V_{max} is the maximal absolute particle velocity inside the wave, to the rate of change of the kinetic energy defined as

$$\dot{W}_{kin} = \frac{1}{2} m \frac{V_{max}^2}{\delta t} \approx m \frac{V_{max}^3}{\delta L}, \quad (6)$$

where δL is the soliton front width. For the case chosen in fig. 5 the ratio of the rates is

$$\frac{\dot{W}_{fr}}{\dot{W}_{kin}} = \frac{\gamma_{Eps} \delta L}{2V_{max}} \sim 10 \gg 1. \quad (7)$$

Apparently, the frictional losses are dominating in the balance. Under the given conditions it seems quite reasonable to assume that the main components of the in-wave balance are friction and the electrical force. (In this way the particle tracks themselves are treated as a probe of the interior of the DDS which otherwise is difficult to study.) Based on the balance condition $m\gamma_{Eps}V = ZeE_s$ and making use of the relationship (3) it is possible to restore the inherent structure of the DDS electrical field $E_s = E_s(x, t)$, and hence the mutual polarization. It immediately follows (to leading order) that in this sense the DDS is a double-layer-like structure with negative charge ahead, accelerating the particles downwards. (A double layer in a plasma is a structure consisting of two parallel layers with opposite electrical charge.)

Another interesting issue found from the analysis is the drift of the particle cloud accompanying the after-shock relaxation (see fig. 6). Quite recognizable are at least

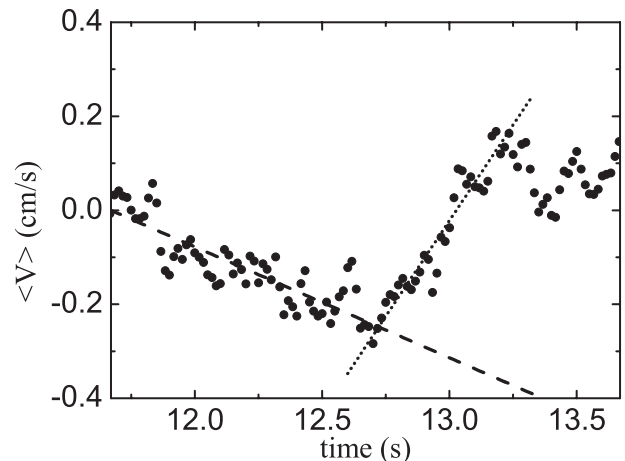


Fig. 6: Drift of the cloud. There are at least three well-recognizable main stages of the drift dynamics: an acceleration, a deceleration, and finally rather weak relaxation oscillations. The dashed and the dotted lines show the rms linear fits to the first two stages with $a_1 = -2.4 \pm 0.2$ mm/s² and $a_2 = 8.1 \pm 0.5$ mm/s².

three main phases of the drift: active acceleration, even more active deceleration, and relaxation oscillations of the cloud. During the acceleration-deceleration stages the drift velocity profile is surprisingly simple: The velocity varies approximately at a constant rate. By analogy with [33] this allows us to explore more closely the structure of the forces, confining the particles. Starting from the balance equation:

$$m\gamma_{Eps} \langle \dot{V} \rangle = Ze \dot{E}_{conf} = Ze E'_{conf} \langle V \rangle, \quad (8)$$

where $\langle V \rangle$ is the particle drift velocity, E_{conf} is the local strength of the electric field (it is assumed that $E'_{conf} \approx \text{const}$), Ze is the particle charge, and defining the confinement frequency parameter Ω_c as

$$\left| \frac{Ze E'_{conf}}{m} \right| \equiv \Omega_c^2, \quad (9)$$

we arrive finally at the relationship

$$\Omega_c^2 = \gamma_{Eps} \left| \frac{\langle \dot{V} \rangle}{\langle V \rangle} \right|. \quad (10)$$

This relationship allows the estimate of typical values of the confinement parameter. Assuming that $\langle V \rangle = 2$ mm/s (see fig. 5), for the data set shown in fig. 6 it follows that $\Omega_c^{(acc)} \approx 7$ s⁻¹ at the acceleration stage, whereas $\Omega_c^{(dec)} \approx 13$ s⁻¹ is approximately twice as high during the deceleration stage. This enables the rough reconstruction of the confinement forces.

Conclusion. – The message we want to communicate in this letter is rather simple: A dc strongly coupled complex plasma provides a promising tool to study dissipative nonlinear structures—in particular the dissipative dark solitons—at the kinetic level. For the first time

we have observed recognizable DDS in a dc complex-plasma cloud and characterized them. We found that under our experimental conditions the DDS traveled at a speed of about 15 mm/s. We observed that the DDS could self-supports its propagation for much longer times than dissipation would imply. The reason for this “anomalous behavior” is not clear yet.

We explored the after-shock relaxation patterns and demonstrated that this could be a promising way to reconstruct the particle confinement parameters.

The observed results represent a first step towards understanding the fascinating property of dc complex plasmas with respect to self-sustained regular dissipative solitary dynamical patterns.

The PK-4 project is supported by ESA and DLR under grant no. 50WM 0804. Also we thank DLR for giving us the opportunity to participate in a parabolic-flight campaign. The Joint Institute for High Temperatures is supported by the Russian Foundation for Basic Research under grant No. 07-02-01464. Furthermore, we would like to thank V. NOSENKO for valuable discussions and C. DEYSENROTH, C. RAU, and S. ALBRECHT for excellent technical support.

REFERENCES

- [1] HASEGAWA A. and MATSUMOTO M., *Optical Solitons in Fibers* (Springer-Verlag) 2002.
- [2] BURTSEV S. and CAMASSA R., *J. Opt. Soc. Am. B*, **14** (1997) 1782.
- [3] KIVSHAR Y. S., *Phys. Rev. A*, **43** (1991) 1677.
- [4] COLLINGS B. C., BERGMAN K. and KNOX W. H., *Opt. Lett.*, **22** (1997) 1098.
- [5] EFREMIDIS N. K., SEARS S., CHRISTODOULIDES D. N., FLEISCHER J. W. and SEGEV M., *Phys. Rev. E*, **66** (2002) 046602.
- [6] AKHMEDIEV N. and ANKIEWICZ A. (Editors), *Dissipative Solitons*, in *Lect. Notes Phys.*, Vol. **661** (Springer) 2005.
- [7] HEIDEMANN R., ZHDANOV S., SÜTTERLIN R., THOMAS H. M. and MORFILL G., *Phys. Rev. Lett.*, **102** (2009) 135002.
- [8] SAEKI K. and RASMUSSEN J. J., *J. Phys. Soc. Jpn.*, **60** (1991) 735.
- [9] DRAKE J. F., SWISDAK M., CATTELL C., SHAY M. A., ROGERS B. N. and ZEILER A., *Science*, **299** (2003) 873.
- [10] JOVANOVIĆ D., SHUKLA P. K. and MORFILL G., *J. Plasma Phys.*, **71** (2005) 203.
- [11] YOSHIMURA S., OKAMOTO A. and TANAKA M. Y., *J. Plasma Fusion Res.*, **8** (2009) 11.
- [12] GHOSH S. S. and LAKHINA G. S., *Nonlinear Process. Geophys.*, **11** (2004) 219.
- [13] NAKAMURA Y. and TSUKABAYASHI I., *Phys. Rev. Lett.*, **52** (1984) 2356.
- [14] CATTART T. and VERHEEST F., *Astron. Astrophys.*, **438** (2005) 23.
- [15] KATES R. E. and KAUP D. J., *Astron. Astrophys.*, **206** (1988) 9.
- [16] MAMUN A. A., *Phys. Rev. E*, **55** (1997) 1852.
- [17] SHUKLA P. K. and MAMUN A. A., *Introduction to Dusty Plasma Physics* (IOP, Bristol) 2002.
- [18] KOURAKIS I. and SHUKLA P. K., *Eur. Phys. J. D*, **29** (2004) 247.
- [19] UMBANHOWAR P. B., MELO F. and SWINNEY H. L., *Nature*, **382** (1996) 793.
- [20] MITIĆ S., SÜTTERLIN R., IVLEV A. V., HÖFNER H., THOMA M. H., ZHDANOV S. and MORFILL G. E., *Phys. Rev. Lett.*, **101** (2008) 235001.
- [21] USACHEV A. D., ZOBININ A. V., PETROV O. F., FORTOV V. E., ANNARATONE B. M., THOMA M. H., HÖFNER H., KRETSCHMER M., FINK M. and MORFILL G. E., *Phys. Rev. Lett.*, **102** (2009) 045001.
- [22] USACHEV A., ZOBININ A., PETROV O., FORTOV V., THOMA M., KRETSCHMER M., RATYNSKAIA S., QUINN R., HOEFNER H. and MORFILL G. E., *Czech. J. Phys.*, **54** (2004) C639.
- [23] FORTOV V., MORFILL G., PETROV O., THOMA M., USACHEV A., HOEFNER H., ZOBININ A., KRETSCHMER M., RATYNSKAIA S., FINK M., TARANTIK K., GERASIMOV YU. and ESEKOV V., *Comments Plasma Phys. Controlled Fusion*, **47** (2005) B537.
- [24] FORTOV V. E., PETROV O. F., MOLOTKOV V. I., POUSTYLNİK M. Y., TORCHINSKY V. M., KHRAPAK A. G. and CHERNYSHEV A. V., *Phys. Rev. E*, **69** (2004) 016402.
- [25] FORTOV V. E., PETROV O. F., MOLOTKOV V. I., POUSTYLNİK M. Y., TORCHINSKY V. M., NAUMKIN V. N. and KHRAPAK A. G., *Phys. Rev. E*, **71** (2005) 036413.
- [26] EPSTEIN P. S., *Phys. Rev.*, **23** (1924) 710.
- [27] CHANDRAKAR K., *Br. J. Appl. Phys.*, **16** (1965) 449.
- [28] BHIDAY M. R., GHOLAR A. V. and PHADKE K. W., *Int. J. Electron.*, **3** (1968) 249.
- [29] SCHWABE M., RUBIN-ZUZIC M., ZHDANOV S., THOMAS H. M. and MORFILL G., *Phys. Rev. Lett.*, **99** (2007) 095002.
- [30] MORFILL G. E., KONOPKA U., KRETSCHMER M., RUBIN-ZUZIC M., THOMAS H. M., ZHDANOV S. K. and TSYTOVICH V., *New J. Phys.*, **8** (2006) 7.
- [31] RUBIN-ZUZIC M., THOMAS H. M., ZHDANOV S. K. and MORFILL G. E., *New J. Phys.*, **9** (2007) 39.
- [32] RUBIN-ZUZIC M., MORFILL G. E., IVLEV A. V., POMPL R., KLUMOV B. A., BUNK W., THOMAS H. M., ROTHERMEL H., HAVNES O. and FOUQUÈT A., *Nat. Phys.*, **2** (2006) 181.
- [33] KRETSCHMER M., KHRAPAK S. A., ZHDANOV S. K., THOMAS H. M., MORFILL G. E., FORTOV V. E., LIPAEV A. M., MOLOTKOV V. I., IVANOV A. I. and TURIN M. V., *Phys. Rev. E*, **71** (2005) 056401.

7.3 Physics of Plasmas (PoP): Comprehensive experimental study of heartbeat oscillations observed under microgravity conditions in the PK-3 Plus laboratory on board the International Space Station

Comprehensive experimental study of heartbeat oscillations observed under microgravity conditions in the PK-3 Plus laboratory on board the International Space Station

Ralf J. Heidemann^{1,a)} Lénaïc Couédel,¹ Sergey K. Zhdanov,¹ K. Robert Sütterlin,¹ Mierk Schwabe,¹ Hubertus M. Thomas,¹ Alexey V. Ivlev,¹ Tanja Hagl,¹ Gregor E. Morfill,¹ Vladimir E. Fortov,² Vladimir I. Molotkov,² Oleg F. Petrov,² Andrey I. Lipaev,² Valery Tokarev,³ Thomas Reiter,⁴ and Pavel Vinogradov⁵

¹Max-Planck-Institut für extraterrestrische Physik, Giessenbachstraße, 85741 Garching, Germany

²RAS-Joint Institute for High Temperatures, Izhorskaya 13/19, 127412 Moscow, Russia

³Yu.Gagarin Cosmonaut Training Center, 141160 Star City, Moscow Region, Russia

⁴Deutsches Zentrum für Luft- und Raumfahrt e.V., Linder Höhe, 51147 Köln, Germany

⁵Rocket Space Corporation "Energia," 141070 Korolev, Moscow Region, Russia

(Received 12 November 2010; accepted 15 March 2011; published online 16 May 2011)

Heartbeat oscillations in complex plasmas with a broad range of fundamental frequencies are observed and studied. The experiments are performed with monodisperse microparticles of different diameters in argon as well as in neon plasmas. The oscillation frequency increases with increasing rf power and neutral gas pressure. At the lower frequencies, oscillations are strongly nonlinear. The microparticle pulsations, the variation of the electrical discharge parameters and the spatially resolved changes in the plasma glow are proven to be strongly correlated. Heartbeat oscillation dynamics is associated with global confinement modes. © 2011 American Institute of Physics. [doi:10.1063/1.3574905]

I. INTRODUCTION

In this article, a comprehensive experimental study of the heartbeat oscillations observed in a complex (dusty) plasma is reported. This study has been performed over 8 months in the PK-3 Plus laboratory on board the International Space Station (ISS).¹ PK-3 Plus uses a capacitively coupled radio frequency (rf) plasma chamber. The microparticle component of the complex plasma consists of monodisperse plastic beads a few micrometers in diameter. These particles are injected into a low temperature noble gas plasma. Every particle acts as a sink for the electrons and ions surrounding it. Due to higher electron mobility, the particles acquire a negative net charge roughly proportional to their diameter. The resulting surface potential is shielded by the positive space charge of the plasma ions.

The negatively charged particles repel each other. Being trapped in the plasma potential well, they self-arrange themselves under microgravity conditions to homogeneous three-dimensional clouds, albeit commonly containing a void—a region free of microparticles—in the center.² Several mechanisms have been proposed explaining the existence of the void, e.g., Goree *et al.*³ suggested: “In the presence of electron-impact ionization, a positive space potential develops, creating an outward ambipolar electric field that drives ions outward, applying an outward ion drag force, which can maintain a void.” First experimental evidence of the void and for void dynamics was published by Morfill *et al.*² and Samsonov and Goree.⁴ A few theoretical models explaining the formation and stability of the void were proposed, among

them Tsytovich,⁵ Tsytovich *et al.*,^{6–8} Avinash *et al.*,⁹ and Vladimirov *et al.*¹⁰ First numerical studies on void formation have been conducted by Akdim and Goedheer¹¹ and Tribecche *et al.*¹² The stability of the void itself is frequently explained by the counteraction of a confinement force and the ion drag force. Conclusive experimental, numerical, and theoretical investigations were done by Kretschmer *et al.*¹³ We suggest that the confinement force is caused by the ambipolar field.

Complex plasma is a state of soft matter comprised of a dense microparticle cloud embedded in a plasma. The higher the density of the microparticle cloud, the more likely it is to observe instabilities that are unique to complex plasmas. As the microparticle cloud becomes denser, the microparticle interactions become stronger and particle motions are strongly correlated to each other and to the local and global plasma parameters. Experimentally observed auto-oscillations and instabilities can be regular¹⁴ as well as irregular with a wide spectrum of excitations.^{4,15–18} One of these phenomena is the so called “heartbeat”: Under certain conditions, the complex plasma configuration becomes unstable and the microparticle cloud starts to pulsate.³ We divide this heartbeat phenomenon into two stages. Starting from a stable plasma and particle configuration, an instability occurs and the system switches into a stable auto-oscillation mode. We shall call the transition phase *heartbeat instability* and the following stable oscillation phase *heartbeat oscillation*. In general, the heartbeat instability and the heartbeat oscillation must be treated as a collective phenomenon of the complex plasma,¹⁹ i.e., taking into account all constituents and their interactions. It cannot be explained as a collective (wave-like) motion of strongly coupled microparticles alone. Our

^{a)}Electronic mail: heidemann@mpe.mpg.de.

experiments can resolve the microparticle dynamics and the rearrangement of the plasma glow. A complete theoretical explanation of this phenomenon is still missing.

The article is organized as follows. In Sec. II, we describe the experimental setup and define the parameter range for our experiments. In Sec. III, we report the general conditions in the complex plasma cloud and give estimates for complex plasma parameters that cannot be measured directly. The dynamical features of the complex plasma auto-oscillations are determined in Sec IV, and the heartbeat phenomenon is described in detail. The changes in the plasma glow are shown, and they are associated with changes in ionization. The microparticle kinetics and dynamics are correlated with electrical measurements. The dust-plasma frequency and the frequency of the heartbeat mode are calculated for our parameters and compared to the heartbeat oscillation frequency. In Sec. V, the heartbeat instability, which is the transition from a stable cloud to a stably oscillating cloud, is discussed. We also discuss limits to the parameter space where the heartbeat instability occurs. In Sec. VI, the obtained results are summarized and the main conclusion is presented.

II. EXPERIMENTAL PROCEDURES AND MEASUREMENTS

A. Experimental setup

The PK-3 Plus setup (see Fig. 1) has been constructed to perform experiments with complex plasmas under microgravity conditions. The plasma is produced by an rf generator of 4 W maximum at 13.56 MHz, which is capacitively coupled to the electrodes via an RC-matching box. The electrodes are mounted in parallel plate configuration and are driven in push-pull mode. They have a diameter of 6 cm and are 3 cm apart. Each electrode is surrounded by a grounded ring of 1.5 cm width. Due to a directional coupler in the rf generator, we feed the chamber with constant power. It is possible to use either argon or neon as working gas, under controlled pressure between 8 and 255 Pa. The pressure is measured by a Baratron with an accuracy of $\pm 0.5\%$. Mono-

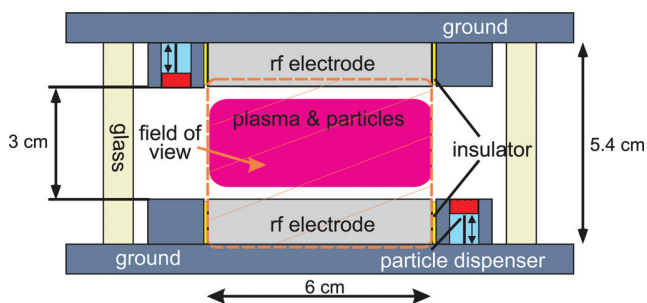


FIG. 1. (Color online) Sketch of the PK-3 Plus setup (Ref. 1). The powered aluminum electrodes are symmetrically driven by an rf power generator in push-pull mode. They are surrounded by grounded guard rings mounted on the grounded aluminum plate flanges. An insulator ring of high thermal conductivity (alumina) prevents a temperature gradient between the electrodes and the grounded structure. Three electromagnetically driven microparticle dispensers are integrated in each ground shield. The electrode system is surrounded by a quadratic glass cuvette, which provides optical access to the discharge region of 300 cm^3 .

disperse microparticles of six different sizes ($1.55\text{--}14.9 \mu\text{m}$) can be injected into the gas discharge: silica microparticles with a diameter of $1.55 \pm 0.04 \mu\text{m}$ and melamine-formaldehyde (MF, $\rho = 1.51 \text{ g/cm}^3$) microparticles with diameters of 2.55 ± 0.04 , 3.42 ± 0.06 , 6.81 ± 0.1 , 9.19 ± 0.09 , and $14.9 \pm 0.26 \mu\text{m}$.

The optical particle detection system consists of a laser illumination system and a recording system, containing four progressive scan CCD-cameras. The illumination system is based on two laser diodes, with $\lambda = 686 \text{ nm}$ and a continuous wave optical power of 40 mW, the light of which is focused to a thin sheet. This laser light sheet has a full width at half maximum of about $80 \mu\text{m}$ at the focal axis. The cameras with different magnifications and fields of view record the light scattered by the microparticles at 90° . To analyze the microparticle motion, we used the “overview camera” that has a field of view (FOV) of $58.6 \text{ mm} \times 43.1 \text{ mm}$. It shows the entire microparticle cloud between the electrodes. The plasma glow is filtered out. To observe the plasma glow dynamics, we used the “glow camera” with a slightly extended field of view of $68.6 \text{ mm} \times 50.1 \text{ mm}$. The cameras follow the PAL standard with a resolution of 768×576 pixels. Each camera provides two composite time interlaced video channels with 25 Hz frame rate. For each experiment, only four of the possible eight camera channels can be recorded on to hard disks. If both video channels from one camera are selected for recording, they can be combined to a 50 Hz progressive scan video.

B. Experimental conditions

The heartbeat experiments were performed for a set of 18 different experimental conditions (see Table I). The experiments were performed in argon and neon and designed to cover a broad range of pressures (8–100 Pa), microparticle sizes ($6\text{--}15 \mu\text{m}$), and forward rf powers (24–483 mW).

Note that argon plasmas give the best conditions for a homogeneous complex plasma with a small void, while neon plasmas result in a bigger void.¹ Argon has a smaller ionization potential: The first ionization potential of argon is $I_{\text{ion}}^{\text{Ar}} = 15.76 \text{ eV}$, whereas it is $I_{\text{ion}}^{\text{Ne}} = 21.56 \text{ eV}$ for neon.²⁰ At a given forward rf power and gas pressure, the ionization rate of argon is higher than in neon, hence the plasma is denser.

There are two main differences compared to experiments presented in Refs. 17, 18, 21, and 22. In our experiments, the monodisperse microparticles are larger than $6.81 \mu\text{m}$. Each single particle can be identified in the camera recordings. This allows us to track the motion of individual particles and thus to analyze their kinetics. Unlike in experiments with grown particles, no contaminating components (cyclic particle growth from sputtering or chemically reactive plasmas) affected the discharge.

C. Electrical signals measurements

With PK-3 Plus, it is possible to record low-frequency (4–10 Hz) electrical signals: the root mean square (rms) rf voltage (U_{rms}) and rms rf current (I_{rms}), the rms of the harmonics in the rf current (rms harmonics), the dc current to the electrodes which is proportional to the dc self-bias, and

TABLE I. Plasma parameters, forward rf power, and measured fundamental frequencies of the heartbeat experiments. For comparison, we show also the dust plasma frequency f_{dust} and the breathing mode frequency f_{bm} (see Sec. IV D). The estimated dust density n_d is also shown (see Sec. III A). The experiments were performed under microgravity conditions on board the ISS in 2006 by Valery Tokarev (16.01.), Pavel Vinogradov (14.08.) and Thomas Reiter (19.08.).

Nr.	Gas	Diam. (μm)	Power (mW)	Press. (Pa)	F (Hz)	f_{dust} (Hz)	f_{bm} (Hz)	n_d (cm^{-3})	Mission date
I	Ar	6.8	483	35	5.96	23.4	4.5	2.1×10^4	16.01.
II	Ar	6.8	290	36	3.31	17.9	4.3	1.1×10^4	16.01.
III	Ar	6.8	94	9	4.30	17.6	4.2	1.5×10^4	16.01.
IV	Ar	9.19	483	11	2.65	15.1	3.2	1.1×10^4	19.08.
V	Ar	9.19	288	10	3.33	11.5	3.1	0.6×10^4	19.08.
VI	Ar	9.19	288	9	2.81	11.7	2.4	1.4×10^4	19.08.
VII	Ar	9.19	194	9	2.48	16.0	2.5	1.9×10^4	19.08.
VIII	Ar	9.19	192	9	2.71	11.7	2.3	1.4×10^4	19.08.
IX	Ar	14.9	192	35	0.83	6.6	1.5	0.3×10^4	14.08.
X	Ne	6.8	96	63	4.22	14.0	3.0	1.7×10^4	16.01.
XI	Ne	6.8	96	101	2.81	13.6	3.0	1.2×10^4	16.01.
XII	Ne	6.8	48	101	1.08	13.7	2.7	1.3×10^4	16.01.
XIII	Ne	9.19	288	35	5.38	12.5	2.5	1.7×10^4	19.08.
XIV	Ne	9.19	192	102	6.95	11.9	2.2	1.1×10^4	19.08.
XV	Ne	9.19	96	102	2.81	12.9	1.9	1.6×10^4	19.08.
XVI	Ne	9.19	80	102	2.15	11.3	1.9	1.3×10^4	19.08.
XVII	Ne	14.9	30	65	2.48	5.8	1.4	0.6×10^3	14.08.
XVIII	Ne	14.9	24	102	1.08	4.9	1.4	0.2×10^3	16.01.

the forward rf power (P) and reflected rf power. These measurements are synchronized to the optical recordings with an accuracy of 0.3 ms. This enables us to cross-check independently the low frequency data extracted from the time-space plots (cf. Sec. IV). The measurement errors of U_{rms} , I_{rms} , and the rms harmonics are in a range of $\pm 2\%$. For all rf power measurements, the errors are in a range of $\pm 1\%$.

The average rms rf voltage ($\langle U_{\text{rms}} \rangle$) and the average rms rf current ($\langle I_{\text{rms}} \rangle$) versus average forward rf power ($\langle P \rangle$) for all the experiments in Table I are shown in Fig. 2. The time average (...) is calculated over several heartbeat oscillation periods. These dependencies turn out to be simple: they are fitted well with the scaling laws $\langle U_{\text{rms}} \rangle \propto \langle P \rangle^{0.3}$ and $\langle I_{\text{rms}} \rangle \propto \langle P \rangle^{0.75}$. This naturally simplifies the estimation procedure.

III. COMPLEX PLASMA CONDITIONS

A. Volume and density of the microparticle clouds

In different heartbeat experiments, the volume of the microparticle cloud varied in the range $V = 10\text{--}40 \text{ cm}^3$. This value was found using the following method: the geometric

cross section of the microparticle cloud was directly obtained from the recorded images. We assumed that the cloud (and the void) shape approximated an axially symmetric oblate spheroid (see Fig. 6), the volume of which can be calculated as $V = \frac{4}{3}\pi b a^2$, where $a(b)$ is the horizontal (vertical) semi-axis. The “net” microparticle cloud volume was calculated as $V_d = V_c - V_v$, where V_c is the volume of the entire cloud and V_v is the void volume.

The density of the microparticle cloud varies in the range $n_d = 0.2 - 2 \times 10^4 \text{ cm}^{-3}$. The smallest values were always detected in the experiments with the biggest particles. The averaged “2D-density,” $n_d^{(2D)}$, was obtained by detecting the particle positions inside the individual recorded images. The “3D-density,” n_d , is derived from the relationship: $n_d = \xi [n_d^{(2D)}]^{3/2}$, where $\xi \approx 1$ is the geometric factor. The total number of microparticles in different experiments was estimated as $N_d = n_d V_d = 0.4 - 7 \times 10^5$.

B. Estimated plasma parameters

The plasma temperature and the plasma density were not directly measured in the experiments. Because they are

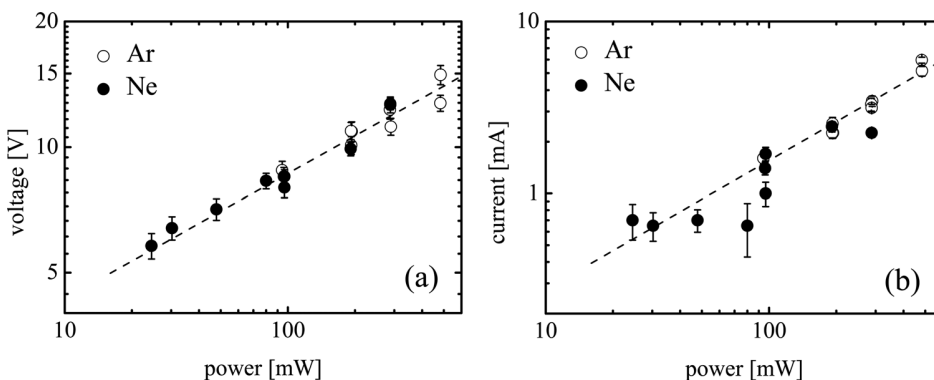


FIG. 2. Dependence of (a) average rms voltage $\langle U_{\text{rms}} \rangle$ and (b) average rms current $\langle I_{\text{rms}} \rangle$ on average forward rf power $\langle P \rangle$ for all studied discharges (see Table I). The dashed lines indicate the general trends $\langle U_{\text{rms}} \rangle [\text{V}] = 2.5 \langle P \rangle [\text{mW}]^{0.3}$ and $\langle I_{\text{rms}} \rangle [\text{mA}] = 0.07 \langle P \rangle [\text{mW}]^{0.75}$.

TABLE II. The scaling parameters to the relationships (1).

Gas	n_{e0} (cm ⁻³)	p0 (Pa)	U ₀ (V)	T _{e0} (eV)	T _{i0} (eV)
Ar	10 × 10 ⁸	60	14	2–3	0.03
Ne	1.5 × 10 ⁸	60	17	3–4	0.03

directly related to the discharge regime, these parameters can be estimated based on recently published results.^{1,23}

Probe measurements²⁴ and simulations^{1,24} show that the plasma density is basically proportional to the gas pressure and the discharge voltage and that the plasma species temperatures are roughly constant:

$$n_e = n_{e0} \frac{p}{p_0} \frac{U}{U_0}, \quad T_e = T_{e0} = \text{const}, \quad T_i = T_{i0} = \text{const}. \quad (1)$$

This is approximately true in the range of parameters, which is of interest in the given study. Additionally, it was found that the presence of microparticles leads to a decrease of the electron density in the microparticle cloud and that the electron density in the void is significantly higher.²³

The values of the electron density obtained with Eq. (1) are quite reasonable, as the comparison to Ref. 25 shows. The ion temperature is commonly considered to be equal to the neutral gas temperature. The latter is close to room temperature for the low forward rf power we operated with.

The estimation of the electron temperature values is more demanding. The electron temperatures simulated in Ref. 1 were found to be in the range $T_e = 5 - 6\text{eV}$ for neon and $T_e = 3 - 4\text{eV}$ for argon. Compared to the probe measurement data,²⁴ the 2D simulation code used in Ref. 1 overestimates the real temperatures. Note also that the experiments in Ref. 24 have been performed in the IMPF device that differs from the PK-3 Plus device in design. It is, however, possible to rescale data as proposed in Ref. 25. The set of scaling parameters determined is shown in Table II.

C. Plasma glow measurements

With the camera system of the PK-3 Plus laboratory, it is possible to simultaneously record the microparticle dynamics and the time and space resolved discharge glow.¹

The heartbeat oscillation is accompanied by a change of the discharge glow that relates to a change in the spatial distribution of ionization. (For comparison: changes in the ionization distribution are also observed in a gas discharge alternating from α to γ mode.²⁰ It is known that in reactive plasmas, the discharge switches from α mode to γ' mode during the particle growth.²⁶)

Even in a stable discharge phase the plasma glow is distributed nonuniformly. The instability manifests itself with a strong glow increase in the center of the discharge. At the same time, the glow at the periphery goes down (red curve in Fig. 3). According to Ref. 17, this bright glow phase lasts for a few milliseconds then decays rapidly within less than 1 ms, until it reaches a minimum. From our space-resolved measurements, we can see that the peripheral glow increases during this phase (blue curve in Fig. 3). Thereafter, the glow

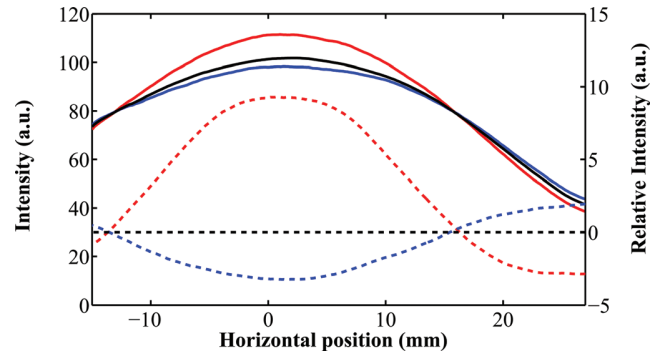


FIG. 3. (Color) Horizontal glow distribution in experiment X. The red curves correspond to the enhanced glow initiating the contraction phase of the heartbeat oscillation. The blue curves show the minimal intensity in the reopening phase of the oscillation. The time-averaged distribution is shown in black. The dashed curves show the intensity deviation from this averaged value. Note that there is a stagnation zone with approximately constant glow intensity located at 14–16 mm from the center (at 0 mm).

stays on an intermediate value for up to 1 s, then the cycle restarts. The glow dynamics can be correlated with the particle kinetics (see Sec. V).

D. The particle charge

The experimental setup used in this study does not allow us to measure the microparticle charge directly, but for a wide range of complex plasma parameters, the charge can be estimated using model assumptions. For instance, in many complex plasma studies, it has been shown that each microparticle gains about 1000 electrons per 1 μm diameter for a typical laboratory plasma with electron (ion) density $n_{e(i)} \sim 10^8 - 10^9 \text{cm}^{-3}$ and electron temperature $T_e \sim 2 - 4\text{eV}$.^{27,28} This is a convenient “reference value” useful as a test for model predictions.

In the given study, the microparticle charge Ze , where e is the elementary charge, was estimated using the drift motion limited (DML) method explained in Ref. 29. For all the cases listed in Table I, the value of the specific charge Ze/d is in the range $Ze/d \in [1000, 1400]e$, where d is the particle diameter measured in micrometers. For instance in experiment II, Z was estimated as $Z = 9800$ and in experiment IX as $Z = 22\,700$.

For comparison: in the orbital motion limited (OML) model $Z \approx 1400aT_e$, where a is the particle radius in micrometers and T_e is the electron temperature in electronvolts.³⁰ This results in $Z/d \approx 700 T_e = 1400$ for $T_e = 2 \text{eV}$. That gives an upper limit for the specific particle charge estimate.

In Sec. IV E, the above estimates of the particle charge are cross-checked using measurements of the dust acoustic waves (DAW) propagating in the complex plasma.

IV. DYNAMICAL PROCESSES OBSERVED IN THE COMPLEX PLASMA

The heartbeat oscillation is a succession of contractions and expansions of the void defined by the microparticles.¹⁸ In the beginning, it manifests itself as an instability accompanied by a fast contraction of the microparticles toward the geometrical center of the discharge chamber. Then the

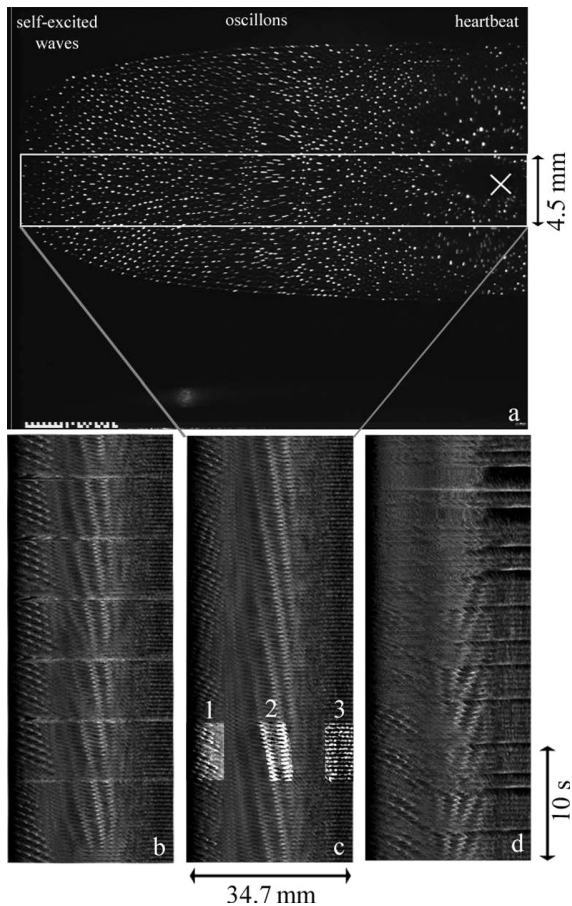


FIG. 4. Auto-oscillation patterns observed in argon at 9 Pa: (b) and (c) experiment VI with $P=288$ mW and (d) experiment VIII with $P=192$ mW. (a) A snap-shot of the microparticle cloud. The cross indicates the center of the chamber. The rectangle marks the region used for preparing the time-space plots shown in the bottom panels (b)–(d). In panel (c), three features are indicated by enhanced contrast: (1) the self-excited waves propagating at the cloud edge (Ref. 25), (2) the slowly propagating oscillons (Ref. 14), and (3) the heartbeat oscillations. (b) The six horizontal lines crossing the panel are disturbances caused by short-time voltage pulses. (d) Unstable heartbeat oscillations at low forward rf power.

microparticles drift outward restoring their initial position while the oscillation cycle restarts.

The observed heartbeat oscillations can be weak (linear stage) where almost the whole cloud oscillates synchronously. It can also be strongly nonlinear, with complicated oscillation patterns (Fig. 4). We observed such kinds of behavior in experiments IV–VIII. Here, the heartbeat oscillations are accompanied with other instabilities like self-excited waves²⁵ that are connected to ion- and dust-acoustic instabilities in dusty plasmas.^{31,32} These instabilities can occur in our experimental conditions.³³ Such secondary waves can themselves have profound nonlinear features like spatial frequency clustering.³⁴ The pattern realized in our experiment was strongly dependent on the discharge regime, in particularly on the forward rf power.

A. Observed oscillation patterns

In this section, the complicated oscillation patterns excited by the heartbeat oscillation are illustrated using

experiments VI and VIII. The patterns consist of three main elements: Self-excited waves on the outer edges of the microparticle cloud, heartbeat oscillations close to the center, and oscillons in the transition region. The patterns are visualized in Fig. 4 using time-space plots. The preparation of time-space plots is discussed in Sec. IV B.

Self-excited waves were present at the edge of the cloud. They are visible as oblique bright stripes in the left part of the panels (b)–(d) shown in Fig. 4 and emphasized in the contrast enhanced region 1 in panel (c). These waves are not caused by the heartbeat oscillations and their frequency is not correlated with that of the heartbeat oscillation.²⁵

Heartbeat oscillations occur at the center of the cloud, in the right part of Fig. 4(a) and in panels 4(b)–4(d). The regular contractions during experiment VI [panels 4(b) and 4(c)] can be seen as alternating narrow bright and dark lines. Also compare the contrast enhanced region 3. The oscillations were stable over 83 s, which is more than 230 oscillation cycles. The pattern remained stable even under an external disturbance caused by a set of short-time pulses (changes of the dc offset on the electrodes), visible as bright horizontal stripes in Fig. 4(b). After the perturbation the restoring time of the oscillation pattern was less than the oscillation period of 0.36 s. At lower rf power, the heartbeat oscillations became unstable and irregular [experiment VIII, see Fig. 4(d)]. The oscillations stopped abruptly and a large void appeared. This phase can be recognized as large dark areas in the right part of the panel. After a short time, the void collapsed again and the regular heartbeat oscillations were restored.

The heartbeat oscillation excites the propagation of oscillons.¹⁴ In the time-space plots, the oscillons are visible as slightly slanted bright lines in the central part, see region 2 with enhanced contrast. The internal structure of the oscillons consists of vibrating particles. The oscillation periods of the microparticles in the oscillons are strongly correlated with the heartbeat frequency.

It is an interesting question whether the oscillation patterns in complex plasmas show universal properties under different experimental conditions. From our measurements and from previously published data^{4,14,17,35,36} it is evident qualitatively that some simple dependencies should exist. For instance, it follows directly from the data listed in Table I that the oscillation frequency increases with decreasing particle size and with increasing forward rf power. The trend for fundamental frequencies to grow with the forward rf power remains true for the data available from a variety of experimental setups and conditions (cf. Fig. 5).

The dependence of the fundamental frequency on other parameters is less evident, either because the parameter space has not yet been mapped sufficiently by experiments or because some parameters could neither be measured nor be estimated. The latter is especially true in experiments with grown particles where the information about particles—like size distribution, density, charge, kinetics—is missing, and the discharge itself is modified uncontrollably by the products of the growth process.

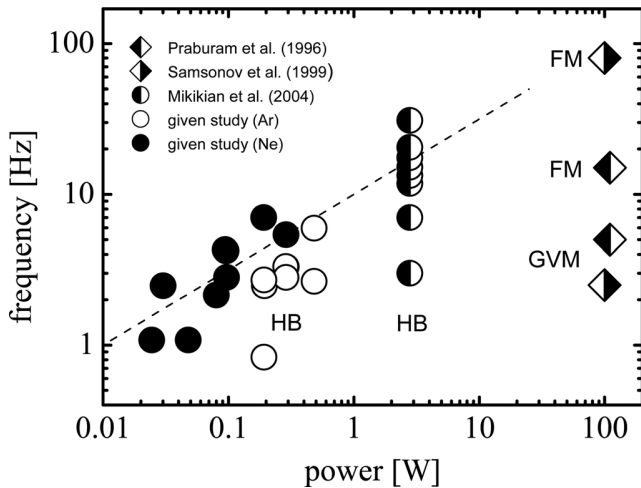


FIG. 5. The oscillation frequency shows a general trend to grow with the rf power: (diamonds) experimental data from Praburam and Goree (Ref. 35) and Samsonov and Goree (Ref. 4) (argon), (half-open circles) experimental data from Mikikian *et al.* (Ref. 36) (argon), and (circles) given study (argon and neon, monodisperse microparticles). In Refs. 4 and 36, the particles are grown in the discharge. In Ref. 36, the heartbeat frequency is lowered due to failed contractions following a mixed mode oscillation pattern (Ref. 17). The dashed line ($f \propto P^{1/2}$) is shown as a reference. HB, FM, and GVM stand for “heartbeat mode,” “filamentary mode,” and “great void mode.”

B. Frequency analysis: Method of time-space plots (periodograms)

To demonstrate the analysis methods, let us consider the example shown in Fig. 6. It shows a snapshot of the microparticle cloud obtained in experiment II (cf. Table I). The experimental conditions were argon gas with a pressure of 36 Pa, MF particles with a diameter of $6.81 \mu\text{m}$, 290 mW forward rf power at a peak-to-peak voltage of 32 V, and an $\langle I_{\text{rms}} \rangle = 3.5 \text{ mA}$. The microparticle dynamics were recorded at a frame rate of 25 fps.

Beyond the small central void the cloud is homogeneous with an averaged interparticle separation $\Delta \sim 450 \mu\text{m}$ and a mean particle number density $n_d \sim 10^4 \text{ cm}^{-3}$. The whole microparticle cloud was continuously oscillating, indicating a rather weak instability (cf. Sec. IV A).

Time-space plots are used to measure the line density evolution and thereby illustrate the dynamics of the microparticle cloud in a straightforward way. These plots are assembled as follows: Inside a narrow horizontal band of well-defined width (see below) taken close to the center of each frame (cf. Fig. 6), the pixel intensities are summarized vertically, resulting in a single line representing the horizontal pixel intensity distribution. These lines are stacked in sequence. The resulting image shows the temporal evolution of the horizontal brightness distribution in the recorded images, and thus (to some extent) the temporal evolution of the line density of the microparticle cloud.

The resulting (t, x) map (prepared from several hundred images) is decomposed into its constituent frequencies and wave numbers $\sim e^{-i\omega t + ikx}$, with $\omega = 2\pi f$ and $k = 2\pi/\lambda$, where f is the frequency, k is the wave number and λ is the wavelength of the line density variations. The spectra calculated with the help of discrete Fourier transform (DFT) are

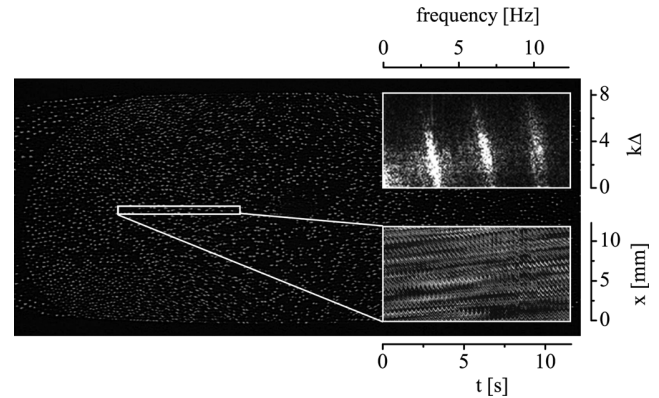


FIG. 6. A vertical cross-plane of the dense microparticle cloud of experiment II, Table I. FOV = $47.2 \text{ mm} \times 23.9 \text{ mm}$ (overview camera). The rectangle marks the $12.3 \text{ mm} \times 0.8 \text{ mm}$ region used to detect the microparticle vibrations and to obtain the oscillation frequencies. The x -position is counted from the left edge of the rectangle. Inserts show (bottom) the time-space plot (see text for the preparation details) and (top) the DFT frequency-wave number spectrum obtained from it. The interparticle separation is $\Delta = 0.45 \text{ mm}$.

shown in Fig. 6 (top inset) and Fig. 9(d). There the wave numbers are normalized by the interparticle separation Δ . The maximal inaccuracy of the measured positions of the spectrum lines is estimated to be less than 30%. It is important to note that in order to obtain a good Fourier spectrum, the width of the band has to be chosen carefully: if it is too narrow, only a few particles will contribute to the time-space plot and consequently no pertinent information can be extracted concerning the cloud dynamics; if it is too wide, the intensities of several particles will overlap across the band and pixel intensity variations will only reflect microparticle density variations at a long wavelength scale while the fine details will be lost. A generally good choice for the band’s width is when three–four layers of microparticles are included.

C. Correlation of the particle oscillation periods and the electrical signals oscillations

The heartbeat oscillations also cause variations in the measurements of the electrical signals. These measurements

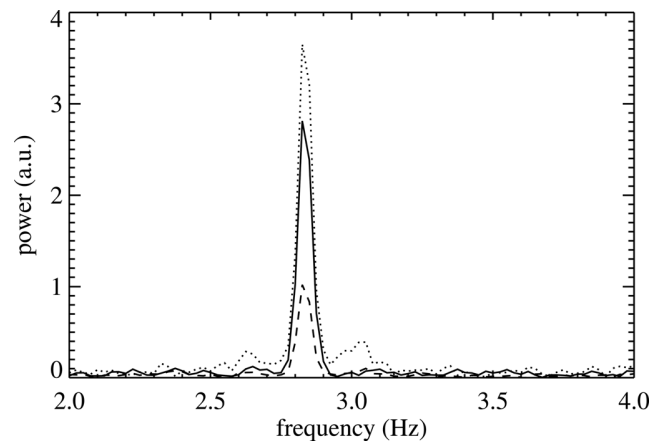


FIG. 7. DFT spectra obtained for (solid line) the time-space plot (Fig. 4), (dotted line) the rms rf voltage, and (dashed line) the rms rf current oscillations, in the phase of stable heartbeat oscillations of experiment VI, Table I.

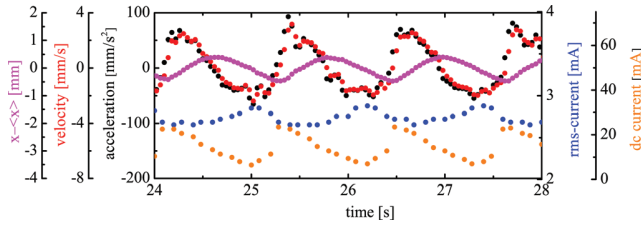


FIG. 8. (Color) Trajectory of an individual particle in experiment IX, Table I. The particle velocity $v = \dot{x}$ and the “net force” acceleration $a = \ddot{x} + \gamma\dot{x}$ have been calculated from the tracked particle trajectory. $\gamma = 25.7 \text{ s}^{-1}$ is the damping rate of the Epstein drag force (Ref. 37). Note a well-manifested correlation shown by the net force, accelerating the particle, and dc-current oscillation. The time axis is the same as in Fig. 9.

are related to the global discharge characteristics. At this global scale, the results of electrical signal measurements agree reasonably well with those obtained from particle dynamics measurements.

In Fig. 8, we compare the trajectory of an individual particle with the electrical signals recorded in experiment IX, Table I. Note that the time moments when the particles gain momentum from the plasma correlate well with the sharp increase shown by the oscillating dc-current.

Moreover, the base frequency of the particle vibration matches the base frequency of the variations of rms rf voltage (U_{rms}) and current (I_{rms}). For instance, a comparison of the oscillation frequency of the microparticles and of the recorded electrical signals during the phase of stable oscillations of experiment VI (cf. Fig. 4) is shown in Fig. 7. The measured frequencies agree well (for more details see Ref. 14). Figure 9 presents the housekeeping data (pressure and several electrical measurements) and the time-space plot for experiment IX. A reasonably good agreement between not only the fundamental frequencies but also their higher harmonics is evident from the derived Fourier spectra.

D. The dust-plasma frequency and the breathing mode frequency

From a physical point of view, the heartbeat oscillations must arise from oscillations ubiquitous in complex plasmas.

One could expect that the frequencies must be proportional, e.g., to the dust-plasma frequency.³⁸ The regular microparticle oscillations can also be associated with the global modes affected by plasma confinement.^{14,39} To decide which mechanism of plasma oscillations can be employed, the frequencies of these oscillations are calculated from plasma parameters (cf. Sec. III B).

The dust-plasma frequency is defined by

$$f_{\text{dust}} = \frac{1}{2\pi} \sqrt{\frac{4\pi(Ze)^2 n_d}{m_d}}, \quad (2)$$

where Ze , n_d , and m_d are the microparticle charge, the microparticle number density, and the microparticle mass, respectively.³⁸ The calculated values of f_{dust} are listed in Table I. In the majority of cases, the dust-plasma frequency is four times higher than the one exhibited by the oscillating microparticles [see Fig. 8(a)].

This is not surprising as the oscillating microparticles visibly do not behave like individually “caged” particles but reveal a collective motion typical for complex plasma global modes. This is one of the important features of the instability discussed: a *breathing mode*^{40,41} is primarily excited. The breathing mode and its first harmonics are easily identified in the spectra shown in Figs. 6 and 9. In our case, it is actually a “classical” variant of the breathing mode with essentially “radially polarized” particle vibrations. Noteworthy is the correlation of the particle vibration frequency with the frequency of oscillations of the dc current, the low frequency modulation of rms harmonics as described in Sec. IV C. The

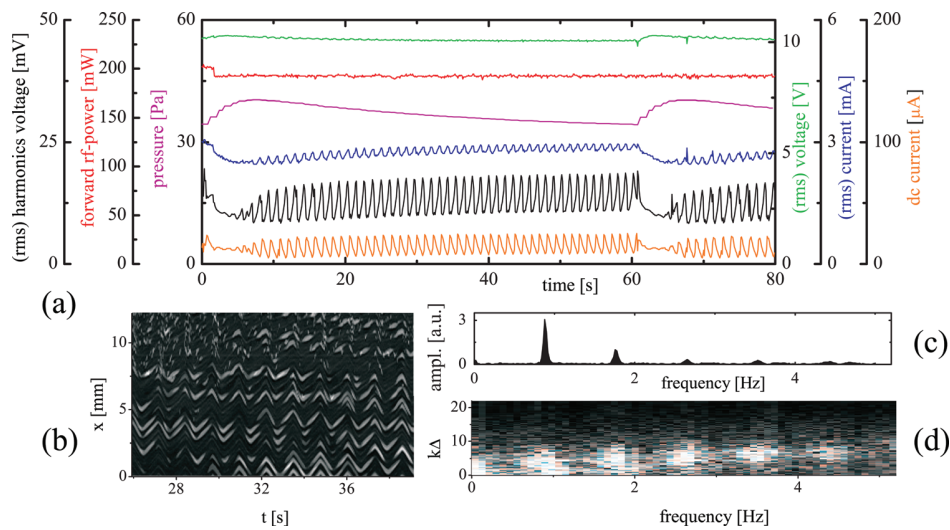


FIG. 9. (Color) Analysis of the lowest frequency experiment in argon performed with $14.9 \mu\text{m}$ particles experiment IX, Table I. (a) A set of the housekeeping data, (b) a fragment of the time-space plot ($12.2 \text{ mm} \times 13.2 \text{ s}$; $26.9 \text{ s} \leq t \leq 40.1 \text{ s}$), (c) Fourier spectrum of the dc current with a fundamental frequency $f = 0.87 \pm 0.03 \text{ Hz}$, and (d) Fourier spectrum obtained from the time-space plot giving a frequency-wave number plot with a fundamental frequency $f = 0.83 \text{ Hz}$. The interparticle separation is $\Delta = 0.69 \text{ mm}$. Note a well pronounced correlation between the electrical signal oscillation and the particle oscillation pattern. The gas inside the discharge chamber was refreshed every 60 s during the experiment. The gas refreshments were followed by an increase in pressure, which correlated well with tentative oscillation suppression periods.

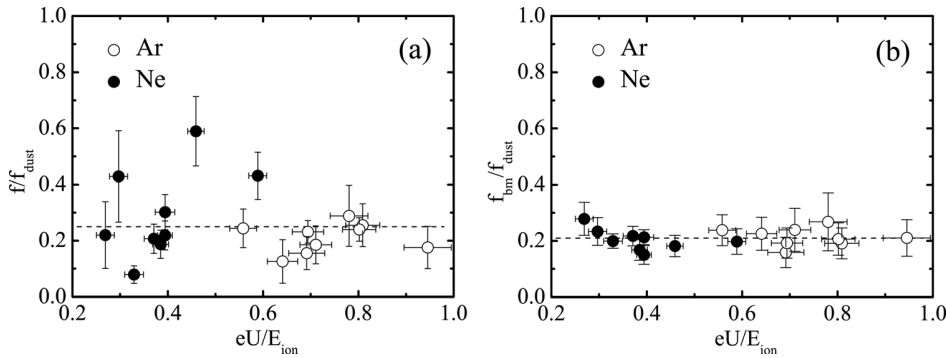


FIG. 10. The oscillation frequencies of (a) the heartbeat instability and (b) the breathing mode normalized to the dust-plasma frequency vs (rms) discharge voltage normalized to ionization potential. The dashed lines show the mean values: (a) $\langle f/f_{\text{dust}} \rangle = 0.25 \pm 0.12$ and (b) $\langle f_{\text{bm}}/f_{\text{dust}} \rangle = 0.21 \pm 0.03$.

correlation of the horizontal oscillation of one individual particle with the rms rf and dc current oscillations is emphasized in Fig. 8. In the context of breathing mode oscillations, the particle-energizing mechanism can be naturally explained as a temporary enhancement of the radial confinement strength followed by a short-time degradation. The detailed theoretical explanation of the feedback mechanism is still outstanding.

It is well known that the breathing mode is determined primarily by the confinement conditions, that is, by the strength of the electric field caging the cloud.³⁰ Assuming that the horizontal voltage drop $\delta U \approx U$ (see Ref. 1), the radial component of the electric field strength can be estimated and the oscillation frequency is given by

$$f_{\text{bm}} \approx \frac{2}{\pi D} \sqrt{\frac{2Z|e|U}{m_d}}, \quad (3)$$

where D is the horizontal diameter of the microparticle cloud. The estimated values of f_{bm} are listed in Table I. They agree well with those observed experimentally.

The ratio of the breathing mode frequency to the dust-plasma frequency is shown in Fig. 10(b) versus the reduced rms rf voltage. Surprisingly, all data points concentrate well around $f_{\text{bm}}/f_{\text{dust}} \approx 1/5$. This frequency ratio can be interpreted also in a different way. From the relationships (2) and (3), it follows that $E'_{\text{bm}}/4\pi\rho_{\text{dust}} = 1/8(f_{\text{bm}}/f_{\text{dust}})^2$, where $\rho_{\text{dust}} = Zen_d$ is the total microparticle charge density, $E'_{\text{bm}} = U/R^2$ is the scale of the electric field strength variation, and $R = D/2$. Because $E'_{\text{bm}} \sim \delta\rho$, where $\delta\rho$ is the charge decompensation inside the complex plasma, we come to the important conclusion:

$$\delta\rho/\rho_{\text{dust}} \approx 0.5 - 1.5\%.$$

Therefore, the smallness of the ratio $f_{\text{bm}}/f_{\text{dust}} \approx 1/5$ evidences the global quasineutrality of the entire complex plasma cloud.

E. Self-excited waves and “dust sound”

Additionally, intense heartbeat oscillations can give rise to collective modes also detected in the particle excitation spectra, e.g., the dust acoustic mode. The traces of the “dust sound” are seen, for instance, in the spectra shown in Figs. 6

and 9. The fundamental harmonic along with its resonant super-harmonics form a peculiar pearl-necklace-like pattern in (k, ω) space, visibly aligned, and therefore unmistakably indicating an acoustic-like dispersion relationship, $\omega \sim k$. The slope of the line highlighted by the pearl-necklace-like pattern gives us the speed of sound. For instance, it is $C_s = 5.1 \pm 2.5$ mm/s in the spectrum of experiment II shown in Fig. 6, while it is $C_s = 2.6 \pm 1.1$ mm/s in the spectrum for experiment IX shown in Fig. 9.

Both estimates agree fairly well with the theoretical expectations of the dust acoustic wave speed:³⁸

$$C_{\text{DAW}} = \sqrt{\frac{Z^2 T_i}{m_d} \frac{n_d}{n_e + Zn_d}}. \quad (4)$$

Using our charge estimates as described in Sec. III D, we obtain for experiment II ($n_d = 1.1 \cdot 10^4 \text{ cm}^{-3}$) an estimated $C_{\text{DAW}} = 6.4$ mm/s and for experiment IX ($n_d = 3 \cdot 10^3 \text{ cm}^{-3}$) $C_{\text{DAW}} = 2.5$ mm/s. As mentioned in Sec. III D, we can also use the measured dust acoustic wave speed to cross-check the estimate of the particle charge. For the whole set of experiments in Table I, we get on average $Z^{\text{DAW}}/Z^{\text{DML}} = 1.0 \pm 0.2$, where Z^{DAW} is the value of the particle charge obtained with Eq. (4) and the experimentally measured speed of sound, while Z^{DML} is the value obtained using the method from Ref. 29

As mentioned in Sec. IV A, self-excited wave-ridges may start to propagate at the edges of the microparticle cloud in some cases. A good example for such an event is seen in Fig. 4, where these waves are generated well in the periphery part of the microparticle cloud, far away from the void in the center. These waves are not sound-like, and they are never spread out all over the entire cloud.

V. THE ONSET OF INSTABILITY

The study of the heartbeat oscillations would not be complete without even a brief discussion of the microparticle dynamic aspects directly related to the onset of the instability. They can be explored directly in the given experiments, even quantitatively, especially in the domain of low frequency oscillations. For example, in the conditions of the aforementioned low-frequency experiment IX (Table I) the time-resolved measurements provided such kind of detailed information. There is a unique opportunity to demonstrate

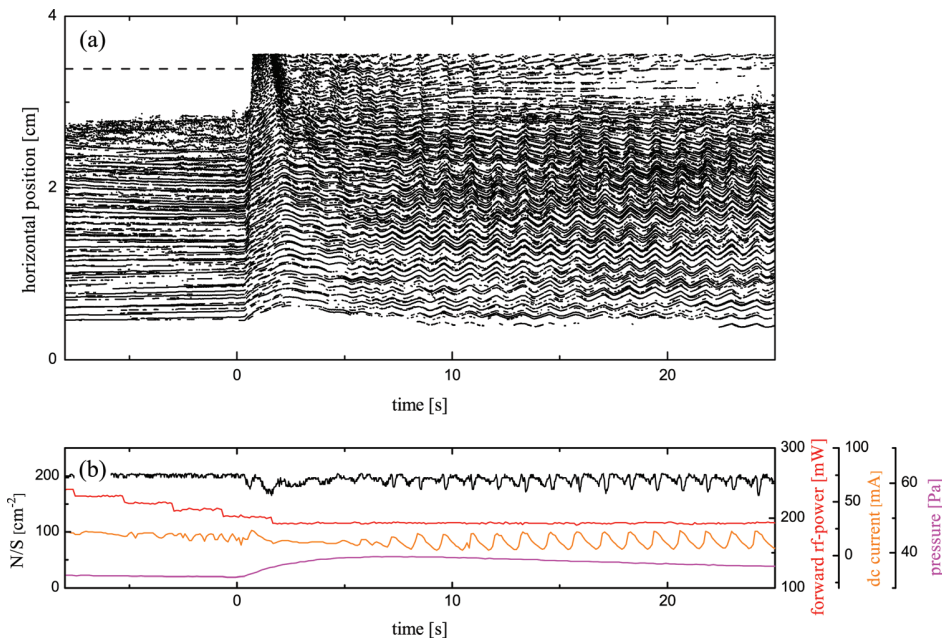


FIG. 11. (Color) The onset of the heartbeat instability observed in the experiment IX, Table I. (a) The horizontal position of the particles vs time taken inside a slice of a width $\Delta y = 2$ mm across the cloud through the void. The dashed line indicates the geometric center. (b) The correlation of the “area density” N/S of the cloud with the housekeeping signals. Top to bottom: the area density N/S , the forward rf-power, the dc current, and the pressure. Here, N is the number of the particles inside the rectangle of the size $S = \Delta x \times \Delta y = 20 \times 17$ mm². The time scale is the same as in Fig. 9.

whether there is any relation between some of the important experiment parameters and the occurrence of the instability, e.g., whether a minimum dust density, critical rf power, or neutral gas pressure are required.

Figure 11(a) shows the tracked particle positions during the transitions phase from a microparticle cloud with stable void to a stable heartbeat oscillation. The changes in the important parameters, rf power, pressure, and particle density $n^{(2d)} = N/S$ are shown together with the measured dc current in Fig. 11(b). The heartbeat instability in the given experiment occurred as the forward rf power was stepped down. The total change in the forward rf power amounts to 22%. Already at $t \approx -5$ s, low amplitude particle oscillations started at the void boundary and dc current oscillations appeared. From all electrical measurements, dc current seems to be the most sensitive to heartbeat oscillations. At $t \approx 0$ s, a gas puff is increasing the neutral gas pressure by approximately 15% and the void disappears. The stable heartbeat oscillation is fully developed from $t \approx 10$ s. A smaller void establishes from $t \approx 15$ s. The average particle density after $t = 0$ s is reduced by $\approx 4\%$ from the initial value. It is important to note that in all experiments in Table I, the rf power was stepped down before the onset of the instability. Yet, not all transitions contained a gas puff and the average density of the microparticle cloud stayed almost constant (going down marginally). We could also determine a general trend that the higher the neutral gas pressure the higher the critical value of forward rf power at which the heartbeat instability arose. Also note the second gas puff at $t \approx 62$ s recorded for experiment IX, Table I (Fig. 9). The restoration time of the heartbeat oscillation is 10 s, the same as for the gas puff at $t \approx 0$ s. In this experiment, $C_{DAW} \approx 2.5$ mm/s (see Sec. IV E). Hence, dust acoustic waves need ≈ 12 s to travel through the shown part of the cloud [$\Delta x \approx 30$ mm, see Fig. 11(a)]. The particles in the cloud oscillate mainly in phase, i.e., basically no waves are

propagating through the cloud during the steady state of the heartbeat oscillation.

The experimental setup on board the ISS limits the possibility to conclude on the mechanism of the instability itself by a few reasons. The PK-3 Plus laboratory cannot provide information below the time scale of 20 ms for the particle cloud dynamics and below 100 ms for the housekeeping signals measurements. Hence, the time resolution is not enough to resolve the dynamics of the plasma ions—the leading agent of the instability. For the conditions of our experiments, the ion (ambipolar) diffusion time can be estimated as $\tau_{Di} \approx 1 - 20$ ms (Ref. 20) or even less.^{4,15-18} There are still several open questions concerning the heartbeat instability and oscillations, most importantly a complete theoretical model and the mapping of the heartbeat instability in terms of discharge parameters and microparticle number densities. As long as no quantitative model for the occurrence of the heartbeat instability exists, it is not clear which “canonical” variables control this phenomenon and how they are related to experimental parameters. Therefore mapping of the parameter space is not feasible.

VI. CONCLUSION

In our experiment, the heartbeat instability has been observed at a particle number density of $n_d = 0.2 - 2 \times 10^4$ cm⁻³. In this survey, the transition from a cloud with stable void to heartbeat oscillations was accompanied by only a marginal variation of the cloud density. In all cases we explored the instability sets in after decreasing the forward rf power. The heartbeat phenomenon occurs for a wide range of experimental parameters as it is obvious from our experiments and previous publications.^{4,35,36} We conclude that the instability conditions depend on the interplay of local ionization rate, particle charge, and cloud density.

The possibility to resolve the microparticle dynamics at the kinetic level is crucial for understanding the heartbeat phenomenon. In addition, the measurement of the microparticle kinetics allows to probe plasma parameters and to cross-check the estimates of experiment parameters that had to be calculated using theoretical predictions. For instance, the microparticle charge was calculated using the DML²⁹ and OML³⁰ theories and could be cross-checked using measurements of the dust acoustic wave speed. It was found that the discrepancy between these three estimates is less than 20%. The frequency of the heartbeat oscillation has been measured independently from the time-space plots (periodograms) depicting the temporal evolution of line density, the direct tracking of the particle positions, and the housekeeping data. We showed that the acceleration of microparticles is strongly correlated with changes in the electrical signals—especially the dc current related to dc self-bias of the electrodes—and found significant agreement between the DFT spectra of particle motion and electrical signals. Additionally by comparing the predictions for the dust-plasma frequency and the breathing mode frequency for our parameters, a fixed relation of $f_{bm}/f_{dust} \simeq 1/5$ has been found. From this relation, global quasineutrality of the entire complex plasma cloud can be deduced. Combining measurements and estimates, it was possible to relate the heartbeat oscillation to a global breathing mode of the microparticles.

ACKNOWLEDGMENTS

We thank the valuable discussions with M. Chaudhuri and all members of the PK-3 Plus team. Gefördert von der Raumfahrt-Agentur des Deutschen Zentrums für Luft und Raumfahrt e. V. mit Mitteln des Bundesministeriums für Wirtschaft und Technologie aufgrund eines Beschlusses des Deutschen Bundestages unter dem Förderkennzeichen 50 WP 0203 and by RFBR Grant No. 08-02-00444-a.

¹H. M. Thomas, G. E. Morfill, V. E. Fortov, A. V. Ivlev, V. I. Molotkov, A. M. Lipaev, T. Hagl, H. Rothermel, S. A. Khrapak, R. K. Sütterlin, M. Rubin-Zuzic, O. F. Petrov, V. I. Tokarev, and S. K. Krikalev, *N J. Phys.* **10**, 033036 (2008).

²G. E. Morfill, H. M. Thomas, U. Konopka, H. Rothermel, M. Zuzic, A. Ivlev, and J. Goree, *Phys. Rev. Lett.* **83**, 1598 (1999).

³J. Goree, G. E. Morfill, V. N. Tsytovich, and S. V. Vladimirov, *Phys. Rev. E* **59**, 7055 (1999).

⁴D. Samsonov and J. Goree, *Phys. Rev. E* **59**, 1047 (1999).

⁵V. N. Tsytovich, *Phys. Scr. T* **89**, 89 (2001).

⁶V. N. Tsytovich, S. V. Vladimirov, and G. E. Morfill, *JETP* **102**, 334 (2006).

⁷V. N. Tsytovich, S. V. Vladimirov, and G. E. Morfill, *Phys. Rev. E* **70**, 066408 (2004).

⁸V. N. Tsytovich, S. V. Vladimirov, G. E. Morfill, and J. Goree, *Phys. Rev. E* **63**, 056609 (1999).

⁹K. Avinash, A. Bhattacharjee, and S. Hu, *Phys. Rev. Lett.* **90**, 75001 (2003).

¹⁰S. V. Vladimirov, V. N. Tsytovich, and G. E. Morfill, *Phys. Plasmas* **12**, 052117 (2005).

¹¹M. R. Akdim and W. J. Goedheer, *Phys. Rev. E* **65**, 015401 (2001).

¹²M. Tribeche, K. Aoutou, and T. H. Zerguini, *Phys. Plasmas* **12**, 32305 (2005).

¹³M. Kretschmer, S. A. Khrapak, S. K. Zhdanov, H. M. Thomas, G. E. Morfill, V. E. Fortov, A. M. Lipaev, V. I. Molotkov, A. I. Ivanov, and M. V. Turin, *Phys. Rev. E* **71**, 056401 (2005).

¹⁴S. K. Zhdanov, M. Schwabe, R. Heidemann, R. Sütterlin, H. M. Thomas, M. Rubin-Zuzic, H. Rothermel, T. Hagl, A. V. Ivlev, G. E. Morfill, V. I. Molotkov, A. M. Lipaev, O. F. Petrov, V. E. Fortov, and T. Reiter, *New J. Phys.* **12**, 043006 (2010).

¹⁵M. Cavarroc, M. Mikikian, Y. Tessier, and L. Boufendi, *Phys. Plasmas* **15**, 103704 (2008).

¹⁶M. Mikikian, M. Cavarroc, L. Couëdel, and L. Boufendi, *Phys. Plasmas* **13**, 092103 (2006).

¹⁷M. Mikikian, M. Cavarroc, L. Couëdel, Y. Tessier, and L. Boufendi, *Phys. Rev. Lett.* **100**, 225005 (2008).

¹⁸M. Mikikian, L. Couëdel, M. Cavarroc, Y. Tessier, and L. Boufendi, *N. J. Phys.* **9**, 268 (2007).

¹⁹K. N. Ostrikov, S. V. Vladimirov, M. Y. Yu, and G. E. Morfill, *Phys. Rev. E* **61**, 4315 (2000).

²⁰M. A. Lieberman and A. J. Lichtenberg, in *Principles of Plasma Discharges and Materials Processing*, edited by Wiley (Wiley, New York, 1994).

²¹M. Cavarroc, M. Mikikian, Y. Tessier, and L. Boufendi, *Phys. Rev. Lett.* **100**, 045001 (2008).

²²M. Mikikian and L. Boufendi, *Phys. Plasmas* **11**, 3733 (2004).

²³M. Klindworth, O. Arp, and A. Piel, *Rev. Sci. Instrum.* **78**, 033502 (2007).

²⁴M. Klindworth, O. Arp, and A. Piel, *J. Phys. D* **39**, 1095 (2006).

²⁵M. Schwabe, M. Rubin-Zuzic, S. Zhdanov, H. M. Thomas, and G. E. Morfill, *Phys. Rev. Lett.* **99**, 095002 (2007).

²⁶A. Bouchoule and L. Boufendi, *Plasma Sources Sci. Technol.* **3**, 292 (1994).

²⁷H. Ikezi, *Phys. Fluids* **29**, 1764 (1986).

²⁸T. Matsoukas and M. Russell, *J. Appl. Phys.* **77**, 4285 (1995).

²⁹G. E. Morfill, U. Konopka, M. Kretschmer, M. Rubin-Zuzic, H. M. Thomas, S. K. Zhdanov, and V. Tsytovich, *N. J. Phys.* **8**, 7 (2006).

³⁰M. Bonitz, C. Henning, and D. Block, *Rep. Prog. Phys.* **73**, 066501 (2010).

³¹M. Rosenberg, *Planet. Space Sci.* **41**, 229 (1993).

³²R. L. Merlino, A. Barkan, C. Thompson, and N. D'Angelo, *Phys. Plasmas* **5**, 1607 (1998).

³³N. D'Angelo and R. L. Merlino, *Planet. Space Sci.* **44**, 1593 (1996).

³⁴K. O. Menzel, O. Arp, and A. Piel, *Phys. Rev. Lett.* **104**, 235002 (2010).

³⁵G. Praburam and J. Goree, *Phys. Plasmas* **3**, 1212 (1996).

³⁶M. Mikikian, M. Cavarroc, N. Chaumeix, and L. Boufendi, in *Proceedings of the 31st EPS Conference on Plasma Physics, London*, edited by P. Norreys and H. Hutchinson (European Physical Society, Petit-Lancy, 2004), Vol. 28G of ECA, pp. 0-2.13; see http://epsppd.epfl.ch/London/pdf/02_13.pdf.

³⁷P. S. Epstein, *Phys. Rev.* **23**, 710 (1924).

³⁸P. K. Shukla and A. A. Mamun, *Plasma Phys. Controlled Fusion* **44**, 395 (2002).

³⁹T. E. Sheridan, *Phys. Rev. E* **72**, 026405 (2005).

⁴⁰C. Henning, K. Fujioka, P. Ludwig, A. Piel, A. Melzer, and M. Bonitz, *Phys. Rev. Lett.* **101**, 045002 (2008).

⁴¹T. Sheridan, C. Buckley, D. Cox, R. Merrill, and W. Theisen, *Phys. Lett. A* **329**, 88 (2004).

**7.4 New Journal of Physics (NJP):
Auto-oscillations in complex plasmas**

Auto-oscillations in complex plasmas

This article has been downloaded from IOPscience. Please scroll down to see the full text article.

2010 New J. Phys. 12 043006

(<http://iopscience.iop.org/1367-2630/12/4/043006>)

View [the table of contents for this issue](#), or go to the [journal homepage](#) for more

Download details:

IP Address: 130.183.136.86

The article was downloaded on 17/09/2010 at 15:16

Please note that [terms and conditions apply](#).

Auto-oscillations in complex plasmas

Sergej K Zhdanov^{1,4}, Mierk Schwabe¹, Ralf Heidemann¹,
Robert Sütterlin¹, Hubertus M Thomas¹, Milenko Rubin-Zuzic¹,
Hermann Rothermel¹, Tanja Hagl¹, Alexei V Ivlev¹,
Gregor E Morfill¹, Vladimir I Molotkov², Andrey M Lipaev²,
Oleg F Petrov², Vladimir E Fortov² and Thomas Reiter³

¹ Max-Planck-Institut für extraterrestrische Physik, D-85741 Garching, Germany

² Institute for High Energy Densities, Russian Academy of Sciences, 125412 Moscow, Russia

³ Deutsches Zentrum für Luft- und Raumfahrt, Linder Höhe, 51147 Köln, Germany

E-mail: zh@mpe.mpg.de

New Journal of Physics **12** (2010) 043006 (18pp)

Received 14 December 2009

Published 1 April 2010

Online at <http://www.njp.org/>

doi:10.1088/1367-2630/12/4/043006

Abstract. Experimental results on an auto-oscillatory pattern observed in a complex plasma are presented. The experiments are performed with an argon plasma, which is produced under microgravity conditions using a capacitively coupled rf discharge at low power and gas pressure. The observed intense wave activity in the complex plasma cloud correlates well with the low-frequency modulation of the discharge voltage and current and is initiated by periodic void contractions. Particle migrations forced by the waves are of long-range repulsive and attractive character.

⁴ To whom any correspondence should be addressed.

Contents

1. Introduction	2
2. Observation results	3
2.1. Experimental conditions	3
2.2. The global dynamical pattern and oscillons	4
2.3. Correlation between particle vibrations and electrical signals	5
2.4. Plasma parameters	8
3. Complex plasma as a dissipative system capable of auto-oscillations	10
4. Physical aspects of auto-oscillations in complex plasmas	10
4.1. Time and space scales of the momentum transfer	11
4.2. A charge exchange	12
4.3. Momentum and energy balance	12
4.4. A trigger mechanism for inner oscillations	14
4.5. A driving mechanism for outer oscillations	15
5. Conclusion	17
Acknowledgments	17
References	17

1. Introduction

The ability to self-sustain oscillations is typical for *auto-oscillation systems* with inertial self-excitation such as the Helmholtz resonator, well known in acoustics [1].

Hydrodynamic (or hydrodynamic-like) systems provide other examples of *oscillatory patterns* fed by streaming in the system: a flow-acoustic resonance [2], hydrothermal [3] and plastic deformation flows [4], mobile dunes [5], surface tension auto-oscillations [6], oscillating domains in planar discharges [7], self-excited dust density waves [8] and many others.

The usual assumption is that auto-oscillations are maintained by a sufficiently powerful instability allowing recirculation (hysteresis) in phase space [9, 10].

In this paper, we discuss self-sustained oscillatory and wave patterns observed in complex plasmas with the PK-3 Plus setup on board the ISS [11]. These active experiments (including as an item wave excitations [12]) have been performed recently in a particularly wide range of plasma parameters [11].

Complex plasmas are low-pressure low-temperature plasmas containing microparticles. These particles can be visualized individually with a laser beam, the light of which is scattered by the particles and then recorded with a CCD camera. Under microgravity conditions in experiments on board the ISS [11] or in parabolic flight experiments [13], the recorded particle clouds are essentially three-dimensional structures that are more or less homogeneous, albeit commonly containing a void—a ‘visibly empty region’ free of particles—at the center [14, 15].

By providing investigations of microparticle migrations at the atomistic level, such experiments may help us to understand the fundamental nature of inanimate auto-oscillations and the intrinsic dynamics of highly dissipative nonlinear structures. In particular, we will show that for fluid systems a range of processes may occur (at the microscopic level), which all play a role in the self-organization and finally lead to a simple auto-oscillatory pattern for the system as a whole.

Stable regular auto-oscillations have been observed for the first time in the experiments under microgravity conditions. It is still a challenging open question to explain the physics of this phenomenon. The intention of the paper is twofold:

- detailed analysis of available experimental data;
- focus attention on the physical mechanism of auto-oscillations.

The paper is organized as follows: in section 2, the observation results are collected. This includes the experimental conditions (section 2.1), the dynamical patterns shown by the particle vibrations (section 2.2), their correlation with measured low-frequency oscillatory components of the voltage and the current of the feeding circuitry (section 2.3), and the parameters of the complex plasma (section 2.4). The capability of a complex plasma to generate auto-oscillations (in this respect complex plasmas resemble many other dynamical systems) is discussed in section 3 and physical aspects of auto-oscillations in complex plasmas in section 4. We propose a simple electromechanical model description. To ensure that our simple scenario is valid, we check the local consistency of the time and space scales (section 4.1), the charge balance (section 4.2), the momentum and the energy balance (4.3), and possible trigger (section 4.4) and driving (section 4.5) mechanisms for oscillations. In section 5, the results are briefly summarized.

2. Observation results

2.1. Experimental conditions

The PK-3 Plus chamber, a parallel plate capacitively coupled rf discharge, is symmetrically driven by two electrodes, which have a diameter of 6 cm and are separated by 3 cm (measured voltage asymmetry does not exceed $\simeq 2\%$; all measured electrical values shown below are arithmetic means). The electrodes are surrounded by a grounded ring of 9 cm diameter and 1.5 cm width. (More technical details of the setup can be found in [11].) Particle vibrations were recorded at a rate of 50 fps and a spatial resolution of $45.05 \mu\text{m pixel}^{-1}$ ($49.6 \mu\text{m pixel}^{-1}$) in the vertical (horizontal) direction. The sample rate of the low-frequency electrical measurements was 10 Hz at the stage of stable vibrations.

The experiment we address here was performed in argon at a pressure of 9 Pa and was arranged in two stages (figure 1). In the first stage, the discharge was ignited with a peak-to-peak voltage of 37 V at an applied (rms) power of 0.181 W (the discharge power factor for the entire circuitry was estimated as about 45–60%). Melamine-formaldehyde particles with a diameter of $(9.2 \pm 1\%) \mu\text{m}$ and a mass density of 1.51 g cm^{-3} were inserted into the chamber. They formed a cloud stretched horizontally (the aspect ratio width/height $\equiv D/H \approx 64 \text{ mm}/15 \text{ mm}$) with a visually pulsating elliptically shaped void. In the maximal ‘stretched’ phase the void is $\sim 7 \times 3 \text{ mm}^2$. This discharge regime allows us to observe stable oscillations at a frequency of 3–15 Hz. The estimated gas damping rate, attenuating particle motion, was $\gamma_{\text{damp}} = 10.7 \text{ s}^{-1}$. Unlike [16]–[18] no contaminating (sputtering) components affected the discharge.

This is one of the main differences of this experiment compared to [17]: the particles are injected, not grown in a plasma, and the particle size is larger (at least one order of magnitude).

The experiment started out with a stochastically stabilized complex plasma ($t = 0 \text{ s}$ in figure 1; for details of stochastic stabilization see [11]). At $t = 20 \text{ s}$, the external stabilization was turned off, and after $\Delta t \simeq 1 \text{ s}$ delay the auto-oscillations appeared. Next at $t = 31 \text{ s}$ the

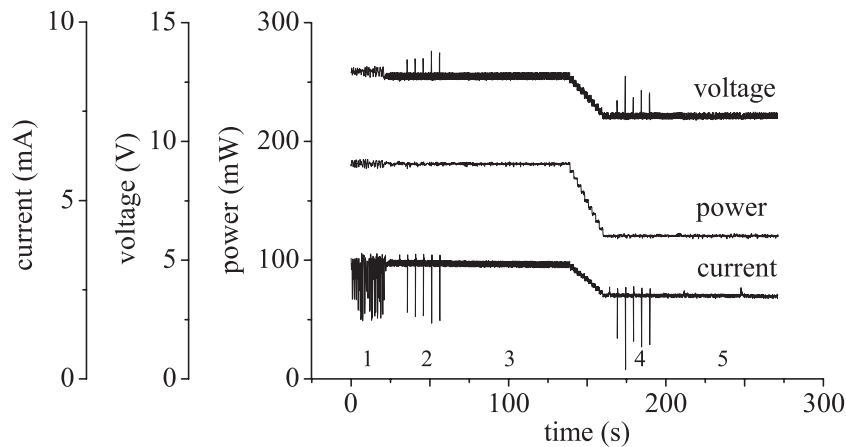


Figure 1. The (rms) discharge voltage, the current and the applied power measured during the two-stage experiment. The numbers indicate the main phases: 1, stochastic stabilization; 2, first round of short-time pulses; 3, stable-free oscillations at a higher applied power; 4, second round of short-time pulses; 5, free oscillations at a lower applied power.

plasma was stimulated by a series of six short-time voltage pulses produced by the function generator. The pulses, with a negative amplitude of -50 V, were applied to the bottom electrode through a 20 k Ω feed resistor. This produces short-time dc voltage shifts of a few volts, which leads to shock compression of the particle cloud. After this the system was observed to freely oscillate for $\simeq 83$ s without external forcing.

After $\simeq 150$ s the applied power was lowered to 0.12 W, and another form of the heart-beat instability with its almost irregular large-amplitude void constrictions started. The stable oscillation phase we address here would seem to be a completely different phenomenon. Details of the unstable (heart-beat) phase will be published elsewhere.

2.2. The global dynamical pattern and oscillons

Figure 2 visualizes the dynamical activity. Surprisingly the ‘shaking’ divides the particle cloud into two counter-moving parts, which form a stagnation zone with nearly zero particle velocity at the interface. Outside the stagnation zone the particles are seen to move along the axis at nearly constant velocity (in this particular half-cycle) as if they were *attracted* by the void. Apparently, in this phase the void behaves like a negatively charged probe, and long-range attraction is due to the ion collection effect [19]. In the next half-cycle, as the void tends to close, the particles are *repelled* from the center.

Simple estimates based on particle behavior analysis show a rather weak plasma charge oscillation with maximal decompensation of the order of $\delta n/n = 0.5\text{--}1\%$ inside the stagnation zone.

The fluctuation spectrum of the oscillating particle cloud is shown in figure 3. It consists of discrete lines, indicating regular nonlinear vibration, and the dust fluctuations with a continuous spectrum $\omega \propto k$ at a mean speed of 6.4 ± 0.3 mm s $^{-1}$. Waves in the continuum are identified as dust acoustic waves.

The periodic auto-oscillation pattern formed by particle horizontal vibrations is shown in figure 4. For depicting the oscillation pattern, we follow a simple procedure proposed in [8].

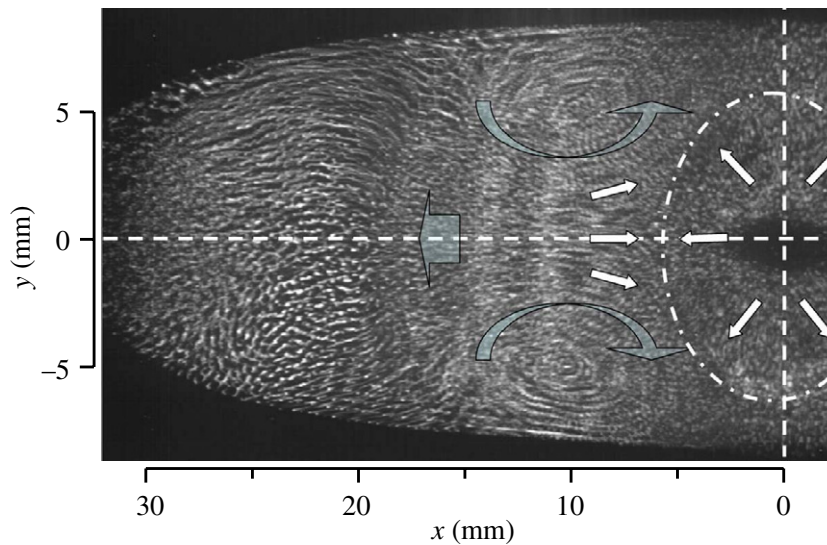


Figure 2. Ten superimposed images shifted by one period in time are shown to reveal the global dynamical pattern of the complex plasma. The main elements are: a void (the dark elliptic-shaped area to the right, at this active open stage), a quasi-spherical halo (highlighted by the dash-dotted line) with concentric waves spreading around the vibrating void, two horizontal counter-rotating global vortices with angular velocity $\simeq 0.2 \text{ s}^{-1}$ and horizontal radius $\simeq 7.5 \text{ mm}$, and an edge 'buffer' zone to the left. The boundaries of the vortices form a 'waveguide' for oscillons in-between (oscillons are identified in the middle as a few brighter vertical stripes). For the given half-cycle the dominant particle motion is as indicated by the arrows. The stagnation zone with nearly zero particle velocity is located at $x \sim 5 \text{ mm}$ (see also figure 7). The semi-transparent arrows indicate general particle drifts. The dashed lines cross at the position of the void center. The illuminating laser sheet FWHM is about $80 \mu\text{m}$.

From each image of the recorded sequence a narrow slab of size $35 \times 5 \text{ mm}^2$ centered over the void's vertical position is extracted. Then the slab is 'compressed' into a line by adding up the pixel intensities perpendicular to its longer side. The result is plotted (as a periodgram) for every frame as shown in figure 4, forming a (x, t) map. The brighter regions of this map correspond to higher particle densities. The darkest regions are particle-free, which means that the void is maximally open. The fundamental oscillation frequency shown by the cloud is

$$f_{\text{osc}} = 2.81 \pm 0.03 \text{ Hz.} \quad (1)$$

The lines of the spectrum shown in figure 3 form a sequence of harmonics of fundamental frequency $f_n = n f_{\text{osc}}$, $n = 1, 2, 3, \dots$. All harmonics up to the fourth order can be properly identified.

2.3. Correlation between particle vibrations and electrical signals

Figure 5 shows the correlation between the vertical cloud oscillations and all electrical signals. There is no correlation with the applied power. To depict the pattern of vertical oscillations the

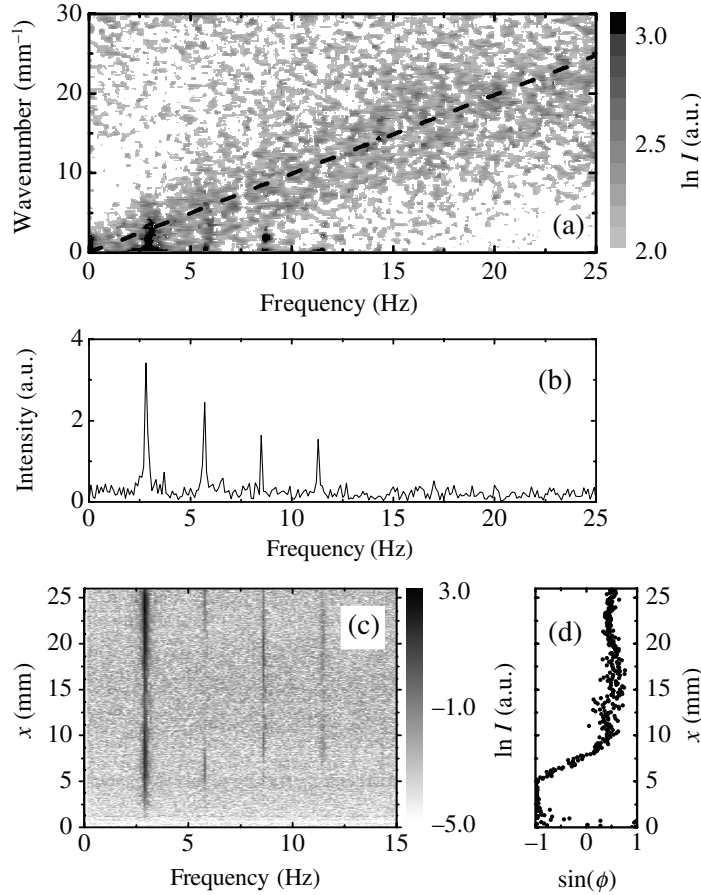


Figure 3. Spectral characteristics of the auto-oscillating complex plasma. The spectral energy is shared between two components: (a) a sound-like continuum (dust acoustic waves) and (b) discrete spectral lines. The two bottom panels show the spatial distribution (c) of the spectral intensity of the mean particle velocity fluctuations (I) and (d) the phase variation (ϕ) at the fundamental frequency. Both parameters are distributed inhomogeneously along the cloud. The spectrum (a) was calculated by making use of over 2700 particle trajectories. The spectrum (b) of the density fluctuations was obtained locally ($5.5 \text{ mm} < x < 6.5 \text{ mm}$) inside the stagnation zone. Note that the dashed line in (a) with the slope $C_{\text{DAW}} = 6.4 \text{ mm s}^{-1}$ fits well to the DAW spectrum.

aforementioned procedure is carried out over a narrow vertical slab of size $2 \times 20 \text{ mm}^2$. The result is shown in figure 5(a) as a superposition of consecutive periods.

A comparison with the oscillatory components of the effective voltage and current (figures 5(b) and (c)) shows an almost *anti-phase* behavior that is typical of pattern-creating gas discharges (see e.g. [20]). The mean components of these signals (corrected for measurement offset errors) are

$$\langle I \rangle = 3.24 \pm 0.03 \text{ mA}, \quad \langle U \rangle = 12.70 \pm 0.02 \text{ V}. \quad (2)$$

From this we obtain an average ohmic discharge resistance of $\simeq 4 \text{ k}\Omega$. (Without particles the plasma resistance was $\simeq 3.4 \text{ k}\Omega$. This value agrees well with that estimated from [21].)

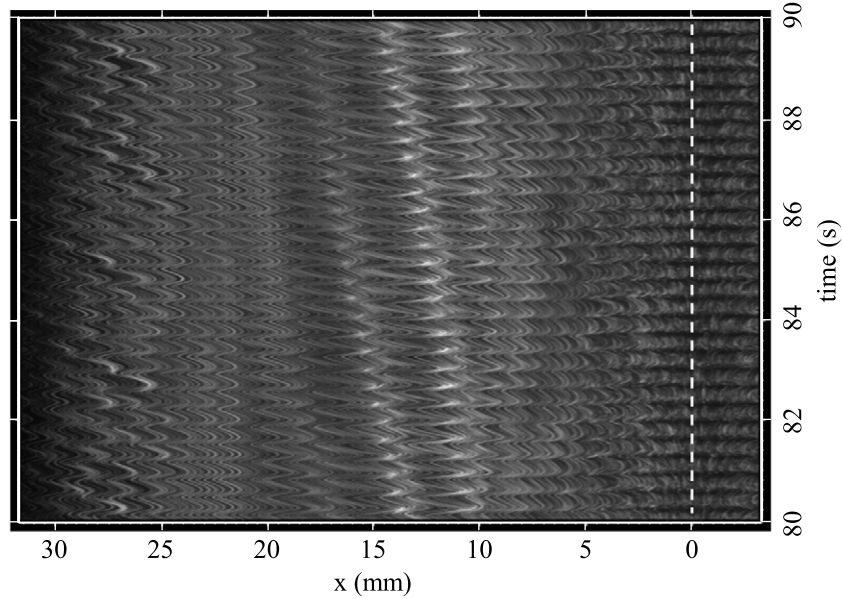


Figure 4. Periodogram showing horizontal oscillations of the cloud. The brighter spikes in the middle (indicating enhanced particle density) are oscillons (see also figure 2) slowly propagating towards the outer edge of the cloud (to the left) at an approximately constant speed of 0.4 mm s^{-1} away from the pulsating void (the horizontal periodic dark stripes to the right). The dashed line indicates the position of the void center. The life-time of the oscillons is $\simeq 20 \text{ s}$, i.e. about 200 damping times. Oscillons are ‘fed’ by the oscillatory energy. The faster edge wave-ridges (see [12]) are also clearly seen at $x > 25 \text{ mm}$.

Fitting a VI-curve (figure 6) obtained from the data shown in figure 5(b) and (c) yields (to the main order) a constant *negative differential conductivity* (NDC; see [22])

$$-dI/dU = 0.41 \pm 0.07 \text{ mA V}^{-1}. \quad (3)$$

Note that sharp current minima (voltage maxima) are apparently linked to the vertical cloud compression, whereas the void opening relates to a weak rise in the current. All this suggests an association with the variation of the discharge capacitance—an ‘electromechanical effect’. In this sense, the complex plasma resembles a *varicap*, a device whose capacitance varies under the applied voltage.

Based on this analogy and using an equivalent circuit model [21], one can show that the expected variation of the rms current is of the order

$$\frac{\delta I}{\langle I \rangle} \simeq -\eta \frac{C_{\text{cloud}}}{C}, \quad \eta = \frac{\omega^2 \tau^2}{1 + \omega^2 \tau^2}, \quad \tau = RC, \quad (4)$$

where R is the discharge resistance, C the discharge capacitance, and C_{cloud} the cloud capacitance. Assuming $\omega\tau \simeq 1$ we estimate $C \simeq 3 \text{ pF}$. Hence, the observed oscillation amplitude would be explained if $C_{\text{cloud}} \simeq 0.4 \text{ pF}$, which is quite reasonable.

The maximal volume of the void considered as an oblate (disc-shaped) spheroid is

$$V = 4 \frac{\pi}{3} c a^2 \simeq 0.077 \text{ cm}^3, \quad (5)$$

where $a \simeq 0.35 \text{ cm}$, and $c \simeq 0.15 \text{ cm}$ are the corresponding semi-axes.

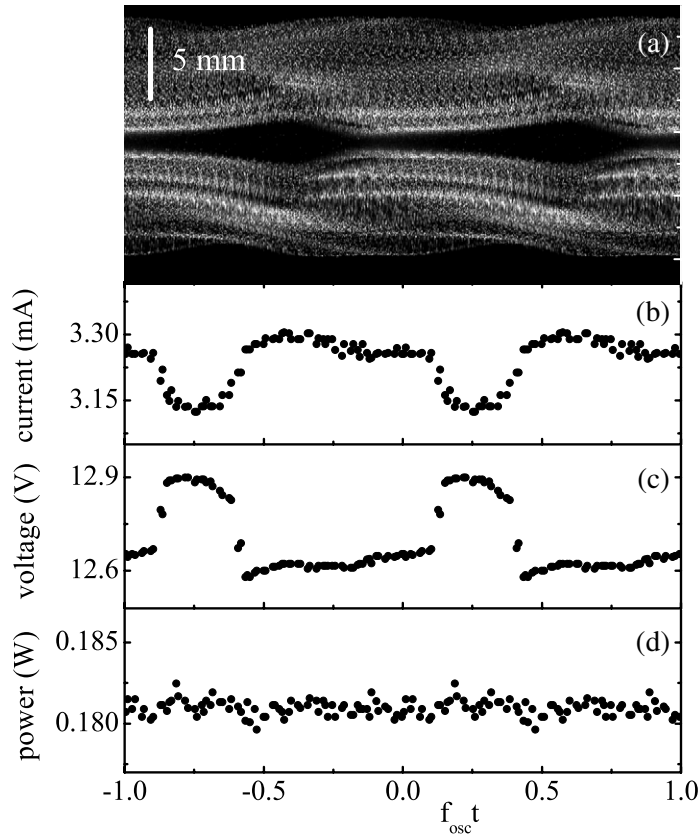


Figure 5. (a) Vertical oscillations of the cloud, (b) the (rms) rf current, (c) rf voltage and (d) applied (forward) rf power versus reduced time ($\equiv f_{osc}t$). Two ‘reconstructed’ oscillation periods are shown. Reconstruction, based on superposition of the data points taken over 20 consecutive periods (phase 3 in figure 1), demonstrates clearly local quasi-periodicity of the discharge electrical signals (periodicity time is limited by slowly drifting oscillons). The lack of any periodicity in the applied power signal is also evident. (The forward power is held constant by a servo control loop inside the rf generator.)

The geometric capacitance of such a spheroid is

$$C = \frac{\sqrt{a^2 - c^2}}{\arccos(c/a)} \simeq 0.3 \text{ pF}. \quad (6)$$

This agrees surprisingly well with the above estimate derived from current variation.

2.4. Plasma parameters

From probe measurements [23] we estimate the plasma parameters as $n_e \sim 10^8 \text{ cm}^{-3}$, $T_e \sim 2\text{--}3 \text{ eV}$. The interparticle separation averaged over the entire cloud area (figure 2) is $\langle \Delta \rangle \simeq 230 \mu\text{m}$. The highest compression occurs at the spikes (figure 4), where the interparticle separation is $\Delta_{\min} = 173 \pm 16 \mu\text{m}$. Outside the spikes compression is less; the interparticle separation is $\langle \Delta \rangle = 300\text{--}350 \mu\text{m}$. At the kinetic level we see that particles are first accelerated

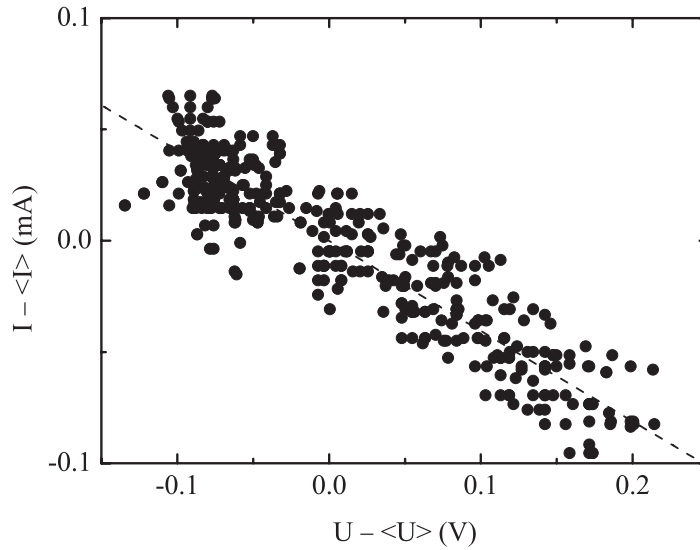


Figure 6. VI-curve of the discharge current and voltage variations indicating *the negative differential conductivity* in the auto-oscillation regime. The dashed line is the rms fit with the negative slope shown in equation (3) in the text.

to high speeds ($v_{\max} = 18.9 \pm 0.4 \text{ mm s}^{-1}$) and then they are decelerated, forming spikes—oscillons, which are clearly seen in figure 2 as vertically elongated constrictions.

The process of periodic capture and release of particles by oscillons is quite similar to that realized inside the dust density wave fronts [8]. Following [8] and using the parameters listed above, we calculated the particle charge $Z_d \simeq 8900$. From [25] it follows $Z_d \sim 9000$.

Thus taking $Z_d \approx 9000$, we can estimate now all other dynamical parameters. For instance, the dust sound speed is $C_{\text{DAW}} \sim 6\text{--}7 \text{ mm s}^{-1}$, and the dust plasma frequency is $f_{\text{dust}} = \omega_{\text{dust}}/2\pi \approx 14\text{--}20 \text{ Hz}$.

The fact that the estimated value of C_{DAW} agrees well with the measured value (see section 2.2) is worth noting. It indicates that the plasma parameters shown above are properly identified.

It is remarkable also from another viewpoint. In the general case the dust acoustic speed depends equally strongly on the particle charge and plasma density [24]. Hence, it is difficult to identify the dominant parameter—either the electron temperature or density—controlling the dynamics. In dense particle clouds if the Havnes parameter $H = Z_d n_d / n_e$ is large, $H > 1$ (exactly the case we deal with), the situation might be different. The dust acoustic speed $C_{\text{DAW}} \propto \sqrt{Z_d(1 + H^{-1})^{-1}}$ is still strongly dependent on the particle charge but only weakly on the electron density. In our case, we estimated $H \approx 2$; thus a $\pm 50\%$ variation in the value of H would give only $\approx 10\%$ variation in C_{DAW} . The particle charge is roughly proportional to the electron temperature. Therefore the value of the dust acoustic speed can be a good measure for the electron temperature.

Finally, let us emphasize again that the values of both parameters Z_d and C_{DAW} are obtained from observations: charge—from the dynamics of oscillons, dust acoustic speed—directly from the fluctuation spectrum.

3. Complex plasma as a dissipative system capable of auto-oscillations

The auto-oscillating cloud of the microparticles is one of the most intriguing phenomena detected in experiments with complex plasmas: the complex plasma gives rise to self-excited macroscopic motions—it sets the paradigm of a dissipative system capable of auto-oscillations. (This stable auto-oscillating complex plasma should not be confused with cyclic spatiotemporal microparticle generations [16], and the *heart-beat instability* [17] studied in detail in dust-forming plasmas). Depending on discharge conditions and plasma parameters, the complex plasma could be kept stable, or excited externally into an oscillatory state, which even in the presence of damping remains autonomically excited.

We associate low-frequency current and voltage self-pulsations, and the accompanying particle oscillations in complex plasmas, with the negative differential conductivity. In this sense, the complex plasma exhibits properties similar to some types of photoconductors [22], semiconductors [26], semi-metals [27], ferroelectric liquid-crystalline films [28], carbon nanotubes [29], nanocrystalline heterostructures [30] and other microelectromechanical systems [31, 32].

The nonlinear dissipative compact formations in the patterns seen in complex plasmas remotely resemble *oscillons*. These standing undulations can be produced on the free surface of a liquid (so-called Faraday's waves [33]), a granular medium (in this case localized excitations can self-organize with possible assembly into 'molecular' and 'crystalline' structures [34]), or nonlinear electrostatic oscillations on a plasma boundary [35]. Oscillons 'feed' from external shaking of the system, and dissipation seems to be inherent for their existence, likewise in our case. There remain still many open questions in explaining the physical mechanism of oscillons.

Streaming ions may act as an activator of the instability in the complex plasma (see e.g. [8]). The formation of a void itself is explained frequently by the counteraction of the confinement force and the ion drag force [18, 36]. Void vibrations in an energized complex plasma are believed to be due to the heart-beat instability, the free energy of which may arise from streaming ions [17]. There are a number of direct observations of the interaction of streaming ions and dust particles [36]–[38].

Since straightforward measurements of flowing ions in complex plasmas are not possible to perform without perturbing the particle cloud structure [39], evidence might be extricated from the direct observations of particle vibrations. There are two possible options:

1. elucidate the long-range character of particle vibrations;
2. decode the patterns of the secondary wavefronts.

Fortunately, both options are realizable as has been proven by the given experiments.

4. Physical aspects of auto-oscillations in complex plasmas

The observations of an auto-oscillating fluid-like system at the individual (atomistic) particle level have revealed a number of different effects/processes [40]–[42]:

1. Complex plasmas are thermodynamically 'open' systems—energy has to be constantly provided to maintain the plasma against recombination;
2. Complex plasmas are (weakly) dissipative due to neutral friction;

3. Complex plasmas exhibit natural frequencies associated with global modes, dust acoustic wave generation, periodic flow patterns, dust plasma frequency, etc as well as characteristic frequencies due to particle confinement;
4. Self-sustained oscillations, ‘feeding’ on the free energy in the system (ultimately the external supply provided by the rf power) and driven by an instability (e.g. caused by ion–particle drift), are therefore not entirely unsuspected;
5. The ‘kinetic details’, colliding particle flows, generation of waves, oscillons, etc presumably all play the role of optimizing energy dissipation and transporting the oscillatory energy out to the edge of the particle cloud.

The surprising (global energy) result appears to be the agreement of our measurements with a simple electromechanical model description, which does not concern itself with the details and speed (rate) of energy transport (dissipation) by the various means at disposal. This suggests that the system automatically ‘adjusts’ these paths of dissipation according to the minimum action principle—without auto-oscillations free energy would build up and the system would have to expand; when it does, energy is released at a rate that could be equal to or larger than that at which it is supplied. External confinement prohibits continuous expansion as a means of equilibration; hence an oscillatory solution would appear to be the most reasonable. Such a scenario requires that the potential energy of the central region be a significant part of the available local energy—the system is clearly not overdamped. That the process occurs in the spatial regime where ion drag and electrostatic forces approximately balance strongly suggests that the free energy of the ion drift is the source of the instability required.

To assure that this scenario is valid, we must do a charge balance, a momentum balance, and an energy balance involving systematic kinetic energy, potential energy, thermal energy and energy carried away by dust acoustic waves and oscillations. A simple estimate, by restricting the considerations to only the main processes, actually is not difficult to get.

4.1. Time and space scales of the momentum transfer

The local consistency of the timescales, for instance, immediately follows from a comparison of the DAW speed (see section 2.4) and the velocity of the void boundary vibrations (see section 2.1). At each half-cycle the void shrinks in size by a factor of $k \simeq 1.5$. The variation of the horizontal (maximal) void semi-axis is of the order of $\delta x = a(1 - k^{-1}) \simeq 0.12$ cm, and the mean boundary velocity is then

$$\langle c \rangle = \Delta x / \Delta t \approx 2 f_{\text{osc}} \delta x \simeq 6.6 \text{ mm s}^{-1}. \quad (7)$$

This is consistent with the above estimated $C_{\text{DAW}} \sim 6\text{--}7 \text{ mm s}^{-1}$ and close to that obtained from the fluctuation spectrum of figure 3. The variation of the void volume, assuming that both axes shorten in the same proportion, can be estimated as

$$\frac{\delta V}{V} = 1 - k^{-3} \simeq 0.7, \quad \delta V \simeq 0.054 \text{ cm}^3. \quad (8)$$

On average the rate of volumetric variation is a bit less than the estimate (7) predicts:

$$\langle c_{\text{vol}} \rangle \approx 2 f_{\text{osc}} \langle R \rangle (1 - k^{-1}) \simeq 5 \text{ mm s}^{-1} \quad (9)$$

but is still of the same order. Here, $\langle R \rangle = \sqrt[3]{\frac{3}{4\pi} V} \simeq 0.26$ cm is the averaged size of the maximal open void.

Propagating periodic density modulations with a wavelength of 1–2 mm are clearly seen, e.g. in figure 5(a). At these scales the DAWs are dominantly responsible for the particle cloud elasticity.

4.2. A charge exchange

Every half-cycle the volume (8) should be cleared out of approximately

$$\delta N_d = \langle n_d \rangle \delta V \simeq 1060 \quad (10)$$

particles. Here, $\langle n_d \rangle = (\frac{4\pi}{3} \langle \Delta \rangle^3)^{-1} \simeq 2 \times 10^4 \text{ cm}^{-3}$ is the dust cloud density (see section 2.4). The total number of electrons stuck to these particles is $Z_d \delta N_d$. This number must be a match for the number of elementary charges that are exchanged while the ‘void-capacitor’ is recharging. According to section 2.2, this number can be estimated as

$$\delta N_{\text{el.ch.}} \approx C_{\text{cloud}} \frac{R \langle I \rangle}{e} \left(\frac{\delta C_{\text{cloud}}}{C_{\text{cloud}}} + \frac{\delta I}{\langle I \rangle} \right). \quad (11)$$

Numerically these two amounts are close, $Z_d \delta N_d \approx \delta N_{\text{el.ch.}} \simeq 10^7$. This is not surprising if the charge balance is fulfilled.

4.3. Momentum and energy balance

In order to examine the global behavior, we investigate the conservation of the horizontal momentum. The momentum of the oscillating particles averaged over the entire oscillation period Δt is naturally equal to zero, $\langle \delta V_x \rangle_{\text{period}} = 0$. Hence, also the impulse of the forces acting at the void interface is zero:

$$\oint_{\Delta t} \delta F_x dt = 0. \quad (12)$$

We separate the acting forces into the ‘electrostatic’ ones δF_{es} , and the ‘ion drag’ forces δF_{id} . Simplifying, we can assume that these counteracting forces play a role dominantly only in one of the consecutive half-cycles. Then the relationship (12) can be approximately rewritten as

$$(\langle \delta F_{\text{es}} \rangle - \langle \delta F_{\text{id}} \rangle) \Delta t / 2 = 0. \quad (13)$$

The force δF_{id} is due to the variation of the ion drift (compared to the global ambipolar ion drift component always directed outwards, i.e. towards the discharge chamber walls, see figure 2). For our parameter set (see section 2.4) it can be estimated from the relationship (see equation (11) of [43]; the relationship is valid in the limiting case of small ion drift velocities):

$$\delta F_{\text{id}} \simeq 0.02 M_d g \frac{\delta u_i}{v_{T_i}}, \quad (14)$$

if $M_T = \frac{\delta u_i}{v_{T_i}}$ the ‘thermal Mach number’ of the drift velocity fluctuation is known. To get a sense of how big M_T is, we note that far away from the void boundary where the particles move at an approximately constant speed $|v| \simeq 4\text{--}5 \text{ mm s}^{-1}$ (figure 7), the force (14) should be compensated for by the friction force $\delta F_{\text{fr}} \equiv M_d \gamma_{\text{damp}} \delta v$. This balance yields the magnitude of the ion drift velocity fluctuation:

$$\frac{\delta u_i}{v_{T_i}} = 0.2\text{--}0.3, \quad (15)$$

which is quite reasonable.

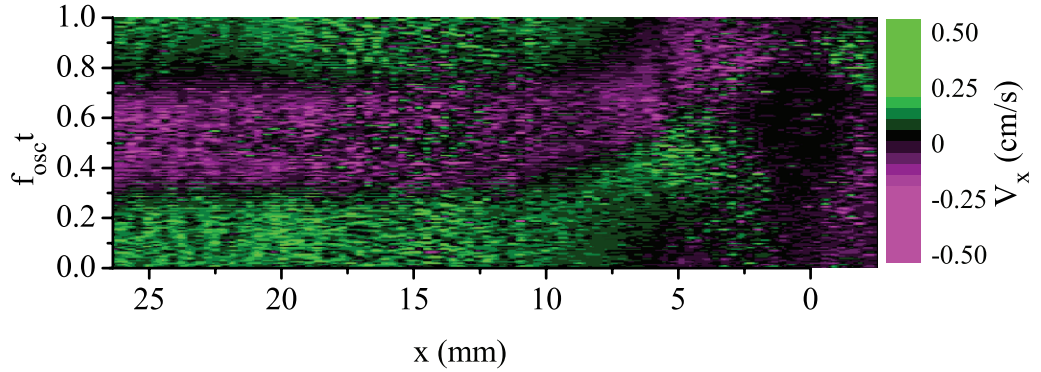


Figure 7. Time–space map of the horizontal velocity of the particles. Particle positions are identified, their velocities are calculated in consecutive frames, and shown color-coded, using a narrow horizontal slab $1.2 \times 30 \text{ mm}^2$ crossing the void center. The void is clearly seen to the right as the darker region with (conventionally) zero velocity. It should not be confused with *the stagnation zone* located at $x \sim 5 \text{ mm}$ on the first and last quarters of the period, and at the middle of the period. The enhanced counter streaming advancing and retreating particle fluxes are also clearly seen there. Note that outside this region at $x > 7 \text{ mm}$ the incoming and outgoing particle fluxes are formed practically simultaneously at all distances, indicating the presence of the ‘latent’ ion drift activating motion of the particles. To reduce the stochastic noise, the data points are taken and smoothed over 20 consecutive periods (the same as in figure 5).

Next, after introducing the electrostatic force by the relationship

$$\delta F_{\text{es}} = Z_d e E, \quad E \approx -\frac{\delta \varphi}{\delta x}, \quad (16)$$

the force balance (13) allows us to estimate:

$$\delta \varphi \approx 0.03 \text{ V}. \quad (17)$$

This result is in fairly good agreement with that measured in [36].

Finally, the energy balance written in the form:

$$W_{\text{ext}} = \Delta W + 2\langle W_{\text{kin}} \rangle \gamma_{\text{damp}} \Delta t, \quad W = W_{\text{pot}} + W_{\text{kin}}. \quad (18)$$

yields the work W_{ext} of the external forces needed to compensate for frictional losses. Here $W_{\text{pot}} = Z_d e \delta N_d \delta \varphi$ is the electrostatic potential energy, W_{kin} is the kinetic energy, and ΔW is the variation of the total energy during the time of an oscillation Δt .

In the beginning of every expansion cycle the particles first accelerate, acquiring kinetic energy, and then decelerate. Let us adopt a simple spherical model of the void of size a . To consider the last stage, we put for the particles’ speed a distribution

$$v = v_m \frac{a - r}{a}, \quad 0 < r \leq a, \quad (19)$$

where v_m is the maximal particle velocity; particles stop at $r = a$. Initially the particle density is constant, $n_d = \delta N_d / V$, $V = \frac{4}{3} \pi a^3$; next, at expansion it is $\sim \delta(r - a)$. The maximal kinetic

energy ‘to clear the void’ is then

$$W_{\text{kin}} = \int_0^a \frac{1}{2} M_d n_d v^2 4\pi r^2 dr = \frac{1}{20} M_d v_m^2 \delta N_d. \quad (20)$$

At $v_m \sim 5 \text{ mm s}^{-1}$, we have $W_{\text{kin}} \sim 5 \text{ keV}$, that is, roughly 5 eV per particle.

The directed kinetic energy dissipation rate in every expansion–contraction cycle is $\dot{W}_{\text{kin}} = 2W_{\text{kin}} f_{\text{osc}} \sim 30 \text{ keV s}^{-1}$. This is an elastic, ‘recoverable’, part of dissipation: The kinetic energy is returned to the particles by work done by potential forces. The average inelastic (frictional) energy loss is defined by the relationship

$$\langle \dot{W} \rangle_{\text{fr}} = 2\gamma_{\text{damp}} \langle W_{\text{kin}} \rangle, \quad (21)$$

and is of the same order as \dot{W}_{kin} .

In contrast, the oscillon-driving mechanism must be much more powerful because the energy dissipation rate through outgoing oscillons is higher, of the order of $\langle \dot{W} \rangle_{\text{oscillon}} \sim 100\text{--}200 \text{ keV s}^{-1}$. This can easily be verified making use of the parameters listed above (see sections 2.2 and 2.4) and noting that the fully developed oscillon is a circular belt-shaped wave of horizontal width $\approx 0.5\text{--}1 \text{ mm}$ and transverse cross-section $S_{\text{oscillon}} = (2\pi R \times H)_{\text{oscillon}} \approx 5\text{--}7 \text{ cm}^2$.

4.4. A trigger mechanism for inner oscillations

According to the general theory of nonlinear oscillations, the auto-oscillation patterns arise in dynamical systems with feedback. In order to clarify the mechanism of feedback in the complex plasma we experimented with, it is necessary to have an idea of the distribution and evolution of internal and external fields controlling particle motion. The observed behavior may be due to a different (collective) physical process that needs a different treatment. In the experimental studies discussed above such detailed measurements could not be made and for that reason the creation of a rigorous model is difficult. There is one common point, however. A possible indication of such a feedback is the ‘intrinsic non-Hamiltonianity’ of complex plasma dynamics [44, 45]. There are two aspects worth discussing: This type of feedback based on charge gradients has been used in [45] to explain self-excitations of some simple systems—a few oscillating particles, and chains of charged particles. It was mentioned that the complexity of the system is not an obstacle for auto-oscillations. Furthermore, often space- and time-dependent particle charges are considered as an inherent attribute of many complex plasmas, see e.g. [46] and references therein.

Another possibility for particles to gain energy originates from the classical tunneling effect [25]. Moving particles may slide through a cloud of similar particles, elastically deforming the cloud as they slide through it. For instance, at expansion as the central particles are pushed away outwards, forming a void, they are forced to penetrate into the rest of the particle cloud, which is still immobile. When a particle passes through the layers of a cloud, its charge changes, helping penetration. For particles of the same size possible charge variation through the ‘charge sharing process’ is $(\delta Z/Z)_{\text{max}} = 1/4$ on maximum [25]. In our case, the charge variation needed to compensate for frictional losses (21) is 3–4 times less than this limit:

$$\frac{\delta Z_d}{Z_d} = \frac{\langle \dot{W} \rangle_{\text{fr}}}{Z_d |e| \delta \varphi \delta N_d f_{\text{osc}}} \sim 0.07 < \left(\frac{\delta Z}{Z} \right)_{\text{max}}, \quad (22)$$

so that this is a promising way to gain the energy.

4.5. A driving mechanism for outer oscillations

In the dynamics of auto-oscillations, not only short time and space scales of DAWs are important, but also the global ones of the size of the cloud. At distances further from the void, starting from $\sim 5\text{--}7$ mm and approximately up to the edge of the cloud, the particles are seen to move as if they acquire momentum at all positions simultaneously (see figure 7). Apparently the ‘wave exciting agent’ (that is, the plasma ions), sharing the momentum with particles, must be much lighter compared to the particles themselves. At these distances the ion collection effect appears to be more important (see section 2.2). This highlights once again the crucial role of the ion drift as the source of the instability.

Undoubtedly the oscillations in the outer part of the cloud are induced by fluctuating central charges (figure 2). But what is the physics explaining why these oscillations form such a kind of ‘supersonic’ pattern?

The explanation of ‘simultaneous’ excitation is indeed simple: the particles behave this way because they are forced to by *the breathing mode* [12]. Compared to the dust acoustic mode, this one is a fast-phase mode: $C_{\text{bm}} = f_{\text{osc}}\Delta L = 70\text{--}80 \text{ mm s}^{-1} \gg C_{\text{DAW}} = 6\text{--}7 \text{ mm s}^{-1}$. (Here $\Delta L \approx D/2 = 25\text{--}30$ mm is approximately half the size of the cloud.) This naturally explains the observed simultaneous excitation: the cloud disturbance appears to be transmitted supersonically with respect to the speed of the dust acoustic waves.

Next, an important issue is to explain the value of the frequency (1) involved in auto-oscillations. This frequency is difficult to calculate rigorously. However, there are several possible ways to estimate it: it is well known that the breathing mode is determined primarily by the confinement conditions, that is, by the strength of the electric field caging the cloud. As a first step, assuming [11] that the radial voltage drop $\delta U_r \sim U$ (see (2)), we estimate the radial component of the electric field strength, and then the confinement parameter as (M_d is the mass of the dust particle)

$$f_{\text{conf}} \sim \frac{1}{\pi D} \sqrt{\frac{2Z_d|e|\delta U_r}{M_d}} \simeq 1.4 \text{ Hz}, \quad (23)$$

this explaining the breathing mode oscillation frequency. (According to [47], for the breathing mode it should be $f_{\text{bm}} \simeq 2f_{\text{conf}} \simeq 2.8$ Hz in good agreement with the experimentally observed value (1)).

It is worth noting that a more detailed consideration based on the assumptions of the ambipolar model [48] confirms (23). It follows that

$$f_{\text{conf}} \sim \frac{1}{\pi D} \sqrt{\frac{2Z_d|e|\delta U_{\text{amb}}}{M_d}}, \quad \delta U_{\text{amb}} \simeq \left(\frac{1}{2}D\right)^2 \text{div } \mathbf{E}_{\text{amb}} \simeq \xi^2 \frac{T_e}{|e|}. \quad (24)$$

Here $\xi \simeq 2.405$ is the first root of the zeroth-order Bessel function, $J_0(\xi) = 0$. Numerically $\delta U_{\text{amb}} \approx U$, and this frequency estimate agrees well with (23).

Note also that a reasonable estimate of the frequency can be obtained by considering the behavior of the particles at the very edge of the cloud. The key point is that there, at the edge, the quasi-equilibria are stable because of the balance between confinement and repulsion:

$$E_{\text{conf}} = \delta E_{\text{rep}}^{(1)} n_{\text{eff}}, \quad (25)$$

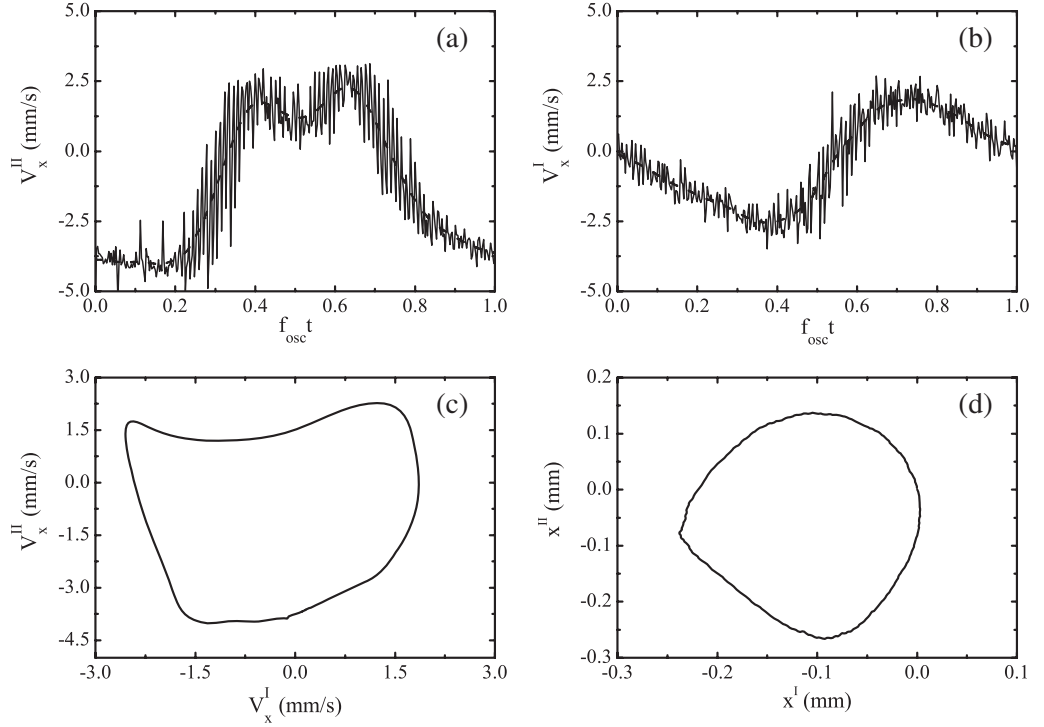


Figure 8. Averaged velocities $v_x^{I,II}$ (a, b), kinematic (c) and spatial (d) mutual phase portraits for inner (I) and outer (II) particles, oscillating to the left of the void boundary (see figure 2). x^I and x^{II} are the ‘centers of mass’ of the inner ($2.5 \text{ mm} < x < 7.5 \text{ mm}$) and outer ($7.5 \text{ mm} < x < 25 \text{ mm}$) particles. In both cases the width of the horizontal slab (centered at the height of the void center) was $\Delta y = 4.4 \text{ mm}$. The inner and outer oscillations are evidently auto-correlated, forming a type I attractor (as classified in [45]).

$$\delta E_{\text{rep}}^{(1)} \approx \frac{Z_d |e|}{\langle \Delta \rangle^2} \left(1 + \frac{\langle \Delta \rangle}{\lambda_{\text{scr}}} \right) \exp \left(-\frac{\langle \Delta \rangle}{\lambda_{\text{scr}}} \right), \quad (26)$$

$$\delta U_{\text{conf}} \sim \frac{1}{2} D E_{\text{conf}}, \quad (27)$$

where λ_{scr} is the screening length, $\delta E_{\text{rep}}^{(1)}$ is the strength of repulsion (per particle), and $\delta E_{\text{rep}}^{(1)} n_{\text{eff}}$ is the total repulsion exerted on a given edge particle by the effective nearest neighbors n_{eff} , pushing the particle out of the cloud. From elementary calculations it follows that $\delta U_{\text{conf}} / n_{\text{eff}} \simeq 2\text{--}3 \text{ V}$. Hence, to obtain the expected $\delta U_{\text{conf}} \approx U \approx 13 \text{ V}$, one needs 5–6 associated neighbors. This number has to be reduced roughly by a factor 2 when the ion drag force is included in the balance.

The time–space pattern formed by the oscillating particles has a rather complicated structure (see figure 2 and 7). To simplify the analysis, we divided the cloud’s cross-section by two (not equal) subparts: the inner (I) ($2.5 \text{ mm} < x < 7.5 \text{ mm}$) and the outer (II) ($7.5 \text{ mm} < x < 25 \text{ mm}$) regions (in both cases the width of the horizontal slab was chosen as specified in the caption to figure 8). We explored the particle oscillations in these regions separately and found a surprisingly clear auto-correlation as shown in figure 8. For the particles oscillating closer to

the void, the mean kinetic energy is $\langle W_{\text{kin}}^{\text{I}} \rangle = 5.1 \pm 0.3$ eV, which agrees very well with that predicted by the model (20), whereas $\langle W_{\text{kin}}^{\text{II}} \rangle = 15.3 \pm 0.6$ eV for the particles inside the outer region.

5. Conclusion

The origin of the proposed electromechanical effect could be due to the cloud stretching, multiplication or selective harmonic amplification of coupled oscillations of the particles and the electrical circuitry feeding the discharge. In the case studied here, it is a self-sustained low-frequency resonant oscillator. We conclude that the self-excitation leading to the regular repeatable constrictions of the void in the particle cloud is due to the free energy in plasma ions drifting relative to the microparticles.

Note finally that intense shaking due to the auto-oscillating breathing mode is the necessary condition of the oscillon excitations observed in our wave patterns. Hereby, the complex plasma sets a new ‘kinetically resolved’ paradigm to a variety of ‘vibro-excited’ oscillons in many other media [33]–[35].

Acknowledgments

We acknowledge valuable discussions with P Huber, U Konopka and all members of the PK-3 Plus team. This work was supported by DLR/BMWi grant no. 50WP0203 and by RFBR grant no. 08-02-00444-a.

References

- [1] Pierce A D 1989 *Acoustics: an introduction to its Physical Principles and Applications* (New York: Acoustical Society of America)
- [2] Rowley C W *et al* 2002 *J. Fluid Mech.* **455** 315
- [3] Garnier N and Chiffaudel A 2001 *Phys. Rev. Lett.* **86** 75
- [4] Zuev L B *et al* 2001 *Russ. Phys. J.* **44** 169
- [5] Sauermann G *et al* 2001 *Phys. Rev. E* **64** 031305
- [6] Kovalchuk V I *et al* 1999 *Phys. Rev. E* **60** 2029
- [7] Strümpel C *et al* 2000 *Phys. Rev. E* **62** 4889
- [8] Schwabe M *et al* 2007 *Phys. Rev. Lett.* **99** 095002
- [9] Zierep J and Oertel H (ed) 1982 *Convective Transport and Instability Phenomena* (Braun: Karlsruhe)
- [10] Koschmieder E L 1993 *Benard Cells and Taylor Vortices* (Cambridge: Cambridge University Press)
- [11] Thomas H M *et al* 2008 *New J. Phys.* **10** 033036
- [12] Schwabe M *et al* 2008 *New J. Phys.* **10** 033037
- [13] Piel A *et al* 2006 *Phys. Rev. Lett.* **97** 205009
- [14] Morfill G E *et al* 1999 *Phys. Rev. Lett.* **83** 1598
- [15] Lipaev A M *et al* 2007 *Phys. Rev. Lett.* **98** 265006
- [16] Cavarroc M *et al* 2008 *Phys. Rev. Lett.* **100** 045001
- [17] Mikikian M *et al* 2007 *New J. Phys.* **9** 268
- [18] Samsonov D and Goree J 1999 *Phys. Rev. E* **59** 1047
- [19] Samsonov D *et al* 2001 *Phys. Rev. E* **63** 025401
- [20] Šijačić D D *et al* 2004 *Phys. Rev. E* **70** 056220
- [21] Godyak V A *et al* 1991 *IEEE Trans. Plasma Sci.* **19** 660

- [22] Hoffman H F 1975 *Phys. Status Solidi a* **31** 171
- [23] Klindworth M *et al* 2007 *Rev. Sci. Instrum.* **78** 033502
- [24] Rao N N, Shukla P K and Yu M Y 1990 *Planet. Space Sci.* **38** 543
- [25] Morfill G E, Konopka U, Kretschmer M, Rubin-Zuzic M, Thomas H M, Zhdanov S K and Tsytovich V 2006 *New J. Phys.* **8** 7
- [26] Esaki L and Tsu R 1970 *IBM J. Res. Dev.* **14** 61
- [27] Upit G P *et al* 1966 *Phys. Status Solidi* **15** 617
- [28] Yablonskii S V *et al* 2001 *J. Exp. Theor. Phys.* **93** 94
- [29] Hall A R *et al* 2007 *Nat. Nanotechnol.* **2** 413
- [30] Chen J *et al* 2007 *Nanotechnology* **18** 015203
- [31] Sung S *et al* 2003 *J. Micromech. Microeng.* **13** 246
- [32] Hossein-Zadeh M *et al* 2006 *Phys. Rev. A* **74** 023813
- [33] Faraday M 1831 *Phil. Trans. R. Soc. Lond. A* **52** 299
- [34] Umbanhowar P B *et al* 1996 *Nature* **382** 793
- [35] Stenflo L and Yu M Y 1996 *Nature* **384** 224
- [36] Kretschmer M *et al* 2005 *Phys. Rev. E* **71** 056401
- [37] Steinberg V *et al* 2001 *Phys. Rev. Lett.* **86** 4540
- [38] Melzer A *et al* 1999 *Phys. Rev. Lett.* **83** 3194
- [39] Klindworth M *et al* 2006 *J. Phys. D* **39** 1095
- [40] Shukla P K and Mamun A A 2002 *Introduction to Dusty Plasma Physics* (Bristol: Institute of Physics Publishing)
- [41] Fortov V E, Ivlev A V, Khrapak S A, Khrapak A G and Morfill G E 2005 *Phys. Rep.* **421** 1
- [42] Morfill G E and Ivlev A V 2009 *Rev. Mod. Phys.* **81** 1353
- [43] Ivlev A V, Zhdanov S K, Khrapak S A and Morfill G E 2005 *Phys. Rev. E* **71** 016405
- [44] Vulina O, Nefedov A P, Petrov O F and Fortov V E 2000 *J. Exp. Theor. Phys.* **91** 1147
- [45] Zhdanov S K, Ivlev A V and Morfill G E 2005 *Phys. Plasmas* **12** 072312
- [46] Losseva T V, Popel S I, Yu M Y and Ma J X 2007 *Phys. Rev. E* **75** 046403
- [47] Sheridan T E 2005 *Phys. Rev. E* **72** 026405
- [48] Lieberman M A and Lichtenberg A J 2005 *Principles of Plasma Discharges and Material Processing* 2nd edn (New York: Wiley)

7.5 *Europhysics Letters (EPL): Shear flow instability at the interface among two streams of a highly*

7.5 Europhysics Letters (EPL): Shear flow instability at the interface among two streams of a highly dissipative complex plasma

Shear flow instability at the interface among two streams of a highly dissipative complex plasma

This article has been downloaded from IOPscience. Please scroll down to see the full text article.

2011 EPL 96 15001

(<http://iopscience.iop.org/0295-5075/96/1/15001>)

View [the table of contents for this issue](#), or go to the [journal homepage](#) for more

Download details:

IP Address: 130.183.136.86

The article was downloaded on 10/10/2011 at 12:39

Please note that [terms and conditions apply](#).

Shear flow instability at the interface among two streams of a highly dissipative complex plasma

R. HEIDEMANN^(a), S. ZHDANOV, K. R. SÜTTERLIN, H. M. THOMAS and G. E. MORFILL

Max-Planck-Institut für extraterrestrische Physik - 85741 Garching, Germany, EU

received 18 July 2011; accepted in final form 25 August 2011
published online 22 September 2011

PACS 52.27.Lw – Dusty or complex plasmas; plasma crystals
PACS 47.15.Fe – Stability of laminar flows
PACS 47.20.Ma – Interfacial instabilities (*e.g.*, Rayleigh-Taylor)

Abstract – The shear instability was experimentally studied in a highly dissipative cloud of complex plasma. The cloud of microparticles formed a toroidal vortex with poloidal flow and a stagnation zone in the center. The flow was studied at the kinetic level by resolving the trajectories of the individual microparticles. Hydrodynamic quantities such as flow velocity, vorticity and enstrophy density were determined. The effects of interfacial surface tension were explored. It was found that the two-stream interface between flow and stagnation zone breaks down into a well-developed multi-stream network due to Rayleigh-Taylor-type perturbations.

Copyright © EPLA, 2011

Introduction. – A complex plasma is a weakly ionized gas containing electrons, ions and small macroscopic particles [1,2]. In a complex-plasma microparticles are trapped and charged by a low-temperature plasma and form a one-component liquid. That offers a unique possibility to study fluid dynamics at the most fundamental kinetic level by resolving the trajectories of the individual microparticles. This makes complex plasma an ideal model system for nano fluids [3–5] to study, *e.g.*, dynamical processes [6–9], phase transitions [10–13] and transport processes [14–16], all at the fundamental atomistic level. In this study the dynamics of the particles at an interface between a flowing and a resting complex plasma is discussed. Highly resolved studies of streaming instabilities and circulations in complex plasmas at the kinetic level are still a challenging issue [17,18]. We performed our experiments with radio frequency (rf) discharge plasmas and monodisperse spherical microparticles. The topology of the flow was organized similarly to a convection cell with a toroidal shape. In this work we study the breakup of an interface between resting and flowing particles. An instability was triggered behind an obstacle along the interface between streaming particles and resting particles in the center of the torus. This interface instability was observed at the kinetic level and connected to a hydrodynamic description by calculating macroscopic quantities like rotation, enstrophy and surface tension. From the trajectories of individual

particles we reconstructed the flow pattern and estimated the complex-plasma parameters. The possible origin of the instability is discussed.

Experiment conditions. – The experiments were performed in a modified version of the PKE-Nefedov setup [19]. The discharge chamber contains a pair of parallel plate electrodes with a diameter of 6 cm surrounded by a 1 cm wide grounded guard ring. The electrodes are powered by a 13.56 MHz rf voltage applied to both electrodes symmetrically in push-pull mode. Gas is introduced in the chamber by a flow controller. The pressure in the chamber is regulated by a baratron with accuracy of 0.5 Pa. After the plasma is ignited the microparticles are injected into the chamber. The particles form a cloud inside the bulk of the discharge and can be easily visualized by laser light illumination and a video camera.

This setup allows us to perform experiments in a wide range of parameters (gas pressure, discharge power, particle number density, temperature gradient, etc.). For this study it was particularly important to optimize the experiment conditions to enable an intense stationary rotating particle flux.

For this purpose we used argon gas at a pressure of 55 Pa. The input RF Power was 1 W. Melamine-formaldehyde particles with a diameter of 1.28 μm were injected into the plasma. Additionally, thermophoresis was used to compensate for gravity. For this purpose, a temperature gradient of 320 $\frac{\text{K}}{\text{m}}$ was applied.

^(a)E-mail: Heidemann@mpe.mpg.de

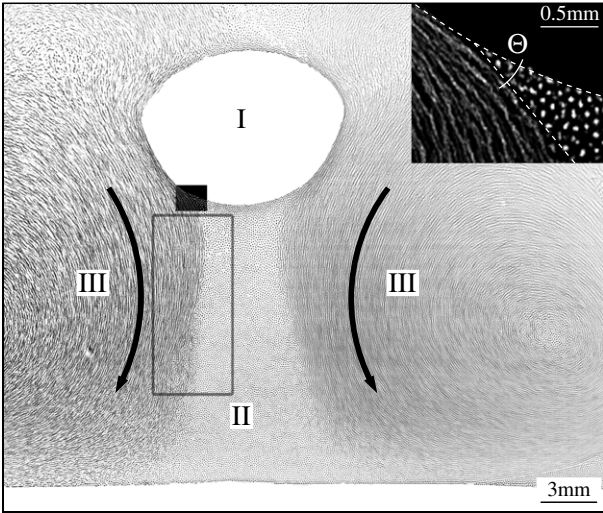


Fig. 1: A $120\ \mu\text{m}$ thick cross-section through the microparticle cloud. The whole cloud consists of about $25 \cdot 10^6$ particles. The illuminating laser light comes from the right. The main elements are clearly recognizable: the void (I), the stagnation zone (II) below the void, and the vortex (III). A superposition of 20 images is shown to emphasize the particle trajectories. The black arrows indicate the direction of the particle flux. The region of interest used in the analysis is indicated by a rectangle. The insert shows the contact angle $\Theta = 20^\circ \pm 5^\circ$ between the two fluids (inverted region).

A $120\ \mu\text{m}$ thick slice of the complex plasma was illuminated by a green (532 nm) laser diode. The light scattered by the particles was recorded with a CCD camera at a frame rate of 90 Hz with a resolution of $13.6\ \mu\text{m}$ ($15.6\ \mu\text{m}$) in horizontal (vertical) direction.

Tracking. – To study the cloud dynamics we determine the particle positions in every frame ($\mathbf{r}_i = x_i \mathbf{e}_x + y_i \mathbf{e}_y$, $i = 1, \dots, N$, where N is the number of particles, $\mathbf{e}_{x,y}$ are the unit vectors). A Gauss fitting method was used for the particle position calculation. This procedure allows to avoid pixel locking that can occur in other methods [20]. Then we track single particles in consecutive frames to form trajectories (see fig. 2). The resting (streaming) particles were tracked for an average of 41 (28) frames. From the particle trajectories we extract velocities (\mathbf{v}_i) accurate to the order of Δt^2 , $\Delta t = 1/90\ \text{s}$.

High-quality tracking data allowed us to derive higher derivatives such as the divergence and vorticity of the velocity field. For the calculation of vorticity and divergence from the discrete particle trajectories the following algorithm was developed: First, Delaunay triangulation was used to obtain the nearest-neighbor vectors ($\mathbf{r}_{i,j} = \mathbf{r}_j - \mathbf{r}_i$, where $j = 1, \dots, nn_i$, nn_i is the number of the nearest neighbors). Second, to calculate the divergence, the projections $\frac{\mathbf{r}_{i,j} \cdot \mathbf{v}_{i,j}}{r_{i,j}}$ of the relative velocities $\mathbf{v}_{i,j} = \mathbf{v}_j - \mathbf{v}_i$ on the nearest-neighbor vectors were calculated and divided by the distance $r_{i,j} = |\mathbf{r}_{i,j}|$, resulting in $d_{i,j} = \frac{\mathbf{r}_{i,j} \cdot \mathbf{v}_{i,j}}{r_{i,j}^2}$. The vorticity was

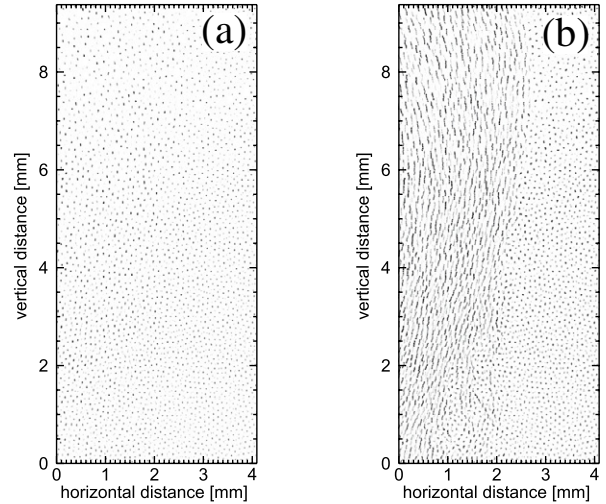


Fig. 2: The spatial distribution of the microparticles at the interface. (a) A single image with exposure time $\Delta t = 1/90\ \text{s}$. (b) Four superimposed consecutive images: the elongated particle tracks in the left part indicate the flow. The mean flow velocity is $V = 3.3 \pm 0.5\ \text{mm/s}$. The average particle distance is $\Delta_r = 109\ \mu\text{m}$ for the resting particles (right), while it is $\Delta_s = 113\ \mu\text{m}$ for the streaming particles (left).

calculated analogously: The projections $c_{i,j} = \frac{\mathbf{r}_{i,j}^\perp \cdot \mathbf{v}_{i,j}}{r_{i,j}^2}$ were performed onto the vectors $\mathbf{r}_{i,j}^\perp = \mathbf{e}_z \times \mathbf{r}_{i,j}$ orthogonal to $\mathbf{r}_{i,j}$, here $\mathbf{e}_z = \mathbf{e}_x \times \mathbf{e}_y$. Note that with this definition vorticity is positive for counter-clockwise rotation. Third, the obtained results were averaged over all neighbors, resulting in

$$(\text{div } \mathbf{v})_i = \frac{1}{nn_i} \sum_{j=1}^{nn_i} d_{i,j}, \quad (1)$$

$$\Omega_i = \mathbf{e}_z \cdot (\text{curl } \mathbf{v})_i = \frac{1}{nn_i} \sum_{j=1}^{nn_i} c_{i,j}. \quad (2)$$

To validate the values of the discrete $(\text{div } \mathbf{v})_i$ and Ω_i we also calculated divergence and vorticity using a regular gridded velocity field ($\mathbf{v}_{k,l}$) in the cell (k,l) via binning. Binning of the discrete results (1), (2) with the same regular grid shows very good agreement.

The discrete algorithm gives an optimal spatial resolution. This is important because the flow interface is narrow with a width of the order of the inter-particle separation.

Topology of the particle cloud. – The particle cloud in our experiment is almost cylindrical with slightly rounded edges. Its height and radius are approximately 20 mm. Figure 1 shows a cross-section through the particle cloud. On the symmetry axis of the cloud slightly above the center there is a “void”, a particle free region, with a radius $\approx 5\ \text{mm}$. In the outer region of the cloud convecting particles form a toroidal vortex with poloidal flow. The angular velocity of convection $\Omega_c \approx 0.3\ \text{s}^{-1}$. This makes up the largest part of the cloud. The “circulation

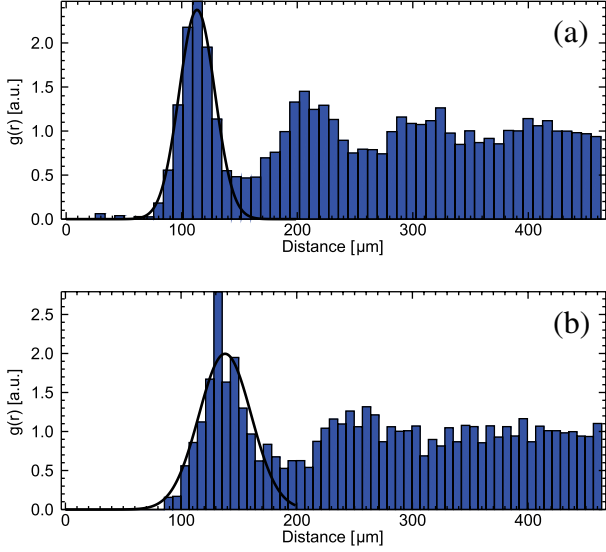


Fig. 3: (Colour on-line) The pair correlation function $g(r)$ (a) of the resting particles, and (b) of the streaming particles. The black lines show the Gauss fit to the first peak of $g(r)$. The positions of the peaks are: (a) $a_r = 113 \pm 4 \mu\text{m}$ and (b) $a_s = 138 \pm 5 \mu\text{m}$. The resting part of the cloud is denser $\frac{n_r}{n_s} \simeq 1.8$.

dynamo” [18] that drives convection in complex plasmas is one of the outstanding problems. In our case it seems natural to consider creep-induced dust convection [21–23]. The void provides an obstacle to the poloidal flow. In the wake under the void a stagnation zone of resting particles is formed. The cloud inside the stagnation zone is approximately two times denser compared to the vortex region, see fig. 3. The bottom of the cloud is terminated by the discharge sheath.

We study the interface among the poloidal stream and the “stagnation zone”. The interface is characterized by a change in the number density and a high angular velocity gradient (see figs. 2 and 4). The mean velocity of the streaming particles at the interface is 3.3 mm/s. The mean poloidal radius of the vortex flow $\approx 11.5 \pm 1$ mm. The interface is very sharp and stable behind the obstacle. Further downstream the interface is unstable and the width of the mixing layer between the streaming and the resting particles grows exponentially.

Particle kinetics. –

Characterization of the fluids. The differences of the streaming (s) and the resting (r) fluid are in the flow velocity (\mathbf{v}), density (n) and particle flux (\mathbf{j}). The main difference of the two fluids at the interface is their average vertical velocity $\langle v_y \rangle$ which is $\langle v_y \rangle_s = -3.3 \pm 0.5$ mm/s for the streaming particle and $\langle v_y \rangle_r = 0.05 \pm 0.1$ mm/s for the resting particles.

The pair correlation function $g(r)$ gives a more detailed picture of the particle distributions (cf. fig. 3). The lattice spacing, derived from a Gauss fit of the first peak, is

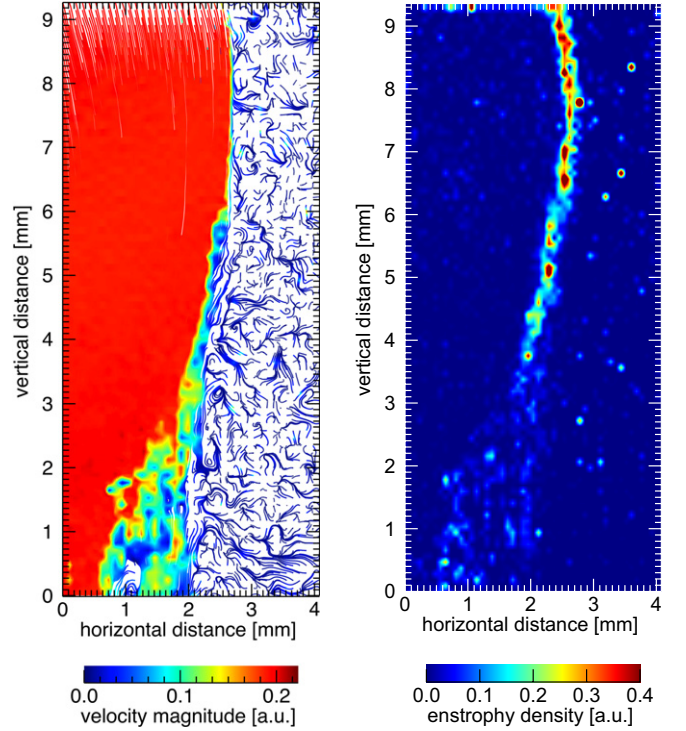


Fig. 4: (Colour on-line) Left panel: the interface and the mixing layer between streaming particles (to the left) and the resting particles (to the right). The flow is visibly laminar from the top down to a height of 6 mm. At $6 \text{ mm} > y > 3.5 \text{ mm}$ the particles start to mix, increasing the width of the interface. At $y < 3.5 \text{ mm}$ the width increases exponentially and chains of particles inter-penetrate. Right panel: the enstrophy density pattern. The averaged rotation energy density apparently peaks up along the laminar interface, then visibly volatilizes from the point where the flow becomes unstable ($y = 3.5 \text{ mm}$). The picture was obtained by averaging over 40 frames.

$a_r = 113 \pm 4 \mu\text{m}$ for the resting and $a_s = 138 \pm 5 \mu\text{m}$ for the streaming fluid. The more distinct second and third peak give a hint for a more ordered structure in the resting particles. The full width at half-maximum of the first peak of $g(r)$, $\sigma_r = 36 \pm 11 \mu\text{m}$ and $\sigma_s = 53 \pm 12 \mu\text{m}$, is also indicating a more disordered state of the streaming particles. The calculated number densities are $n_r = 1.3 \cdot 10^6 \text{ cm}^{-3}$ and $n_s = 0.73 \cdot 10^6 \text{ cm}^{-3}$. The particle flux of the poloidal stream is $j_s = 0.24 \cdot 10^6 \text{ cm}^{-2} \text{ s}^{-1}$.

Interface. The interface between the two fluids develops after the streaming fluid detaches from the void. At the beginning of the interface the flow is laminar with almost no mixing of the two fluids. Here the thickness of the interface is only one interparticle separation (cf. fig. 2). Therefore, the interface structure cannot be described hydrodynamically. A kinetic description is necessary.

Contact angle. The strong separation of the two fluids indicates a surface tension at the interface. The surface tension also manifests itself in the appearance of the contact angle $\Theta = 20^\circ \pm 5^\circ$ where the stream detaches

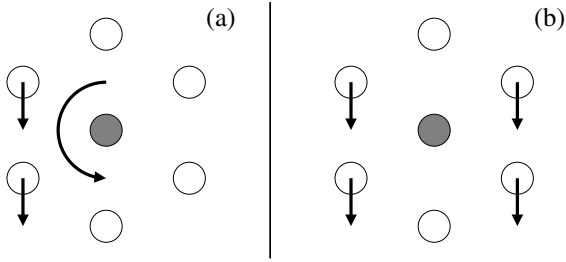


Fig. 5: Mechanism of the volatilization of enstrophy density in the mixing layer. (a) A local point at the interface (filled circle) has a high vorticity and therefore also a high enstrophy value because of the tangential motion of the next neighbors when the streams are separated. (b) When the flows mix up and streaming particles penetrate the region of the resting particles, the vorticity goes down. The straight arrows indicate the relative velocity of the particles, the curved arrow indicates the vorticity.

from the void (cf. insert in fig. 1). Using the Young equation we can derive the relation between the surface tension of the two fluids α_r and α_s ,

$$\cos \Theta = \frac{\alpha_r}{\alpha_s} \approx 0.94. \quad (3)$$

This is valid of course only approximately because we neglected the influence of the constant particles stream.

Development of the instability. The laminar part of the interface is approximately $60a_s = 7$ mm long (cf. fig. 1). At a certain point downstream from the void, the particles start to interpenetrate and the laminar interface breaks down. On the onset of the instability the streamlines start to cross the boundary between the fluids as can be seen in fig. 4 (left panel).

To characterize the particle dynamics we use the enstrophy defined as the surface integral:

$$E(\mathbf{v}) = \frac{1}{2} \int \Omega^2 dS, \quad (4)$$

where \mathbf{v} is the velocity field, Ω is the vorticity, S is the surface.

To obtain the enstrophy density map we calculated the squared average vorticity within every grid cell (k, l) :

$$\varepsilon_{kl} = \left(\frac{1}{n} \sum_{i=0}^n \Omega_i \right)^2, \quad (5)$$

where n is the number of particles in the cell.

The abrupt enstrophy density change indicates the development of the interface. At $y = 3.5$ mm (cf. fig. 4, right panel) chains of flowing particles appear and start to penetrate into the resting particles¹. The chains of particles form fingers of a width of one particle and a length of 3 to 10 particles. Also islands of a few (3–5) particles can be observed. The multi-streaming results

¹In some sense this is similar to fingering observed in solid-liquid ⁴He interfaces in two dimensions [24].

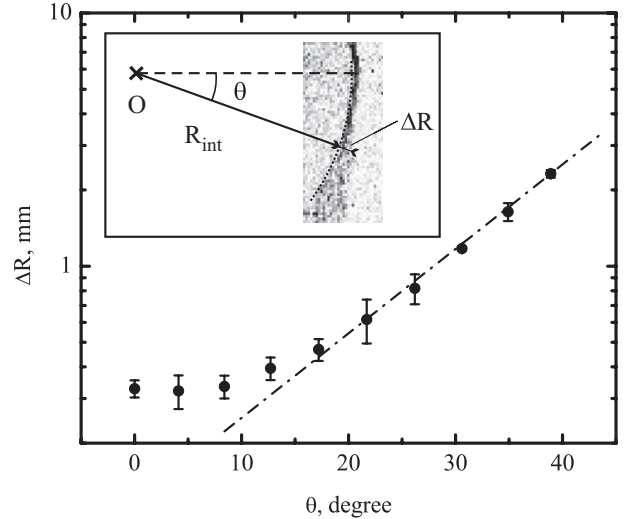


Fig. 6: The width of the mixing layer ΔR vs. angle θ . Insert: an enstrophy map imposed with the measurement geometry: The interface radius $R_{int}(\theta)$ and the radial width ΔR of the mixing layer are measured at every fixed value of the angle θ , counted from the horizontal (dashed) line. The dotted line is a circle, the point O indicates the circle center. The width of the mixing layer develops nearly exponentially; the dash-dotted line is $\Delta R \propto \exp\left(\frac{\theta \langle R_{int} \rangle}{L}\right)$, θ in rad, with the spatial increment $L^{-1} \simeq 4.0$ cm⁻¹.

in the reduction of the enstrophy density. This might be qualitatively explained as follows. A particle at the interface has a high $|\Omega_i|$ because of the relative shear. Whereas a particle in a finger has a low $|\Omega_i|$ because the local vorticity stemming from neighboring particles cancels as visualized in fig. 5.

Width of the interface. The width of the interface was measured vs. angle as shown in fig. 6. Note that at any fixed time moment the interface can be approximated well with a circle. To simplify the measurement procedure, the center of this circle (the point “O” in fig. 6) was used then as a “benchmark” for calculations $R_{int}(\theta)$ and $\Delta R(\theta)$. First $R_{int}(\theta) \approx 11 \pm 1.1$ mm the radial distance of the interface to point O was obtained. Then the width $\Delta R(\theta)$ was measured as the radial cross-section of the interface. We defined the interface as the region of the enstrophy density map (cf. fig. 4) where ε deviates significantly from the background value. The width was measured in an overlay of ten consecutive frames at five different time moments and averaged.

For $\theta < 10^\circ$ the width is approximately constant and of the order of the inter-particle separation. For $\theta > 10^\circ$ the width of the mixing layer develops nearly exponentially:

$$\Delta R \propto \exp\left(\frac{\pi\theta}{180^\circ} \frac{\langle R_{int} \rangle}{L}\right), \quad (6)$$

with a spatial increment $L^{-1} \approx 4.0$ cm⁻¹.

Estimated complex-plasma parameters. – The experiments we discuss here were performed at rather

typical conditions that allowed us to roughly estimate the plasma parameters extrapolating recently published results [9,16,25–28]. Based on this extrapolation we estimated the plasma density as $n_e = 10^8 \text{ cm}^{-3}$. The ion temperature is commonly believed to be equal to the neutral gas temperature, *i.e.* $T_i = 0.03 \text{ eV}$. For argon discharges in our conditions the electron temperature is known to be in the range $T_e = 2\text{--}4 \text{ eV}$ (see, *e.g.*, [9]). For these parameters the estimated particle charge is of the order of $q = Ze \approx 1000\text{--}2000e$ depending on the applied model [29] (DML) or [30] (OML). Note that in our case the charge is dependent on dust density because of the Havnes parameter $P_H > 1$ [31].

The charges are systematically lower in the stagnation zone where the particle cloud is denser. Independent of the model used to estimate the charge, the relative variation of the charge between the stagnation zone and the vortex is approximately $\frac{\delta Z}{\langle Z \rangle} \approx 0.11\text{--}0.15$, $\delta Z = |Z_s - Z_r|$. The charge difference can trigger the mechanism of “phase separation” [32], and introduce the interfacial surface tension effects [33].

For argon at a gas pressure of 55 Pa the Epstein drag coefficient [34] is $\gamma_{Eps} \approx 470 \text{ s}^{-1}$, it defines the friction force $F_{fr} = -m\gamma_{Eps}v$, where $m = 1.66 \cdot 10^{-15} \text{ kg}$ is the particle mass, and v is the particle velocity (relative to the gas). The ratio of the thermophoretic to the gravitational force is estimated as $F_{tph} \approx 0.9mg$, for our experimental conditions. The remaining imbalance can be attributed to the electric field force and the ion drag force. Neglecting the latter at the center of the vortex flow, and assuming further the balance $\frac{qE}{mg} = 1 - \frac{F_{tph}}{mg}$ and $q \approx 1000\text{--}2000e$ we get $E \approx 0.5\text{--}1 \text{ V/cm}$ at the height of the vortex center.

Origin of instability. – To characterize the dynamics of the particle flow it is important to estimate the relative strength of different forces. For instance, the inertial forces $\propto (v\nabla v)$, viscous forces $\propto (\nu v\mathcal{L}^{-2})$, Coriolis force $\propto (\Omega_c \times v)$ etc. Here v is the flow velocity, ν is the kinematic viscosity, Ω_c is the angular velocity of the global rotation, \mathcal{L} is the characteristic length scale. The ratios of these forces allow to determine which class of instabilities can be the reason for the interface breakup.

Reynolds number. The measurement of the viscosity of a complex plasma is a challenging issue. For two-dimensional systems the kinematic viscosity ν is of the order of $1 \frac{\text{mm}^2}{\text{s}}$ [35]. In our case we can estimate the viscosity by measuring the dissipation rate of vorticity at the interface. This yields $\nu \approx 10 \frac{\text{mm}^2}{\text{s}}$. With that value we obtain for the Reynolds number of this viscous flow around an obstacle $Re = \frac{v\mathcal{L}}{\nu} \approx 3$, here $\mathcal{L} = 10 \text{ mm}$ is the diameter of the void, $v = 3.3 \frac{\text{mm}}{\text{s}}$. Considering this low value our flow should be laminar dominated by the viscous forces that prevent the production of large scale eddies and vortices. This is also supported by the large neutral gas damping rate of 470 s^{-1} . The instability develops along the

interface in absence of large scale eddies and in fact can be better described by fingering [24]. The obtained Reynolds number is slightly less than $Re = 5\text{--}50$ given in [17].

Rossby number. It can be estimated for our case as $Ro = \frac{R_{int}}{\Delta R} \frac{v_{\perp}^2}{v_{\parallel}^2} \approx 0.3$, where $v_{\parallel,\perp}$ are the velocity components along and across the interface. Here R_{int} is the vortex radius, ΔR is the width of the interface (cf. fig. 6). The small value of the Rossby number means that the Coriolis force is not negligible in the system and can partly balance pressure forces.

Ekman number. The rather large $Ek = \frac{\nu}{\Omega_c \mathcal{L}^2} = 370$, here $\mathcal{L} = 0.3 \text{ mm}$ is the width of the laminar interface, means that the viscous forces in our experiment are bigger than the Coriolis force that is present for small fluctuations in the big vortex rotation.

Kelvin-Helmholtz (KH) instability. The KH-instability is suppressed by the strong friction force F_{fr} ; the estimated maximal increment is less than 0.06 s^{-1} in our conditions. We suggest that the reason for the interface breakup is a Rayleigh-Taylor instability between the resting and the streaming particle cloud.

Rayleigh-Taylor (RT) instability. The dispersion relation of a “deep water” RT-instability is

$$\Re\omega \approx v_D k, \Im\omega \approx \frac{(\rho_r - \rho_s)ka}{(\rho_r + \rho_s)\gamma} - \frac{(\alpha_s + \alpha_r)k^3}{(\rho_s + \rho_r)\gamma}, \quad (7)$$

where $\Re\omega$ and $\Im\omega$ are the real and imaginary part of the oscillation frequency, v_D is the drift velocity, k is the wavenumber, $\rho_s = 1.4 \frac{\text{g}}{\text{m}^3}$ and $\rho_r = 2.5 \frac{\text{g}}{\text{m}^3}$ are the mass densities of the two liquids, $\alpha_{r,s}$ are the surface tension coefficients, $\gamma = 470 \text{ s}^{-1}$ is the neutral gas drag and a is the effective acceleration.

The interface between the two liquids is destabilized by the effective acceleration and stabilized by surface tension.

The characteristic wavelength of the observed perturbation is $\lambda_{max} = \frac{2\pi}{k_{max}} = 1.8 \text{ mm}$. The drift velocity is the center-of-mass motion of the two liquids $v_D = V \frac{\rho_s}{\rho_s + \rho_r} = 1.1 \frac{\text{mm}}{\text{s}}$, where $V = 3.3 \frac{\text{mm}}{\text{s}}$ is the absolute velocity of the streaming particles. With the spacial increment of the instability $L^{-1} = 4.0 \text{ cm}^{-1}$ (cf. fig. 6) a temporal increment $\gamma' = \Im\omega = 0.44 \text{ s}^{-1}$ follows.

The maximal growth rate of the instability (7) gives the relationships

$$a = \frac{3}{2} \frac{\rho_r + \rho_s}{\rho_r - \rho_s} \frac{\gamma\gamma'}{k_{max}} \approx 0.3 \frac{\text{m}}{\text{s}^2}, \quad (8)$$

$$\alpha_s + \alpha_r = \frac{1}{2} \frac{\gamma\gamma'(\rho_s + \rho_r)}{k_{max}^3} \approx 1.0 \cdot 10^{-11} \frac{\text{kg}}{\text{s}^2}. \quad (9)$$

With the contact angle (3) we obtain for the surface tension $\alpha_s \approx \alpha_r \approx 5 \cdot 10^{-12} \frac{\text{kg}}{\text{s}^2}$. Note that this value is approximately 25 times less than that estimated in [36]. Since it is expected that $\alpha \propto Z^2$ [33] this discrepancy can be explained by the much lower charge of the particles in our conditions.

The origin of the acceleration a is still under debate. It can be caused by a radial outward thermophoretic force that is higher for the denser particle distribution at rest than for the streaming particles. Approximately 3–4% of the vertical thermophoretic force is required to explain $a = 0.3 \frac{m}{s^2}$. Note that radial temperature gradients of the order of 0.5–5% of the vertical gradient were measured in [23]. Alternatively the instability can be driven by a transverse electric field because the resting and streaming particles have a slightly different charge.

To conclude, in a complex plasma the interface blow-up accompanied by the exponential growth of the width of the mixing layer between the streaming and resting particles was observed. At the nonlinear stage of the instability the “single-layer” interface is replaced by a highly developed network of fluctuating “fingers”, “islands” or “sub-streams”, consisting of interpenetrating particles with different velocities. Development of RT-type perturbations stabilized by the interfacial surface tension is the most probable origin of the instability. The estimated surface tension coefficient agrees well with theoretical expectations.

The authors appreciate the valuable discussions with P. HUBER, A. IVLEV, V. NOSENKO and V. STEINBERG.

REFERENCES

- [1] FORTOV V., IVLEV A., KHRAPAK S., KHRAPAK A. and MORFILL G., *Phys. Rep.*, **421** (2005) 103.
- [2] MORFILL G. E. and IVLEV A. V., *Rev. Mod. Phys.*, **81** (2009) 1353.
- [3] SQUIRES T. M. and QUAKE S. R., *Rev. Mod. Phys.*, **77** (2005) 977.
- [4] DREYFUS R., TABELING P. and WILLAIME H., *Phys. Rev. Lett.*, **90** (2003) 144505.
- [5] FINK M. A., KRETSCHMER M., FORTOV V. and HOFNER *et al.*, *AIP Conf. Proc.*, **799** (2005) 295.
- [6] ZHDANOV S., NUNOMURA S., SAMSONOV D. and MORFILL G., *Phys. Rev. E*, **68** (2003) 035401.
- [7] SAMSONOV D., IVLEV A., QUINN R. A., MORFILL G. E. and ZHDANOV S. K., *Phys. Rev. Lett.*, **88** (2002) 9.
- [8] HEIDEMANN R., ZHDANOV S., SÜTTERLIN R., THOMAS H. M. and MORFILL G. E., *Phys. Rev. Lett.*, **102** (2009) 135002.
- [9] HEIDEMANN R. J., COUËDEL L., ZHDANOV S. *et al.*, *Phys. Plasmas*, **18** (2011) 053701.
- [10] THOMAS H. M. and MORFILL G. E., *Nature*, **379** (1996) 806.
- [11] RUBIN-ZUZIC M., MORFILL G. E., IVLEV A. V. *et al.*, *Nature Phys.*, **2** (2006) 181.
- [12] KNAPEK C. A., SAMSONOV D., ZHDANOV S., KONOPKA U. and MORFILL G. E., *Phys. Rev. Lett.*, **98** (2007) 015004.
- [13] HARTMANN P., DOUGLASS A., REYES J. C., MATTHEWS L. S., HYDE T. W., KOVÁCS A. and DONKÓ Z., *Phys. Rev. Lett.*, **105** (2010) 115004.
- [14] ARP O., CALIEBE D., MENZEL K., PIEL A. *et al.*, *IEEE Trans. Plasma Sci.*, **38** (2010) 842.
- [15] DURNIKAC C., SAMSONOV D., ZHDANOV S. and MORFILL G., *EPL*, **88** (2009) 45001.
- [16] SCHWABE M., RUBIN-ZUZIC M., ZHDANOV S., THOMAS H. M. and MORFILL G. E., *Phys. Rev. Lett.*, **99** (2007) 095002.
- [17] MORFILL G. E., RUBIN-ZUZIC M., ROTHERMEL H. *et al.*, *Phys. Rev. Lett.*, **92** (2004) 175004.
- [18] RUBIN-ZUZIC M., THOMAS H. M., ZHDANOV S. K. and MORFILL G. E., *New J. Phys.*, **9** (2007) 39.
- [19] MORFILL G. E., THOMAS H. M., ANNARATONE B. M. *et al.*, *AIP Conf. Proc.*, **649** (2002) 91.
- [20] FENG Y., GOREE J. and LIU B., *Rev. Sci. Instrum.*, **78** (2007) 053704.
- [21] MITIC S., SÜTTERLIN R., HÖFNER A. V. I. H., THOMA M. H., ZHDANOV S. and MORFILL G. E., *Phys. Rev. Lett.*, **101** (2008) 235001.
- [22] FLANAGAN T. M. and GOREE J., *Phys. Rev. E*, **80** (2009) 046402.
- [23] SCHWABE M., *Dynamical effects in fluids complex plasmas*, PhD Thesis, LMU (2009).
- [24] DEMARIA C. D., LEWELLEN J. W. and DAHM A. J., *J. Low Temp. Phys.*, **89** (1992) 385.
- [25] KLINDWORTH M., ARP O. and PIEL A., *Rev. Sci. Instrum.*, **78** (2007) 033502.
- [26] THOMAS H. M., MORFILL G. E., FORTOV V. *et al.*, *New J. Phys.*, **10** (2008) 033036.
- [27] KLINDWORTH M., ARP O. and PIEL A., *J. Phys. D: Appl. Phys.*, **39** (2006) 1095.
- [28] SCHWABE M., ZHDANOV S. K., THOMAS H. M. *et al.*, *New J. Phys.*, **10** (2008) 033037.
- [29] MORFILL G. E., KONOPKA U. and KRETSCHMER M. *et al.*, *New J. Phys.*, **8(1)** (2006) 7.
- [30] BONITZ M., HENNING C. and BLOCK D., *Rep. Prog. Phys.*, **73** (2010) 066501.
- [31] HAVNES O., MORFILL G. E. and GOERTZ C. K., *J. Geophys. Res.*, **89** (1984) 10999.
- [32] IVLEV A. V., ZHDANOV S. K., THOMAS H. M. and MORFILL G. E., *EPL*, **85** (2009) 45001.
- [33] WYSOCKI A., RÄTH C., IVLEV A. V. *et al.*, *Phys. Rev. Lett.*, **105** (2010) 045001.
- [34] EPSTEIN P. S., *Phys. Rev.*, **23** (1924) 710.
- [35] NOSENKO V. and GOREE J., *Phys. Rev. Lett.*, **93** (2004) 155004.
- [36] SCHWABE M., RUBIN-ZUZIC M., ZHDANOV S. *et al.*, *Phys. Rev. Lett.*, **102** (2009) 255005.

8 Acknowledgments

My special thanks goes to all the people without whose support this work would not have been possible. I am very thankful to my supervisor Prof. Gregor Morfill for the opportunity to work on this fascinating subject in his Complex Plasma group at the Max Planck Institute for Extraterrestrial Physics. I would like to thank Dr. Hubertus Thomas for all his support and for his inspiration to work on “his” experiment PK-3 Plus. In particular I wish to thank Prof. Sergey Zhdanov for the numerous discussions, his teachings and his encouragement. It was truly a stroke of luck to share the office with such a great physicist.

I also want to thank Dr. Robert Sütterlin for the fruitful discussions and for providing me interesting insights into the data analysis, especially regarding the particle detection algorithms. I want to thank Dr. Lènaïc Couëdel for the great collaboration on the heartbeat subject. I also like to extend my thanks to the project engineers Tanja Hagl and Dr. Herman Rothermel for answering my many questions about the experimental setup. Additionally I want to thank Dr. Uwe Konopka and Dr. Milenko Rubin-Zuzic for their advice on the design of the experiments. I also thank the astronauts for their enthusiasm and dedication in performing our experiments on the international space station. In regards to this work especially to Valery Tokarev, Pavel Vinogradov and Thomas Reiter. I thank Angelika Langer for all the help with the administrative work.

Last but not least I am particularly grateful to Beata and to my family for all their support.

8 Acknowledgments

List of Figures

1.1	Photograph of complex plasma in the PK-3 Plus chamber	13
1.2	Electric potential in the plasma chamber	17
1.3	Photograph of a neon plasma in the PK-3 Plus plasma chamber	22
1.4	Simplified circuit of an inductively coupled discharge	23
1.5	Simplified circuit of a capacitively coupled discharge	24
2.1	Schematic of the PKE-Nefedov plasma chamber.	25
2.2	Schematic of the PK-3 Plus plasma chamber.	26
2.3	RF-current measurement in a bridge configuration	28
2.4	Time resolved measurement of current and voltage	29
2.5	Power factor η for the PK-3 Plus setup	30
2.6	Circuit diagram of the external electric wiring of PK-3 Plus . .	31
2.7	Scheme of the illumination laser optics for the ground setup of PK-3 Plus and PKE-Nefedov.	32
2.8	Typical image from the experiment	33
2.9	Scheme of the PK-4 setup	34
3.1	Particle positions with strong pixel locking	37
3.2	3D positions of the particles and the projection of a slice onto the x-y plane	39
3.3	Particle density of the simulated particle cloud calculated from 2D projections with different slice width	40
3.4	Particle density of the of a simulated particle cloud calculated from 2D projections	42
3.5	Deviation of the calculated density relative to the density n_0 for different projection width	42
3.6	Pair correlation functions obtained from the simulated data in 3D and in 2D projections with different slice width	43
3.7	Profile of the illumination laser obtained from three dimensional scans	45
4.1	Dark and bright solitons by Marc Haelterman in 1989	49
5.1	The different phases of a heartbeat oscillation	59
5.2	Comparison of the observed and simulated microparticle trajec- tories	62

List of Figures

5.3	Comparison of the simulated microparticle trajectories	62
6.1	Sketch of the flow pattern	66
6.2	Central cross-section of a toroidal vortex stream	71

Bibliography

- [1] R. Heidemann, S. Zhdanov, R. Sütterlin, H. M. Thomas, and G. E. Morfill. Dissipative dark soliton in a complex plasma. *Phys. Rev. Lett.*, 102(13):135002, Mar 2009.
- [2] S. Zhdanov, R. Heidemann, M. H. Thoma, R. Sütterlin, H. M. Thomas, H. Höfner, K. Tarantik, G. E. Morfill, A. D. Usachev, O. F. Petrov, and V. E. Fortov. Dissipative dark solitons in a dc complex plasma. *EPL (Europhysics Letters)*, 89(2):25001, 2010.
- [3] R.J. Heidemann, L. Couëdel, S.K. Zhdanov, K.R. Sütterlin, M. Schwabe, H.M. Thomas, A.V. Ivlev, T. Hagl, G.E. Morfill, V.E. Fortov, V.I. Molotkov, O.F. Petrov, A.I. Lipaev, V. Tokarev, T. Reiter, and P. Vinogradov. Comprehensive experimental study of heartbeat oscillations observed under microgravity conditions in the pk-3 plus laboratory on board the international space station. *Physics of Plasmas*, 18(5):053701, 2011.
- [4] S.K. Zhdanov, M. Schwabe, R. Heidemann, R. Sütterlin, H.M. Thomas, M. Rubin-Zuzic, H. Rothermel, T. Hagl, A.V. Ivlev, G.E. Morfill, V.I. Molotkov, A.M. Lipaev, O.F. Petrov, V.E Fortov, and T. Reiter. Auto-oscillations in complex plasmas. *New Journal of Physics*, 12(4):043006, 2010.
- [5] R. Heidemann, S. Zhdanov, K. R. Sütterlin, H. M. Thomas, and G. E. Morfill. Shear flow instability at the interface among two streams of a highly dissipative complex plasma. *EPL (Europhysics Letters)*, 96(1):15001, 2011.
- [6] I. Langmuir. Oscillations in ionized gases. *Proc. Nat. Acad. Sci. U.S.*, 14:628, 1928.
- [7] Hannes Alfvén and Per Carlqvist. Interstellar clouds and the formation of stars. *Astrophysics and Space Science*, 55:487–509, 1978. 10.1007/BF00642272.
- [8] A. Cavaliere and R. Fusco-Femiano. X-rays from hot plasma in clusters of galaxies. *Astronomy and Astrophysics*, 49:137–144, 1976.
- [9] John F. Waymouth and Francis Bitter. Analysis of the plasma of fluorescent lamps. *Journal of Applied Physics*, 27(2):122 –131, feb 1956.

Bibliography

- [10] M. A. Lieberman and A. J. Lichtenberg. *Principles of plasma discharges and materials processing*. Wiley, New York, 1994.
- [11] Gregory Fridman, Marie Peddinghaus, Manjula Balasubramanian, Halim Ayan, Alexander Fridman, Alexander Gutsol, and Ari Brooks. Blood coagulation and living tissue sterilization by floating-electrode dielectric barrier discharge in air. *Plasma Chemistry and Plasma Processing*, 26:425–442, 2006. 10.1007/s11090-006-9024-4.
- [12] M. G. Kong, G. Morfill, and W. Stolz. *Plasma Medicine - Applications of Low-Temperature Gas Plasmas in Medicine and Biology*. Cambridge University Press, May 2012.
- [13] R. Aymar, P. Barabaschi, and Y. Shimomura. The iter design. *Plasma Physics and Controlled Fusion*, 44(5):519, 2002.
- [14] R. Heidemann, M. Kretschmer, S.K. Zhdanov, K.R. Sutterlin, H.M. Thomas, M.H. Thoma, and G.E. Morfill. Dissipative dark soliton in a complex plasma. *Plasma Science, IEEE Transactions on*, 39(11):2720 – 2721, nov. 2011.
- [15] H. Thomas, G. E. Morfill, V. Demmel, J. Goree, B. Feuerbacher, and D. Möhlmann. Plasma crystal: Coulomb crystallization in a dusty plasma. *Phys. Rev. Lett.*, 73(5):652–655, Aug 1994.
- [16] J. H. Chu and Lin I. Direct observation of coulomb crystals and liquids in strongly coupled rf dusty plasmas. *Phys. Rev. Lett.*, 72(25):4009–4012, Jun 1994.
- [17] Yasuaki Hayashi and Kunihide Tachibana. Observation of coulomb-crystal formation from carbon particles grown in a methane plasma. *Jpn. J. Appl. Phys.*, 33:L804–L806, 1994.
- [18] H. M. Thomas and G. E. Morfill. Melting dynamics of a plasma crystal. *Nature*, 379:806–809, 1996.
- [19] M. Rubin-Zuzic, G. E. Morfill, A. V. Ivlev, R. Pompl, B. A. Klumov, W. Bunk, H. M. Thomas, H. Rothermel, O. Havnes, and A. Fouqué. Kinetic development of crystallization fronts in complex plasmas. *Nature Physics*, 2:181–185, 2006.
- [20] M. Schwabe, M. Rubin-Zuzic, S. Zhdanov, H. M. Thomas, and G. E. Morfill. Highly resolved self-excited density waves in a complex plasma. *Phys. Rev. Lett.*, 99(9):095002, 2007.
- [21] A. Barkan, R. L. Merlino, and N. D’Angelo. Laboratory observation of the dust-acoustic wave mode. *Physics of Plasmas*, 2(10):3563–3565, 1995.

- [22] Gregor E. Morfill, Milenko Rubin-Zuzic, Hermann Rothermel, Alexei V. Ivlev, Boris A. Klumov, Hubertus M. Thomas, Uwe Konopka, and Victor Steinberg. Highly resolved fluid flows: “liquid plasmas” at the kinetic level. *Phys. Rev. Lett.*, 92(17):175004, Apr 2004.
- [23] C. K. Goertz and G. Morfill. A model for the formation of spokes in saturn’s ring. *Icarus*, 53(2):219–229, February 1983.
- [24] R. Bingham and V. N. Tsytovich. Dust growth in astrophysical plasmas. In R. Bharuthram, M. A. Hellberg, P. K. Shukla, and F. Verheest, editors, *Dusty Plasmas in the new Millennium: Third Conference on the Physics of Dusty Plasmas*, volume 649, pages 126–134. AIP, 2002.
- [25] G. S. Selwyn, J. Singh, and R. S. Bennett. In situ laser diagnostic studies of plasma-generated particulate contamination. *J. Vac. Sci. Technol. A*, 7(4):2758–2765, 1989.
- [26] André Bouchoule. *Dusty Plasmas: Physics, Chemistry and Technological impacts in Plasma Processing*. Wiley, New York, 1999.
- [27] H. M. Mott-Smith and Irving Langmuir. The theory of collectors in gaseous discharges. *Phys. Rev.*, 28(4):727–763, Oct 1926.
- [28] J. E. Allen. Probe theory - the orbital motion approach. *Physica Scripta*, 45(5):497, 1992.
- [29] S. A. Khrapak, S. V. Ratynskaia, A. V. Zobnin, A. D. Usachev, V. V. Yaroshenko, M. H. Thoma, M. Kretschmer, H. Hofner, G. E. Morfill, O. F. Petrov, and V. E. Fortov. Particle charge in the bulk of gas discharges. *Phys. Rev. E*, 72(1):016406, 2005.
- [30] A. V. Zobnin, A. P. Nefedov, V. A. Sinel’Shchikov, and V. E. Fortov. On the Charge of Dust Particles in a Low-Pressure Gas Discharge Plasma. *Soviet Journal of Experimental and Theoretical Physics*, 91:483–487, September 2000.
- [31] Gregor E. Morfill, Uwe Konopka, Michael Kretschmer, Milenko Rubin-Zuzic, Hubertus M. Thomas, Sergej K Zhdanov, and Vadim Tsytovich. The ‘classical tunnelling effect’ - observations and theory. *New Journal of Physics*, 8(1):7, 2006.
- [32] Martin Lampe, Rajiv Goswami, Zoltan Sternovsky, Scott Robertson, Valeriy Gavrishchaka, Gurudas Ganguli, and Glenn Joyce. Trapped ion effect on shielding, current flow, and charging of a small object in a plasma. *Physics of Plasmas*, 10(5):1500–1513, 2003.

Bibliography

- [33] O. Havnes, G. E. Morfill, and C. K. Goertz. Plasma potential and grain charges in a dust cloud embedded in a plasma. *J. Geophys. Res.*, 89:10999 – 11003, 1984.
- [34] Krastan Blagoev Gabor J. Kalman, J. Martin Rommel. *Strongly Coupled Coulomb Systems*. Kluwer Academic/Plenum Publishers, 1999.
- [35] Jie Kong, Truell W. Hyde, Lorin Matthews, Ke Qiao, Zhuanhao Zhang, and Angela Douglass. One-dimensional vertical dust strings in a glass box. *Phys. Rev. E*, 84:016411, Jul 2011.
- [36] http://www.siglo-kinema.com/siglo_2d.htm.
- [37] Paul S. Epstein. On the resistance experienced by spheres in their motion through gases. *Phys. Rev.*, 23(6):710–733, Jun 1924.
- [38] Bin Liu, J. Goree, V. Nosenko, and L. Boufendi. Radiation pressure and gas drag forces on a melamine-formaldehyde microsphere in a dusty plasma. *Phys. Plasmas*, 10(1):9–20, 2003.
- [39] H. Rothermel, T. Hagl, G. E. Morfill, M. H. Thoma, and H. M. Thomas. Gravity compensation in complex plasmas by application of a temperature gradient. *Phys. Rev. Lett.*, 89(17):175001, Oct 2002.
- [40] S. Mitic, R. Sütterlin, A. V. Ivlev H. Höfner, M. H. Thoma, S. Zhdanov, and G. E. Morfill. Convective dust clouds driven by thermal creep in a complex plasma. *Phys. Rev. Lett.*, 101(23):235001, Dec 2008.
- [41] S. A. Khrapak, A. V. Ivlev, G. E. Morfill, and H. M. Thomas. Ion drag force in complex plasmas. *Phys. Rev. E*, 66(4):046414, Oct 2002.
- [42] S. A. Khrapak, A. V. Ivlev, S. K. Zhdanov, and G. E. Morfill. Hybrid approach to the ion drag force. *Phys. Plasmas*, 12:042308, 2005.
- [43] B.A. Trubnikov. *Reviews of Plasma Physics*, volume 1. Consultants Bureau, New York, 1965.
- [44] Michael S. Barnes, John H. Keller, John C. Forster, James A. O’Neill, and D. Keith Coultas. Transport of dust particles in glow-discharge plasmas. *Phys. Rev. Lett.*, 68(3):313–316, Jan 1992.
- [45] G. E. Morfill, H. M. Thomas, U. Konopka, H. Rothermel, M. Zuzic, A. Ivlev, and J. Goree. Condensed plasmas under microgravity. *Phys. Rev. Lett.*, 83(8):1598–1601, Aug 1999.
- [46] R. B. Piejak, V. A. Godyak, and B. M. Alexandrovich. A simple analysis of an inductive rf discharge. *Plasma Sources Science and Technology*, 1(3):179, 1992.

- [47] Anatoli P. Nefedov, Gregor E. Morfill, Vladimir E. Fortov, Hubertus M. Thomas, Hermann Rothermel, Tanja Hagl, Alexei V. Ivlev, Milenko Zuzic, Boris A. Klumov, Andrey M. Lipaev, Vladimir I. Molotkov, Oleg F. Petrov, Yuri P. Gidzenko, Sergey K. Krikalev, William Shepherd, Alexandr I. Ivanov, Maria Roth, Horst Binnenbruck, John A. Goree, and Yuri P. Semenov. Pke-nefedov: plasma crystal experiments on the international space station. *New J. Phys.*, 5:33.1–33.10, 2003.
- [48] H. M. Thomas, G. E. Morfill, V. E. Fortov, A. V. Ivlev, V. I. Molotkov, A. M. Lipaev, T. Hagl, H. Rothermel, S. A. Khrapak, R. K. Suetterlin, M. Rubin-Zuzic, O. F. Petrov, V. I. Tokarev, and S. K. Krikalev. Complex plasma laboratory pk-3 plus on the international space station. *New Journal of Physics*, 10(3):033036, 2008.
- [49] A. Usachev, A. Zobnin, O. Petrov, V. Fortov, M. Thoma, M. Kretschmer, S. Ratynskaia, R. Quinn, H. Hoefner, and G. Morfill. The project “Plasmakristall-4” (PK-4) - a dusty plasma experiment in a combined dc/rf(i) discharge plasma under microgravity conditions. *Czechoslovak Journal of Physics*, 54(Part 4):C639–C647, 2004. 21st Symposium on Plasma Physics and Technology, Heyrovsky Inst Acad Sci, Prague, Czech Republic, Jun 14-17, 2004.
- [50] V. Fortov, G. Morfill, O. Petrov, M. Thoma, A. Usachev, H. Hoefner, A. Zobnin, M. Kretschmer, S. Ratynskaia, M. Fink, K. Tarantik, Yu Gerasimov, and V. Esenkov. The project ‘plasmakristall-4’ (pk-4) a new stage in investigations of dusty plasmas under microgravity conditions: first results and future plans. *Plasma Physics and Controlled Fusion*, 47(12B):B537, 2005.
- [51] Y. Feng, J. Goree, and Bin Liu. Accurate particle position measurement from images. *Review of Scientific Instruments*, 78(5):053704, 2007.
- [52] Yuriy Ivanov and Andre Melzer. Particle positioning techniques for dusty plasma experiments. *Review of Scientific Instruments*, 78(3):033506, 2007.
- [53] I.V. Hertel and C.P. Schulz. *Atome, Moleküle und optische Physik 1*. Springer, 2010.
- [54] Ke Jiang. *Particle manipulation in plasma device & Dynamics of binary complex plasma*. PhD thesis, LMU München: Fakultät für Physik, 2011.
- [55] J.S. Russell. *Report on waves: made to the meetings of the British Association in 1842-43*. 1845.
- [56] Yuri S. Kivshar and Barry Luther-Davies. Dark optical solitons: physics and applications. *Physics Reports*, 298(2-3):81 – 197, 1998.

Bibliography

- [57] N. Akhmediev and A. Ankiewicz (eds.). *Dissipative Solitons. Lect. Notes Phys.*, volume 661. Springer, 2005.
- [58] D. Samsonov, A.V. Ivlev, R. A. Quinn, G. E. Morfill, and S. K. Zhdanov. Dissipative longitudinal solitons in a two-dimensional strongly coupled complex (dusty) plasma. *Phys. Rev. Lett.*, 88:9, 2002.
- [59] V. E. Fortov, A. D. Usachev, A. V. Zobnin, V. I. Molotkov, and O. F. Petrov. Dust-acoustic wave instability at the diffuse edge of radio frequency inductive low-pressure gas discharge plasma. *Physics of Plasmas*, 10(5):1199–1208, 2003.
- [60] V. E. Fortov, O. F. Petrov, V. I. Molotkov, M. Y. Poustylnik, V. M. Torchinsky, A. G. Khrapak, and A. V. Chernyshev. Large-amplitude dust waves excited by the gas-dynamic impact in a dc glow discharge plasma. *Phys. Rev. E*, 69(1):016402, 2004.
- [61] V. E. Fortov, O. F. Petrov, V. I. Molotkov, M. Y. Poustylnik, V. M. Torchinsky, V. N. Naumkin, and A. G. Khrapak. Shock wave formation in a dc glow discharge dusty plasma. *Phys. Rev. E*, 71(3):036413, 2005.
- [62] Akira Hasegawa and Masayuki Matsumoto. *Optical Solitons in Fibers*. Springer-Verlag, 2002.
- [63] S. Burger, K. Bongs, S. Dettmer, W. Ertmer, K. Sengstock, A. Sanpera, G. V. Shlyapnikov, and M. Lewenstein. Dark solitons in bose-einstein condensates. *Phys. Rev. Lett.*, 83:5198–5201, Dec 1999.
- [64] M. Schwabe, M. Rubin-Zuzic, S. Zhdanov, H. M. Thomas, and G. E. Morfill. Highly resolved self-excited density waves in a complex plasma. *Phys. Rev. Lett.*, 99(9):095002, 2007.
- [65] A. Couairon and J.M. Chomaz. Absolute and convective instabilities, front velocities and global modes in nonlinear systems. *Physica D*, 108(3):236–276, 1997.
- [66] A. A. Mamun and P. K. Shukla. Cylindrical and spherical dust-acoustic shock waves in a strongly coupled dusty plasma. *New Journal of Physics*, 11(10):103022, 2009.
- [67] A.A. Mamun and P.K. Shukla. Formation of dust-acoustic shock waves in a strongly coupled cryogenic dusty plasma. *Physics Letters A*, 373(35):3161 – 3164, 2009.
- [68] P. Bandyopadhyay, U. Konopka, S. A. Khrapak, G. E. Morfill, and A. Sen. Effect of polarization force on the propagation of dust acoustic solitary waves. *New Journal of Physics*, 12(7):073002, 2010.

- [69] Samiran Ghosh, Subrata Sarkar, Manoranjan Khan, and M. R. Gupta. Low-frequency wave modulations in an electronegative dusty plasma in the presence of charge variations. *Phys. Rev. E*, 84:066401, Dec 2011.
- [70] K. R. Sütterlin, A. Wysocki, C. R ath, A. V. Ivlev, H. M. Thomas, S. Khrapak, S. Zhdanov, M. Rubin-Zuzic, W. J. Goedheer, V. E. Fortov, A. M. Lipaev, V. I. Molotkov, O. F. Petrov, G. E. Morfill, and H. L owen. Non-equilibrium phase transitions in complex plasma. *Plasma Physics and Controlled Fusion*, 52(12):124042, 2010.
- [71] K. O. Menzel, O. Arp, and A. Piel. Spatial frequency clustering in nonlinear dust-density waves. *Phys. Rev. Lett.*, 104:235002, Jun 2010.
- [72] D. J. Frantzeskakis. Dark solitons in atomic bose-einstein condensates: from theory to experiments. *Journal of Physics A: Mathematical and Theoretical*, 43(21):213001, 2010.
- [73] G. Grosso, G. Nardin, F. Morier-Genoud, Y. L eger, and B. Deveaud-Pl edran. Soliton instabilities and vortex street formation in a polariton quantum fluid. *Phys. Rev. Lett.*, 107:245301, Dec 2011.
- [74] M. Mikikian, L. Cou edel, M. Cavarroc, Y. Tessier, and L. Boufendi. Self-excited void instability in dusty plasmas: plasma and dust cloud dynamics during the heartbeat instability. *New Journal of Physics*, 9(8):268, 2007.
- [75] M. Klindworth, O. Arp, and A. Piel. Langmuir probe system for dusty plasmas under microgravity. *Review of Scientific Instruments*, 78(3):033502, 2007.
- [76] V.E. Fortov, A.V. Ivlev, S.A. Khrapak, A.G. Khrapak, and G.E. Morfill. Complex (dusty) plasmas: Current status, open issues, perspectives. *Physics Reports*, 421(1-2):1 – 103, 2005.
- [77] V. Nosenko and J. Goree. Shear flows and shear viscosity in a two-dimensional yukawa system (dusty plasma). *Phys. Rev. Lett.*, 93(15):155004, Oct 2004.
- [78] A. Gavrikov, I. Shakhova, A. Ivanov, O. Petrov, N. Vorona, and V. Fortov. Experimental study of laminar flow in dusty plasma liquid. *Physics Letters A*, 336(4-5):378 – 383, 2005.
- [79] N. Vorona, A. Gavrikov, A. Ivanov, O. Petrov, V. Fortov, and I. Shakhova. Viscosity of a dusty plasma liquid. *Journal of Experimental and Theoretical Physics*, 105:824–830, 2007. 10.1134/S1063776107100172.

Bibliography

- [80] K. A. Pacha, J. R. Heinrich, S.-H. Kim, and R. L. Merlino. Observation of the taylor instability in a dusty plasma. *Physics of Plasmas*, 19(1):014501, 2012.
- [81] A. Budea, A. Derzsi, P. Hartmann, and Z. Donko. Shear viscosity of liquid-phase yukawa plasmas from molecular dynamics simulations on graphics processing units. *Contributions to Plasma Physics*, 52(3):194–198, 2012.